Studies of Hydrogen Storage in the $4NaBH_4/5Mg_2NiH_4$ Composite System

by

Louis Greg Afonso

BASc, The University of British Columbia, 2008

A THESIS SUBMITTED IN PARTIAL FULFILLMENT OF
THE REQUIREMENTS FOR THE DEGREE OF

MASTER OF APPLIED SCIENCE

in

The Faculty of Graduate Studies

(Chemical and Biological Engineering)

THE UNIVERSITY OF BRITISH COLUMBIA

(Vancouver)

January 2013

Abstract

Complex metal hydrides typically have high enthalpies which lead to desorption temperatures that are too high for practical use. Thermodynamic destabilization is one method used to lower the enthalpy of decomposition and hence lower the temperature of desorption of a complex metal hydride. A lower temperature (less than 100ºC) would enable waste heat from a PEM (Polymer Electrolyte Membrane) fuel cell to drive the hydrogen desorption reaction. $NaBH_4$ was destabilized by ball milling $NaBH_4$ and Mg_2NiH_4 in a 4:5 molar ratio, respectively. Ball milling periods of up to 2 hours did not have an effect on the thermodynamics or the kinetics of the system. Grain sizes of the two phases, $NaBH_4$ and Mg_2NiH_4, were reduced during the first 30 minutes of ball milling. The decomposition enthalpy of the system was measured and found to be 67 ± 4 kJ $mol_{H_2}^{-1}$ for the decomposition of Mg_2NiH_4 in the composite, 76 ± 5 kJ $mol_{H_2}^{-1}$ for the decomposition of $NaBH_4$ and 95 ± 7 kJ $mol_{H_2}^{-1}$ for the decomposition of NaH, which corresponds to measured desorptions at 275, 360 and 420 ºC respectively. The enthalpy of absorption corresponding to Mg_2NiH_4 in the composite was 59 ± 4 kJ $mol_{H_2}^{-1}$. During dehydrogenation of the $NaBH_4$ phase, the ternary boride phase $MgNi_{2.5}B_2$ is formed under a hydrogen back pressure of vacuum, 1 bar and 5 bar. The total capacity of the system is 5.1 wt%, and a capacity loss of 2.25 wt% hydrogen was noted during cycling studies partially due to the formation of $MgNi_2$, which is a non-hydriding phase, loss of Na from the sample holder, and the formation of large crystals of Mg that could not be hydrogenated easily. Kinetic analysis was conducted and an activation energy of 131 ± 24 kJ mol^{-1} was determined for the decomposition of the Mg_2NiH_4 phase

of the composite. XRD phase analysis showed that the Mg_2NiH_4 decomposed first starting at about 275 ºC, followed by the decomposition of $NaBH_4$ at around 360 ºC. By 400 ºC, XRD analysis showed that the $MgNi_{2.5}B_2$ phase had formed. The effect of cycling on the crystallographic phases showed a change from monoclinic to cubic for the Mg_2NiH_4 phase of the composite as well as the formation of $MgNi_2$.

Preface

The work in this thesis culminated in the production of a manuscript “Studies of Hydrogen Storage in the $4NaBH_4/5Mg_2NiH_4$ Composite System”. This Masters thesis work has been done by Louis Greg Afonso under the direct supervision of Professor David Wilkinson and Arman Bonakdarpour in the Department of Chemical and Biological Engineering at the University of British Columbia.

Identification and design of the research program was conducted by Louis Greg Afonso with guidance by Professor David Wilkinson and Arman Bonakdarpour. Performance of the various parts of the research was conducted by Louis Greg Afonso with guidance by Professor David Wilkinson and Arman Bonakdarpour. Analysis of the research data was conducted by Louis Greg Afonso with guidance by Professor David Wilkinson and Arman Bonakdarpour. Preparation of manuscripts is currently underway and is being written by Louis Greg Afonso with guidance by Professor David Wilkinson and Arman Bonakdarpour.

Table of Contents

List of Tables

List of Figures

Nomenclature

DOE	Department of Energy
α	The unsaturated hydrogenated phase a hydride
β	The saturated hydrogenated phase of a hydride
β_{FWHM}	Full width half max of peak height
β_{ramp}	Heating rate for kissinger analysis
ΔH	Change in enthalpy
ΔS	Change in entropy
η	Weight factor for pseudo - Voight function
γ - MgH_2	High pressure gamma phase magnesium hydride
λ	Wavelength of x-ray
θ	angle of incidence
d	Interplanar distance between atoms
d_g	Grain size
DSC	Differential scanning calorimetry
E_a	Activation energy

fcc	Face centered cubic
FWHM	Full width half maximum
G	Gaussian function
k_0	Constant for Kissinger analysis
L	Lorentzian function
LOHC	Liquid organic hydrogen carriers
n	number of moles
NSERC	Natural Sciences and Engineering Council
P	Pressure
P_0	Atmospheric pressure
P_R	Reactor pressure
P_S	Reservoir pressure
P_T	Total pressure
PCT	Pressure composition temperature
PDF	Powder diffraction file
PEM	Polymer electrolyte membrane
R	Universal gas constant
SEM	Scanning electron microscopy
T	Temperature

$T_{plateau}$	Temperature of PCT isotherm plateau
TGA	Thermogravimetric analysis
TPD	Temperature programmed desorption
V	Volume
V_R	Reactor volume
V_S	System volume
XRD	X-ray diffraction

Acknowledgments

I wish to thank my supervisors Dr. David Wilkinson and Dr. Arman Bonakdarpour for the opportunity to participate in trying to make this world a better place. I would also like to thank them for their endless patience and guidance; it is truly an honour to have them as my mentors. In addition, I wish to thank Rob Hui at the National Research Council Institute for Fuel Cell Innovation (now Energy, Mining and Environment) for putting up with my constant requests for building access and allowing me the use of their facilities, without which I would not have been able to complete my research. To Jasna Jankovich, who planted the seed that started me off on this journey. I would also like to acknowledge NSERC and H_2Can for funding to make this research possible.

To my mom Christine Zarazun who has shown me throughout my life that anything can be overcome. Her single handed determination to never settle for what life has given her and to strive for better despite the odds has been a continuing inspiration for me as I move through my life. To Kar-Yee whose support and shelter from the storm was greatly needed. And to my son Rowan, who makes every day worth living. I can't wait until he can write about how inspirational I was to him in his own thesis acknowledgments!

Chapter 1

Introduction

Energy carriers are currently under intense research and hydrogen is one of the top contenders because it can be produced with renewable energy technologies (e.g., water electrolysis), it is very light, non-toxic, and can be used to generate power without harmful emissions. The interest in new energy carriers stems from our growing use of energy and the increasingly limited available resources. Although hydrogen is not a primary energy source, as a carrier, it will enable energy sources such as wind and solar to cleanly and safely store and / or transport the energy they produce upon demand.

Concerns over energy security are also playing an important role in the push to introduce hydrogen as an energy carrier. Traditional sources of energy such as fossil fuels are only available in specific locations which are often politically volatile, leading to instabilities in their price and availability. Renewable energy sources such as solar energy can lead to a decentralized energy system, effectively allowing energy production to occur anyplace a renewable energy source can be situated. This is increasingly important as fossil fuel resources are finite and will eventually become scarce, leading to intense competition and political strain. Industrialization of countries such as China, India and other developing countries mean rising energy demands for a population seeking the same lifestyle and standard of living seen in industrialized nations like the USA.

Decentralized energy production and storage through the use of hydrogen is a goal that many researchers have been striving to make possible, however, there are a number of problems associated with the use of this new energy carrier. One particular problem is the

storage of hydrogen: while it has the highest gravimetric energy density of common fuels, it also has the lowest volumetric energy density. This means that while the weight associated with the storage of hydrogen may be low, it requires a large volume.

Safe storage and handling of hydrogen is also very important in any potential application. Pressurized and liquified hydrogen are the current methods for storing hydrogen. However, for mass production and use of hydrogen these methods of storage are not considered suitable due to the extreme pressures or low temperatures required [1, 2, 3]. As well, the energy required to compress or liquefy hydrogen, which can be up to 1/3 of the total energy stored, lowers the efficiency of hydrogen as an energy carrier making it an even more unattractive solution [2].

Currently there is significant research effort on developing materials that can store hydrogen reversibly. One of these methods is solid state storage through metal hydrides. This approach differs from the more traditional methods of pressurization and liquefaction in that chemical reactions typically take place to liberate the hydrogen from the storage medium and are also required to store it back again. In general, heat is added to the material to release hydrogen, and pressure and heat removal are required for rehydrogenation.

1.1 Thesis Overview

The overall approach is to develop a complex metal hydride system (mixture of complex metal hydrides) capable of absorbing and desorbing hydrogen at a temperature of about 100 ºC or lower. The features of such a system would be as follows:

- Absorption and desorption of hydrogen at or below 100 ºC
- Mixed complex hydride system
- Use of non-scarce materials
- Low pressure storage

In order to achieve these goals the thermodynamics of currently existing complex hydrides must be altered such that the enthalpy of reaction for the hydrogen release and storage is lowered. The goal of the work in this thesis is to develop a combination of complex hydrides (i.e. hydride system) to achieve this lower enthalpy and thus lower operating temperatures.

1.2 Thesis Layout

This thesis is arranged into 5 main sections: i) the introduction, ii) the background, literature review and thesis objectives, iii) experimental techniques and analysis, iv) results and discussion, v) conclusions and future work. The introduction will present a brief background to the topic as well as the motivations involved. The literature review will survey the current state of the art in the field of hydrogen storage pertaining to metal hydrides. Experimental techniques will introduce and explain all of the equipment and the analysis used to characterize and understand the metal hydride systems under study. Results and discussion will go in depth into the analysis of the data collected and explain what was discovered, and finally any conclusions made from the results and discussion section will be highlighted in the conclusions section along with recommendations for future work.

Chapter 2

Background, Literature Review and Thesis Objectives

Much research has been conducted on altering the thermodynamics of metal hydrides [4, 5, 6, 7, 8]. In particular destabilized $LiBH_4$ mixtures (either $LiBH_4$ / MgH_2, $LiBH_4$ / Mg_2NiH_4 etc.) have been studied in the past few years.

$LiBH_4$ is a readily available chemical commonly used as a reducing agent for esters [9]. Unfortunately, lithium is a relatively scarce element, and its use in the lithium ion battery is continuing to rise. It is projected that by 2025 its use alone in the lithium ion battery will exceed the amount available on the planet [10] creating the potential for limited supply. An alternative to $LiBH_4$ is $NaBH_4$ and although not as gravimetrically appealing (18.4 vs 10.66 wt%) it has the advantage of utilizing one of the most abundant elements on earth, sodium. The compound $NaBH_4$ is also used commonly as a reducing agent and as such is already available on a commercial scale as well.

2.0.1 US Department of Energy (DOE) Targets for Hydrogen Storage

For automotive applications, the US Department of Energy (DOE) has set requirements for storage capacity, reaction rates, and cycling reversibility as presented in table 2.1 [11]. In Canada there are various research groups working on this subject and there is also a nation-wide NSERC research network (H2Can) with a five year time frame which brings researchers across Canada to work on hydrogen storage materials, production, handling and

safety [12].

Table 2.1: DOE hydrogen storage targets for vehicular application (adapted from [11])

		Targets (as of 2009)		
Storage parameter	**Units**	**2010**	**2015**	**Ultimate**
System gravimetric capacity	kWh kg^{-1}	1.5	1.8	2.5
	wt% H_2	4.5	5.5	7.5
System volumetric capacity	kWh L^{-1}	0.9	1.3	2.3
	g H_2 L^{-1}	28	40	70
H_2 delivery temperature (to FC)	ºC	-40 to 85	-40 to 85	-40 to 95-105
Operating pressure (min/max)	MPa	0.5/1.2		
Kinetics	(g H_2 s^{-1}) kW^{-1}	0.02	0.02	0.02

2.1 Hydrogen Storage Technologies

2.1.1 Compressed Hydrogen Gas

Compressing hydrogen is the most common way of storing it. The present generation of fuel cell vehicles use 70 MPa compressed hydrogen tanks to store their hydrogen, which is about 5.6 kg of usable hydrogen [11]. The system volumetric capacity numbers from Table 2.2 show that for 5.6 kg of H_2 the volume of tank and system is about 213 L. While the gravimetric capacity at 350 bar meets the 2015 DOE targets, the volumetric capacity is quite low, and is far from meeting the 2010 targets. At 700 bar the gravimetric capacity of the system decreases and does not meet the 2015 targets due to the extra weight of the tank required to hold the higher pressure. The volumetric system capacity at 700 bar is closer to the 2010 targets.

Table 2.2: Compressed Hydrogen Storage Parameters ([13])

		Compressed H_2		DOE Targets		
Storage Parameter	**Units**	**350 bar**	**700 bar**	**2010**	**2015**	**Ultimate**
System Gravimetric Capacity	wt %	5.5	5.2	4.5	5.5	7.5
System Volumetric Capacity	g H_2 L^{-1}	17.6	26.3	28	40	70

Unfortunately, there is no foreseeable way to increase the capacity of compressed hydrogen systems. Heavier tanks are required as the pressure is increased because thicker tank walls are required, as well the energy losses incurred by going to higher pressures will also lower the overall efficiency [11].

2.1.2 Liquid Hydrogen

Liquid hydrogen is more effective for storage of large amounts of hydrogen. The surface of the tank acts as a heat sink for the tank and as the surface area of the tank increases, the transfer of heat to the hydrogen also increases. This implies that the boil off of the cryogenic liquid is proportional to the surface area to volume ratio of the container. A larger volume has a smaller surface area to volume ratio. This means the heat loss per volume of hydrogen will be less and a large sphere will minimize the surface area for the most hydrogen stored. For a small non spherical container, which may be used in an automobile, the losses increase dramatically [9]. Reported hydrogen losses are about 25% per month for a tank left outside unused in a vehicular application [14]. Table 2.3 shows the gravimetric and volumetric capacities of liquid hydrogen.

Table 2.3: Storage Parameters ([14])

		Liquified H_2	DOE Targets		
Storage Parameter	**Units**		**2010**	**2015**	**Ultimate**
System Gravimetric Capacity	kWh kg^{-1}	2.36	1.5	1.8	2.5
System Volumetric Capacity	kWh L^{-1}	1.48	0.9	1.3	2.3

The efficiency of storing hydrogen as a liquid is poor in relation to other methods because it requires about 1/3 of the energy stored to liquify it. This is due in part to the extremely low boiling point temperature of 22 K which requires a significant amount of energy to reach. Hydrogen also has two nuclear states, one called para-hydrogen and the other ortho-hydrogen. At room temperature the ratio of para to ortho-hydrogen is 1:3. The significance of these two different states becomes apparent during hydrogen liquification. The ground state is para-hydrogen at 0 K, meaning that when hydrogen is cooled to 22 K ortho-hydrogen will convert to para-hydrogen spontaneously. Unfortunately this is an exothermic conversion and the magnitude of the enthalpy increases at lower temperatures. The enthalpy of conversion is higher than the latent heat of vaporization at 22 K, which means that the hydrogen will vaporize no matter how good the insulation of the tank is because the heat generation is originating from within the tank due to this nuclear state change. This requires that cryogenically stored hydrogen be converted to para-hydrogen while it is being stored, and is generally done with the use of catalysts to speed up the change [9].

2.1.3 Liquid Organic Hydrogen Carriers

Liquid Organic Hydrogen Carriers (LOHC) are unsaturated organic compounds that store hydrogen through hydrogenation. A large number of candidates exist, and examples of those with the appropriate requirements such as capacity and vapour pressure are heterocyclic aromatic compounds such as *N*-ethylcarbazole [15, 16]. The hydrogen capacity of

these systems is typically about 5-8 wt% H, and they have physical and handling characteristics similar to diesel or gasoline [16]. These systems require the use of precious metal catalysts such as Ru or Pd for the release/storage of hydrogen [17]. They can also be somewhat volatile leading to potential evaporation of the storage media over time and so require a low vapour pressure and boiling point [16]. Figure 2.1 shows the proposed hydrogenation and dehydrogenation of *N*-ethylcarbazole.

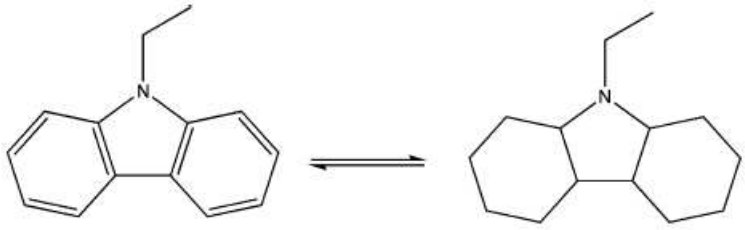

Figure 2.1: Hydrogen storage cycle with *N*-ethylcarbazole [18] [©Industrial & Engineering Chemistry Research, 2012, by permission]

2.1.4 Solid-State Storage

Hydrogen can also be stored in solid material in atomic or molecular form. The advantages are very high volumetric density and low pressure, however, low gravimetric density and high temperature for hydrogen release remain challenges to be solved. The candidate materials for solid-state hydrogen storage can be grouped into four categories: (1) conventional metal hydrides, (2) complex hydrides, (3) sorbents, and (4) chemical hydrides. Table 2.4 provides a summary of these four groups [11]. The criteria listed on the left are the metrics by which hydrogen storage materials can be compared. Each of the groups have their strengths and weaknesses, and choosing one particular group over another will largely depend on application.

Table 2.4: Overview of different hydrogen storage systems ([11])

	Conventional Hydrides	**Complex Hydrides**	**Sorbent Systems**	**Chemical Hydrides**
Vol. Capacity	Good	Good	Fair	Good
Grav. Capacity	Poor	Good	Good	Good
Reversibility	Good	Good	Good	Poor
Thermodynamics	Good	Good	Poor	Fair
Kinetics	Good	Poor	Good	Fair
Efficiency	Good	Good	Good	Poor

Conventional Hydrides

Conventional hydrides are conceptually the simplest systems. They generally consist of a metal host with hydrogen atoms interstitially situated in the crystal lattice structure. Figure 2.2 shows a simple schematic of hydrogen absorption into a metal. Generally, hydrogen is heated in a pressurized vessel containing a metal powder. First molecular hydrogen is adsorbed onto the surface of the metal where it dissociates and diffuses into the host metal. Initially, a so-called α phase is formed where the hydrogen atoms are randomly distributed through out the grain. No change in the crystal structure is associated with this phase. When the solubility limit of dissolved hydrogen in the α phase is reached, a second phase, (β phase) begins to form. The β phase has a different crystallographic structure than that of the α phase. When the metal is completely transformed to the β phase it can no longer hold any more hydrogen.

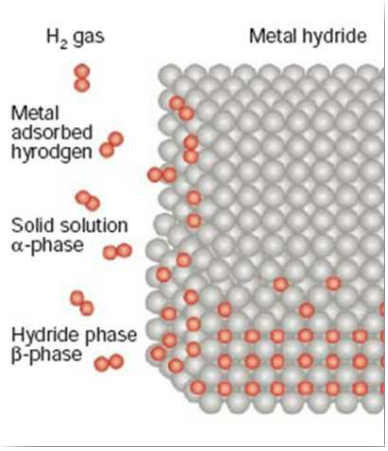

Figure 2.2: Schematic of the hydrogenation of a conventional hydride. Hydrogen is first adsorbed onto the metal surface where it dissociates. It diffuses into the metal and creates the solid solution α phase, upon saturation of the α phase the β phase hydride is formed [19] [©Nature, 2001, by permission]

The general reaction for conventional hydrides is shown in equation 2.1, where M is the metal atom(s) which forms the hydride.

$$M + (x/2)\,H_2 \rightleftharpoons MH_x \tag{2.1}$$

An example system would be $LaNi_5H_6$ which has a capacity of about 1.4 wt% H. It has excellent kinetics and thermodynamics, but the low gravimetric capacity and high cost limit its use [2, 20].

Complex Metal Hydrides

Complex metal hydrides are distinguished from conventional hydrides by having a "complex" anion and a metal cation. An example is $LiBH_4$ which is comprised of the complex anion BH_4^- and the cation Li^+. Figure 2.3 shows a schematic of the $LiBH_4$ structure where the complex anion is clearly seen as a distinct and separate repeating unit in the overall $LiBH_4$ unit cell [21].

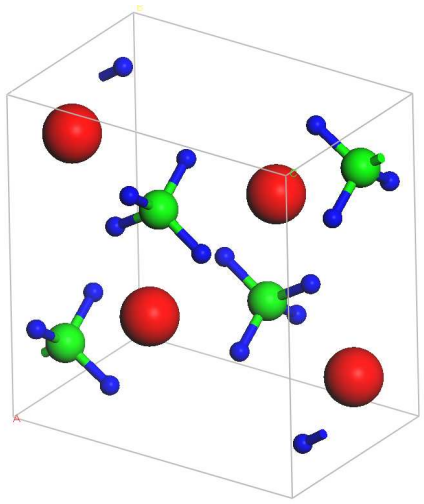

Figure 2.3: Schematic of the orthorhombic $LiBH_4$ showing the atomic locations of Li (red - large), B (green - medium) and H (blue - small)

Complex hydrides are known for their high hydrogen capacities with $LiBH_4$ having a total hydrogen capacity of 18.5 wt%. There are a number of distinct families among the complex hydrides: alanates (AlH_4^-), borohydrides (BH_4^-), and amides (NH_2^-) and imides (NH^{2-}) [22]. It is difficult to achieve hydrogen absorption / desorption reversibility in complex metal hydride based compounds.

Alanate based materials consist of the alanate anion (AlH_4^-) and a metal cation. $NaAlH_4$ is one of the most studied alanate based compounds. Bogdanovic et al. performed extensive research on $NaAlH_4$ and found that mixing it with $TiCl_3$ drastically improved the kinetics of desorption and enabled reversible operation of the system under moderate temperatures and pressures [23]. The dehydrogenation of $NaAlH_4$ to NaH is shown in equations 2.2 and 2.3, the dehydrogenation is a two step reaction involving an intermediate species alanate (Na_3AlH_6).

$$NaAlH_4 \rightleftharpoons {}^1/_3 Na_3AlH_6 + {}^2/_3 Al + H_2 \tag{2.2}$$

$$^1/_3Na_3AlH_6 \rightleftharpoons NaH + ^1/_3Al + ^1/_2H_2 \quad (2.3)$$

Borohydrides are a group of complex hydrides consisting of a BH_4^- complex anion and a metal cation. These materials have high gravimetric capacities because of the presence of light weight boron and a high ratio of H in the complex anion. $LiBH_4$ and $NaBH_4$ are among the most common borohydrides studied. $LiBH_4$ has the highest capacity of the borohydrides. Equation 2.4 shows the partial dehydrogenation of $LiBH_4$ to release 13.9 wt% hydrogen (complete decomposition is 18.5 wt%).

$$LiBH_4 \rightleftharpoons LiH + B + ^3/_2H_2 \quad (2.4)$$

Amides and imides are a group of nitrogen containing hydrides. $LiNH_2$ is lithium amide and Li_2NH is lithium imide. The reaction in equation 2.5 shows the dehydrogenation of the amide to form the imide for about 6.5 wt% hydrogen [2].

$$LiNH_2 + LiH \rightleftharpoons Li_2NH + H_2 \quad (2.5)$$

The low temperature and pressure of desorption for this system has brought it attention as a possible candidate for use in fuel cell systems; however, trace amounts of NH_3 has to be mitigated before use as it is poisonous to the fuel cell's catalyst even in extremely small amounts [2].

2.1.5 Applications of Metal Hydride Storage Systems

Commercial products based on metal hydrides for storage of hydrogen already exist. For example, Palcan Energy Co. has commercialized 600 and 6000 SL sized metal hydride canisters using $LaNi_5$ intermetallic hydride with a gravimetric capacity of about 1 to 1.5 wt%. $LaNi_5$ alloys (and the related AB_5 alloy family) are excellent materials for reversible

absorption / desorption of hydrogen, and form the basis of anode electrodes in rechargeable NiMH (nickel metal hydride) batteries. However, their gravimetric capacity is low (~1.5 wt%) due to presence of heavy metals. Figure 2.4 shows one of Palcan's $LaNi_5$ based storage system.

Figure 2.4: Palcan metal hydride hydrogen storage available in 600-6000 SL sizes using $LaNi_5H_6$ based hydrides. It has about 1 wt% H_2 system capacity [©Palcan, 2012, by permission]

2.2 Thermodynamics of Metal Hydrides

An important figure of merit for metal hydrides is the enthalpy of desorption or absorption. The enthalpy correlates the pressure of hydrogen gas to the temperature of the metal hydride at equilibrium and can be expressed by the van't Hoff equation (2.6):

$$\ln\left(\frac{P}{P_0}\right) = -\frac{\Delta H}{RT} + \frac{\Delta S}{R} \tag{2.6}$$

Where P_0 is the atmospheric pressure, ΔH and ΔS are the enthalpy and entropy change respectively during hydrogenation or dehydrogenation, T is the temperature in Kelvin, and R is the gas constant.

Figure 2.5 shows 3 regions of a typical pressure-composition-temperature (PCT) plot. In region I hydrogen is introduced to the metal and the so called α phase is formed. This is a solid solution phase where the hydrogen is randomly distributed in the metal host's matrix and does not change crystal structure. As the concentration of hydrogen in the metal host increases a new phase (referred to as the β phase) begins to nucleate. The β phase has a different crystal structure than the host metal. The β phase is associated with region II on the PCT diagram and has a fairly constant pressure as the α phase is turned into the β phase. This plateau or constant pressure region signifies a co-existence of both α and β phases. In region III the pressure starts to increase; this corresponds to the full conversion of the α phase to the β phase. The pressure then increases from this point on because no more absorption can take place.

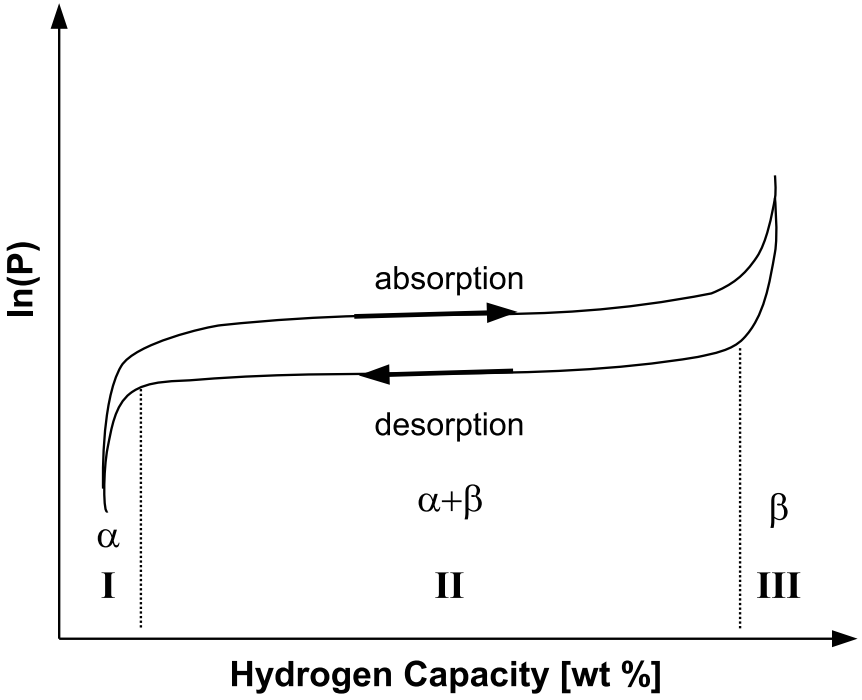

Figure 2.5: Pressure-Composition-Temperature (PCT) curve

For most metal hydrides the enthalpy and entropy of hydrogenation are negative (exother-

mic) and positive for dehydrogenation (endothermic). This means that heat is required to desorb the hydrogen, and it is released during the hydrogen absorption.

Figure 2.5 also shows information about how the reversible capacity of a metal hydride is determined. Reversible capacity of a hydride is the plateau width of the PCT diagram (labeled as region II), and is less than the maximum capacity.

Another phenomena seen in Figure 2.5 is the hysteresis between the absorption and desorption curves. It shows that the hydrogen pressure required for absorption (hydride formation) is greater than that of desorption (decomposition) [2].

The enthalpy value dominates the thermodynamic behavior of a given material. The entropy term is nearly constant (approximately 130 $\mathrm{J\,mol^{-1}K^{-1}}$) for solid-$H_2$ gas systems [24, 20]. If the pressure in equation 2.6 is equal to P_0 (atmospheric pressure), the Van't Hoff relationship can be rearranged to equation 2.7:

$$\Delta H = \Delta S T_{plateau} \tag{2.7}$$

Figure 2.6a shows the PCT data for several different temperatures. The mid-point pressure of each plateau enables one to determine the heat of desorption through a Van't Hoff plot shown in figure 2.6b [2]. The slope and intercept provides ΔH and ΔS, respectively.

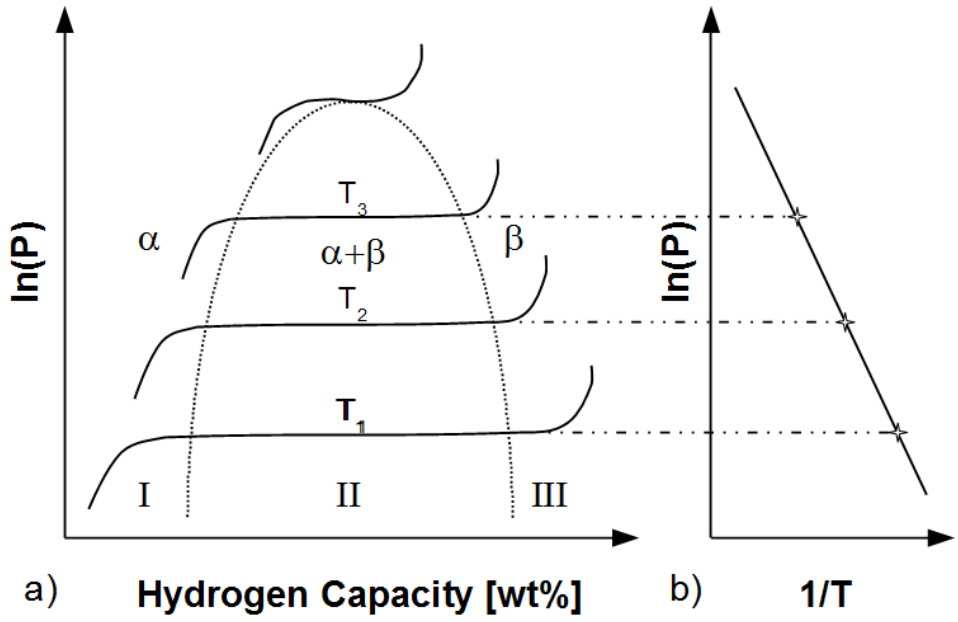

Figure 2.6: PCT (a) and van't Hoff (b) plots for a hydride. (adapted from [19]) [©Nature, 2001, by permission]

The relationship between ΔH and $T_{plateau}$ at atmospheric pressure has shown that as the plateau temperature increases, the magnitude of the hydrogenation enthalpy also increases [2]. It also shows that the enthalpy of decomposition can be used to determine the temperature which corresponds to an equilibrium pressure of 1 bar. This is close to the pressure that a fuel cell will be operating and is a good indication of candidate materials for use in such systems.

This illustrates that the maximum useful enthalpy of formation is limited to about -30 kJ $mol_{H_2}^{-1}$ so that the plateau temperature is kept below 100 ºC to enable the waste heat from a PEM fuel cell to power the dehydrogenation process.

Equations 2.8, 2.9 and 2.10 show the dehydrogenation of MgH_2 along with the calculation of the H_2 desorption enthalpy, respectively.

$$MgH_2 \rightleftharpoons Mg + H_2 \tag{2.8}$$

$$\Delta H_{des} = \Delta H_{f,products} - \Delta H_{f,reactants} \tag{2.9}$$

$$= \left(\Delta H_{Mg} + \Delta H_{H_2}\right) - \left(\Delta H_{MgH_2}\right) = 74\,\text{kJ}\,\text{mol}_{H_2}^{-1} \tag{2.10}$$

The enthalpy of desorption specifically refers to the change in energy that occurs from the release of hydrogen from a hydride and is the enthalpy of formation of the products minus the enthalpy of formation of the reactants. It is usually normalized by dividing by the number of moles of hydrogen released (ΔH_{des} $\text{mol}_{H_2}^{-1}$).

2.2.1 Thermodynamic Destabilization

One of the major goals in solid state hydrogen storage research today is to tune the thermodynamics of a hydride system such that a suitable temperature of desorption for use with a polymer electrolyte membrane (PEM) fuel cell is obtained. This translates into a hydride that can use the waste heat from the fuel cell to evolve the hydrogen, which means that it has an equilibrium pressure above 1 bar at temperatures lower than 100 ºC. Many compounds of interest (such as MgH_2, $LiBH_4$, ...) have desorption temperatures well above 100 ºC making them difficult to use. These high temperatures stem from the high enthalpies of desorption and absorption.

One method to alter the thermodynamics of absorption and desorption is referred to as thermodynamic destabilization. A metal hydride can be destabilized by introducing other compounds that will alter the end products of dehydrogenation. This idea is conceptually presented in Figure 2.7. Dehydrogenation of two systems, AH_2 and AH_x + xB are shown in Figure 2.7. The reactions and the corresponding enthalpies are:

$$AH_2 \rightleftharpoons A + H_2 \qquad \Delta H_{des} = (\Delta H_A + \Delta H_{H_2}) - \Delta H_{AH_2}$$
$$AH_2 + xB \rightleftharpoons AB_x + H_2 \quad \Delta H_{des} = (\Delta H_{AB_x} + \Delta H_{H_2}) - (\Delta H_{AH_2} + \Delta H_{xB})$$

It is the addition of B to the system that lowers the enthalpy of the reaction through the formation of AB_x, and this is shown schematically by the middle line in Figure 2.7. A decrease in desorption temperature proportional to the change in enthalpy occurs.

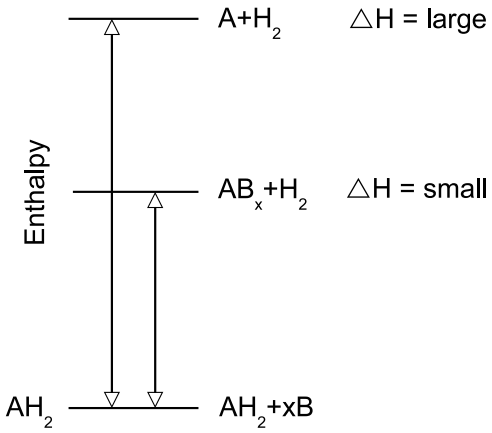

Figure 2.7: The effect of thermodynamic destabilization on enthalpy of formation [6] [©Scripta Materialia, 2007, by permission]

One example of thermodynamic destabilization is for the $LiBH_4$ / MgH_2 system. The temperature of desorption for $LiBH_4$ is about 450 ºC and the temperature of desorption for MgH_2 is about 280 ºC. When the two are combined the temperature of desorption for the system is 225 ºC, showing a lowering of the temperature required to obtain hydrogen absorption and desorption [4].

2.3 Kinetics

Enthalpy of reaction provides no information about the reaction kinetics (rate of hydrogen desorption / absorption). The rate of many chemical reactions is dominated by the pres-

ence of activation barriers in the reaction pathway. The H_2 absorption and desorption of many compounds are examples of chemical reactions which show significantly high activation barriers. Figure 2.8 shows a typical activation barrier for a generic system, where the activation energy, E_a, quantifies the value of the barrier.

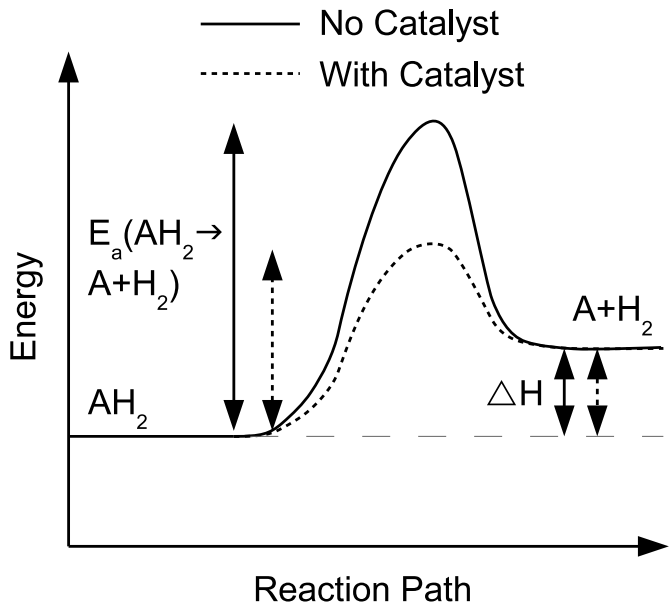

Figure 2.8: Activation energy (E_a) and enthalpy (ΔH) diagram of the reaction $AH_2 \rightleftharpoons A+H_2$

Figure 2.8 also shows the effect of a catalyst on the system. Addition of a catalyst has no effect on the thermodynamics of the system as the nature of the reactants and products (i.e., ΔH) is unchanged, but the activation energy is reduced. Although a system may have favourable thermodynamic properties, the reaction kinetics may be too slow for reasonable dehydrogenation (and rehydrogenation) to occur.

2.3.1 Kissinger Analysis

The activation energy for the desorption of a hydride can be obtained through performing the Kissinger analysis. A series of samples are tested at different heating rates β_{ramp}, where

the maximum temperature T of desorption for each sample shifts with the change in heating rate [24, 2]. Figure 2.9a shows the effect of heating rate on the temperature of desorption in this research for as received MgH_2. As the heating rate increases, the peak temperature also increases.

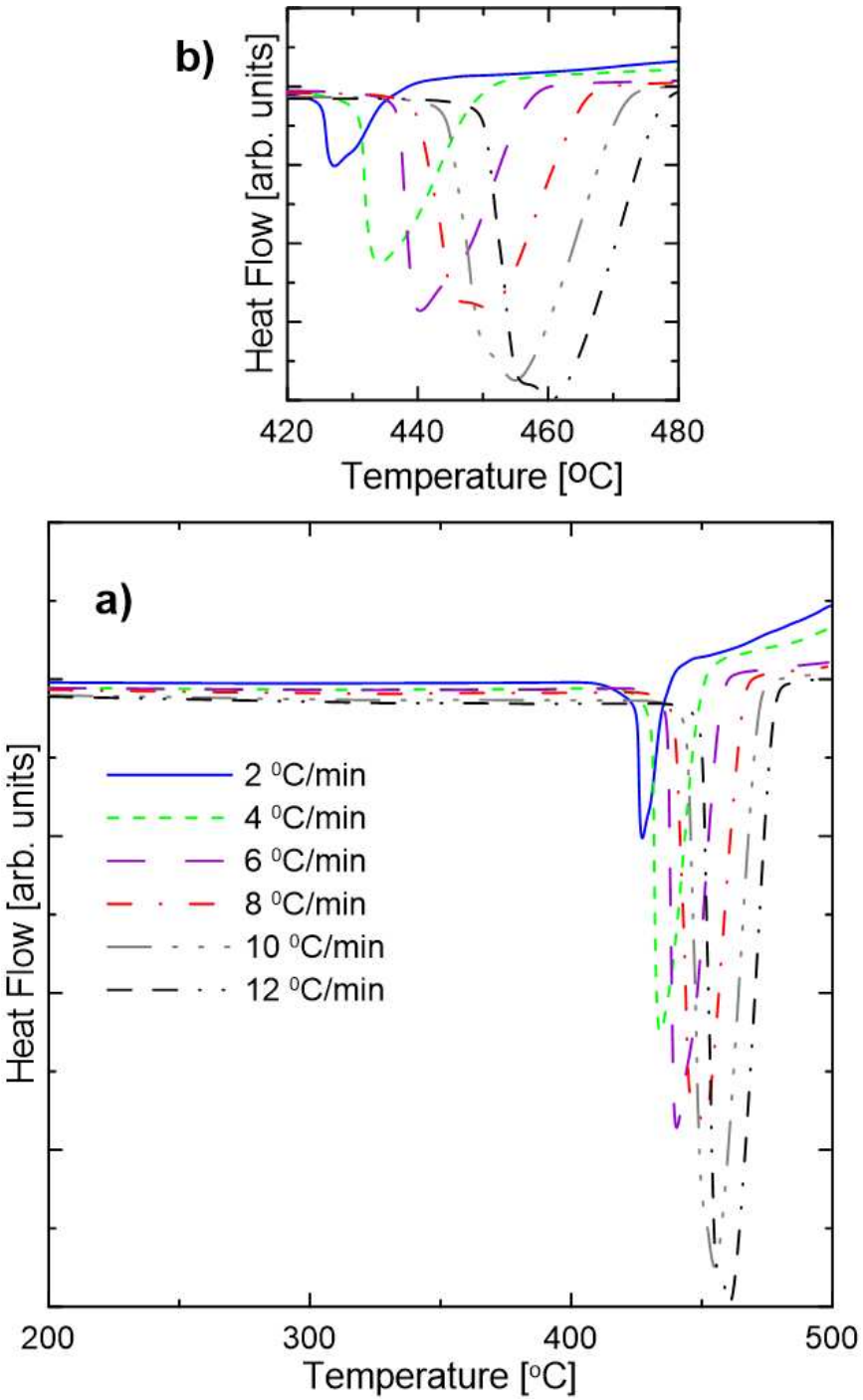

Figure 2.9: a) MgH_2 heated at several different rates for Kissinger analysis. b) closeup showing increased peak temperature with heating rate

Equation 2.11 shows the relationship between the activation energy E_a and the peak's temperature (T_{max}) [24]. Here β_{ramp} is the heating rate, T_{max} is the temperature of desorption, E_a is the activation energy, R is the universal gas constant, and k_0 is a constant.

$$\ln\left(\frac{\beta_{ramp}}{T_{max}}\right) = -\left(\frac{E_a}{RT_{max}}\right) + \ln(k_0) \tag{2.11}$$

A plot of $\ln(\beta_{ramp}/T_{max})$ against $1000/T_{max}$ has a slope of E_a/R from which the activation energy can be determined. Alternatively we could differentiate equation 2.12 to obtain [2]:

$$\frac{d\ln\left(\frac{\beta}{T_{max}^2}\right)}{d\left(\frac{1}{T_{max}}\right)} = \frac{E_a}{R} \tag{2.12}$$

Now a plot of $\ln(\beta_{ramp}/T_{max}^2)$ vs. $1000/T_{max}$ will be linear with a slope of E_a/R. Figure 2.10 shows the the Kissinger plot from the DSC scans in Figure 2.9.

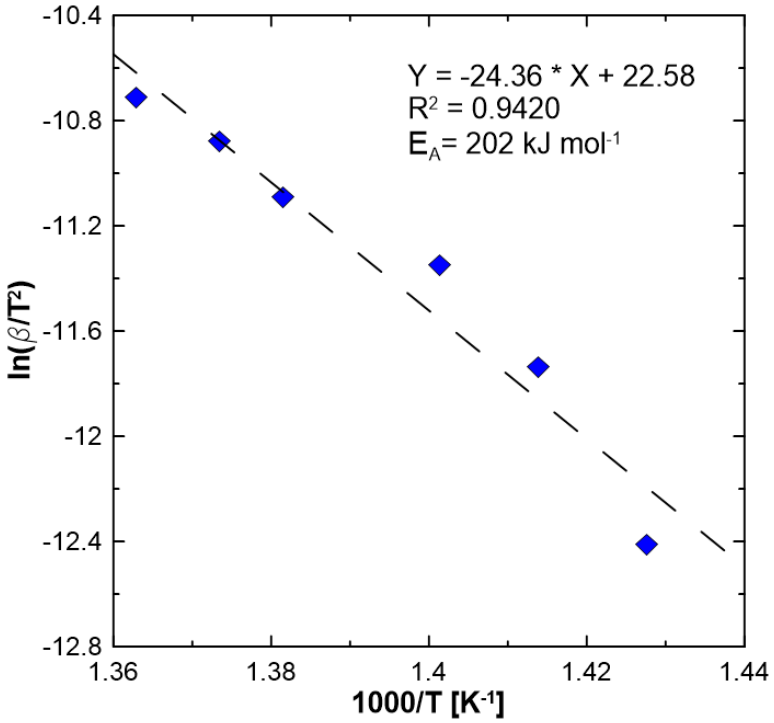

Figure 2.10: Kissinger analysis for as received MgH_2 for the data shown in Figure 2.9

2.4 Previously Studied Complex Hydride Systems

2.4.1 $LiBH_4$

$LiBH_4$ has the highest known gravimetric hydrogen capacity (18.5 wt%) among hydrides (excluding beryllium containing compounds as they are toxic). However, it has a high desorption temperature and is very difficult to regenerate, requiring temperatures and pressures around 690 ºC and 200 bar [20]. The temperature at which $LiBH_4$ desorbs hydrogen at 1 bar is about 450 ºC [4]. The bonding in $LiBH_4$ is described as ionic between the $[BH_4]^-$ and $[Li]^+$ ions and as covalent between the B and H atoms [25]. The high desorption temperature and the difficult regeneration make this hydride unsuitable for vehicular applications (see Table 2.1 in introduction). Table 2.5 is a summary of hydrogen storage parameters for

$LiBH_4$.

Table 2.5: Thermodynamic Data For $LiBH_4$ [22]

	ΔH_{des} **[kJ mol$_{H_2}{}^{-1}$]**	**Measured Temperature [°C]**	**Wt %**
$LiBH_4 \rightleftharpoons LiH + B + {}^3/_2H_2$	67-69 [5, 9]	400-500 [2]	13.9
$LiH \rightleftharpoons Li + H$	90.625 [26]	>727 [2]	4.6

Figure 2.11 shows the desorption path and associated enthalpy for each step of desorption. $LiBH_4$ melts before the release of hydrogen.

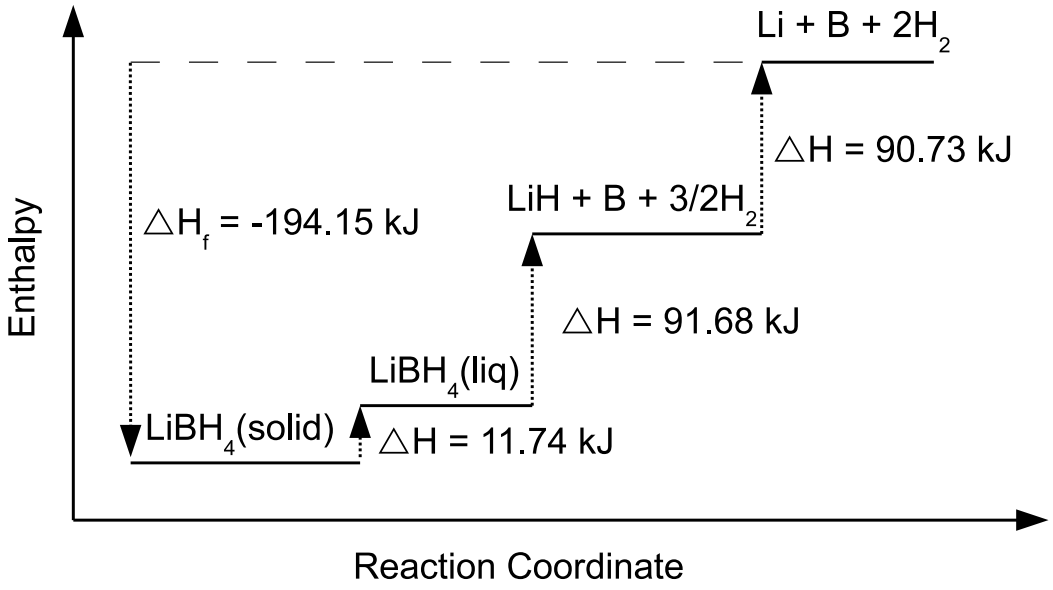

Figure 2.11: Enthalpy diagram for $LiBH_4$ showing the enthalpy for each step of a desorption as well as the structural and phase changes.

The differential scanning calorimetry (DSC) analyses for $LiBH_4$ has three endothermic peaks. The first peak corresponds to a structural change from orthorhombic to hexagonal, the second peak is the fusion (melting) of $LiBH_4$, and the third peak is due to the release of hydrogen [27].

2.4.2 $LiBH_4$ / MgH_2

$LiBH_4$ has one of the highest gravimetric hydrogen contents known (18.5 wt%) and would make an excellent candidate for hydrogen storage if a) the temperature of desorption was lower and b) if rehydrogenation was more practical. MgH_2 is another compound with a relatively high gravimetric hydrogen content of 7.66 wt% with desorption / absorption temperatures and pressures substantially lower than that of $LiBH_4$.

The composite mixture of $LiBH_4$+MgH_2, however, has a theoretical equilibrium desorption temperature of 225 ºC at 1 bar. This desorption reaction is shown below:

$$2LiBH_4 + MgH_2 \rightleftharpoons MgB_2 + 2LiH + 4H_2 \tag{2.13}$$

The exothermic formation of the compound MgB_2 reduces the overall desorption enthalpy through thermodynamic destabilization. The enthalpy of desorption for reaction 2.13 is 46 kJ $mol_{H_2}^{-1}$ [4], which is much lower than that of $LiBH_4$ at 69 kJ $mol_{H_2}^{-1}$. Table 2.6 is a summary of hydrogen storage parameters for the $2LiBH_4$ / MgH_2 system.

Table 2.6: Thermodynamic Data For $2NaBH_4$ / MgH_2

	ΔH_{des} **[kJ** $\mathbf{mol_{H_2}^{-1}}$**]**	**Measured Temperature [ºC]**	**Wt %**
$2LiBH_4 + MgH_2 \rightleftharpoons 2Li + MgB_2 + 5H_2$	n/a	n/a	14.4
$2LiBH_4 + MgH_2 \rightleftharpoons 2LiH + MgB_2 + 4H_2$	46	270 [5]	11.5

Calorimetric studies of $LiBH_4$ / MgH_2 show three endothermic peaks similar to those observed in $LiBH_4$. The peaks correspond to a phase change, melting of $LiBH_4$, and dehydrogenation. No distinct peaks related to the formation of MgB_2 were observed [28]. When compared to $LiBH_4$ the temperature of desorption is about 100 ºC lower indicating thermodynamic destabilization has occurred.

In order to form MgB_2 in the $LiBH_4$ / MgH_2 system, a back pressure of about 2-3 bar of hydrogen is required during desorption [5]. Under 1 bar back pressure amorphous B is formed and a loss of capacity is observed because the amorphous boron will not reform into $LiBH_4$ during absorption [5, 29]. When the back pressure was too low, the dehydrogenation of $LiBH_4$ to LiH and amorphous B was kinetically preferred over the reaction with Mg. Pinkerton et. al. argue that the back pressure kinetically suppresses the decomposition of $LiBH_4$ and allows Mg to react and form MgB_2 before LiH and B are formed [29].

While the thermodynamics and reversibility are improved, the desorption and absorption temperature are still too high to meet the DOE targets. However, this system is an excellent example that thermodynamic destabilization is an effective way of improving the unfavourable thermodynamic properties of hydrogen storage materials.

2.4.3 $NaBH_4$

Sodium borohydride ($NaBH_4$) is a complex hydride with a hydrogen content of about 10.66 wt%. The desorption temperature of $NaBH_4$ is about 200 ºC higher than that of $LiBH_4$ thus making it less attractive as a hydrogen storage material. What makes it more attractive however, is the use of Na instead of Li. There are concerns about the abundance of lithium because of its use in lithium ion battery applications [10], and Na is a cheaper and much more abundant replacement. Urgnani et al. reported that the standard enthalpy of formation for $NaBH_4$ is 191.8 kJ $mol_{H_2}{}^{-1}$ [30]. According to Milanese et al. the decomposition enthalpy of $NaBH_4$ to Na and B is 106.8 kJ $mol_{H_2}^{-1}$ [31]. A summary of thermodynamic data for $NaBH_4$ is shown in Table 2.7.

Table 2.7: Thermodynamic Data For $NaBH_4$

	ΔH_{des} **[kJ mol$_{H_2}{}^{-1}$]**	**Measured Temperature [ºC]**	**Wt %**
$NaBH_4 \rightleftharpoons NaH + B + {}^3/_2H_2$	88.2 [32]	-	8
$NaH \rightleftharpoons Na + {}^1/_2H_2$	114 [33]	> 400 [33]	4.2
$NaBH_4 \rightleftharpoons Na + B + 2H_2$	106.8 [31]	577 [2, 31]	10.8

Calorimetric studies of $NaBH_4$ decomposition show that desorption occurs at temperatures approaching 600 ºC. A small amount of hydrogen (0.25 wt%) evolution occurs around 500 ºC when $NaBH_4$ begins to melt [31, 2].

2.4.4 $NaBH_4$ / MgH_2

Similar to $LiBH_4$+MgH_2, thermodynamic destabilization also occurs in the $NaBH_4$+MgH_2 system. Reaction 2.14 shows the hydrogen desorption reaction of this composite [32]. The formation of MgB_2 is similar to that of the $LiBH_4$+MgB_2 system. MgB_2 acts as a destabilizing agent by lowering the temperature of desorption to 450 - 490 ºC [32, 34], which is about 100 ºC lower than for $NaBH_4$ alone. Calorimetric studies of this system show one endotherm which corresponds to the decomposition of MgH_2 and a second endotherm at $\simeq$ 500 ºC corresponding to the desorption of hydrogen from $NaBH_4$ [31].

$$2NaBH_4 + MgH_2 \rightleftharpoons MgB_2 + 2Na + 5H_2 \tag{2.14}$$

According to Mao et al., the enthalpy of desorption for $2NaBH_4$ + MgH_2 is 100.58 kJ $mol_{H_2}^{-1}$ with 5 mol% TiF_3 added as a catalyst [34], which is lower than that of $NaBH_4$ which has a decomposition enthalpy of 106.8 kJ $mol_{H_2}^{-1}$ [31]. The enthalpy of decomposition determined by Milanese et al. is 90.9 kJ $mol_{H_2}^{-1}$ [31] for $2NaBH_4$ + MgH_2. According to Garroni et al. the decomposition enthalpy for $2NaBH_4$+MgH_2 is 62 kJ $mol_{H_2}^{-1}$ with a corresponding *theoretical* desorption temperature of 350 ºC at 1 bar [35]. Thermodynamic

data for the $2NaBH_4$+MgH_2 system are summarized in Table 2.8.

Table 2.8: Thermodynamic Data For $2NaBH_4$+MgH_2

	ΔH_{des} **[kJ mol$^{-1}_{H_2}$]**	**Measured Temperature [ºC]**	**Wt %**
$2NaBH_4 + MgH_2 \rightleftharpoons 2Na + MgB_2 + 5H_2$	62-100.58 [35, 31, 34]	450 - 490 [35, 34, 31]	9.88
$2NaBH_4 + MgH_2 \rightleftharpoons 2NaH + MgB_2 + 4H_2$	64 [26]	n/a	7.91

Garroni et al. report that varying the stoichiometry of the system from 2:1 $NaBH_4$:MgH_2 to 1:2 significantly changed the sorption properties of the system [35] changing the reaction pathways and corresponding temperatures of desorption. It was reported that hydrogen desorption in the 1:2 mixture completes significantly faster than the 2:1 mixture, although the 2:1 mixture has a lower calculated enthalpy (62 vs. 69 kJ mol$_{H_2}{}^{-1}$) [35, 31]. Powder agglomeration and the presence of more MgH_2, which has been shown to correlate with the kinetics of $NaBH_4$ decomposition, are two reasons for the observed difference in the kinetics [35].

Absorption for the 2:1 and 1:2 systems were carried out isothermally at 450 ºC under 50 bar H_2 pressure for 1 hour. The 2:1 mixture has significantly better reversibility. It is speculated that the formation $NaMgH_3$ is one of the reasons that full absorption is not achieved as it is not can not hold as much hydrogen [35].

2.4.5 Mg_2NiH_4

Mg_2NiH_4 has been the focus of intense research for hydrogen storage due to its relatively low desorption temperature when compared to MgH_2 [36, 37, 38, 22, 39, 4, 3]. Recently, it has also been shown to be a very effective destabilizing agent for $LiBH_4$. Thermodynamic data of Mg_2NiH_4 and MgH_2 are is shown in Table 2.9.

Table 2.9: Thermodynamic Data for Mg_2NiH_4

	ΔH_{des} **[kJ mol$_{H_2}{}^{-1}$]**	**Measured Temperature [ºC]**	**Wt %**
$Mg_2NiH_4 \rightleftharpoons Mg_2Ni + 2H_2$	64.5 - 65.8 [2, 40]	280 [20]	3.6
$MgH_2 \rightleftharpoons Mg + H_2$	74 [2]	310	7.66

Calorimetric measurements of Mg_2NiH_4 show that at about 235 ºC Mg_2NiH_4 undergoes a phase transformation from monoclinic to fcc cubic [38], after which dehydrogenation occurs at about 280 ºC.

Mg_2NiH_4 is not commercially available and can be synthesized through the ball milling of MgH_2 and Ni and high temperature and pressure cycling of the milled mixture at a temperature of 495 ºC and a pressure of 95 bar. As well the ball milling of Mg and Ni in a 2:1 stoichiometric ratio respectively to form Mg_2Ni and hydrogenating it under 30 bar hydrogen and 350 ºC will form Mg_2NiH_4 [38].

2.4.6 $LiBH_4$ / Mg_2NiH_4

Mg_2NiH_4 has been shown to destabilize $LiBH_4$ more effectively than MgH_2 [4]. The proposed desorption steps for the system are:

Step 1 at 250ºC:

$$4LiBH_4 + 5Mg_2NiH_4 \rightleftharpoons 2MgNi_{2.5}B_2 + 4LiH + 8MgH_2 + 8H_2 \tag{2.15}$$

Step 2 at 340ºC:

$$MgH_2 \rightleftharpoons Mg + H_2 \tag{2.16}$$

The formation of $MgNi_{2.5}B_2$ leads to a lower enthalpy of desorption than the $LiBH_4$ + MgH_2 system. This can be seen in table 2.10 where row C shows hydrogen release at an

enthalpy of 15 kJ $mol_{H_2}^{-1}$. According to Vajo et al. [4], the compound $MgNi_{2.5}B_2$ is twice as stable as MgB_2 on a per atom basis, meaning that it will destabilize the system more. This follows Miedema's rule *less stable alloys form more stable hydrides* [20]; or in this case *more stable alloys form less stable hydrides*. It can also be seen in table 2.10 (row B) that the addition of Ni not alloyed with MgH_2 has no effect on the thermodynamics because in this case it is only acting as a catalyst for the system.

Table 2.10: Enthalpy of desorption shown for the dehydrogenation of three composite systems: $LiBH_4/MgH_2$, $LiBH_4/MgH_2/Ni$, and $LiBH_4/Mg_2NiH_4$

	Composite System	ΔH_{des} **[kJ** $\mathbf{mol_{H_2}^{-1}}$**]**
A	$2LiBH_4 + MgH_2 \rightleftharpoons$	46
	$2LiH + MgB_2 + 4H_2$	
B	$2LiBH_4 + MgH_2 + 2.5Ni \rightleftharpoons$	46
	$2LiH + MgB_2 + 2.5Ni + 4H_2$	
C	$4LiBH_4 + 5Mg_2NiH_4 \rightleftharpoons$	15
	$4LiH + 8MgH_2 + 2Mg_{2.5}NiB_2 + 8H_2$	

Hydrogen desorption in $4LiBH_4$+$5Mg_2NiH_4$ initiates at a temperature of about 250 ºC and has a ΔH_{des} of about 15 kJ $mol_{H_2}^{-1}$. This corresponds to a theoretical desorption temperature of -25 ºC [4]. However, room temperature desorption is not observed due to kinetic limitations.

Table 2.11: Thermodynamic Data for $4LiBH_4$+$5Mg_2NiH_4$ [4]

	ΔH_{des} **[kJ** $\mathbf{mol_{H_2}^{-1}}$**]**	**Measured Temperature [ºC]**	**Wt %**
$4LiBH_4 + 5Mg_2NiH_4 \rightleftharpoons$ $4LiH + 8MgH_2 + 2Mg_{2.5}NiB_2 + 8H_2$	15	250	2.5

2.5 Thesis Objectives

The main objective of this thesis was to use the concept of thermodynamic destabilization to lower the enthalpy of the $NaBH_4$ / Mg_2NiH_4 system to a temperature of about 100 ºC for use with a PEM fuel cell. The objectives were as follows:

1. Develop and synthesize novel complex hydride system based on Vajo et al.'s work [4]with $LiBH_4$ using Mg_2NiH_4 as a thermodynamic destabilizer.

2. Synthesize Mg_2NiH_4 based on literature review and characterize it through XRD, DSC, and Sievert's apparatus.

3. Determine the effect of ball milling on the complex hydride system in terms of kinetics, hydrogen capacity, phase changes, grain size and particle size.

4. Determine the need for a hydrogen back pressure in the system for the formation of destabilizing compounds (i.e., MgB_2).

5. Demonstrate thermodynamic destabilization of the complex hydride system.

6. Evaluate the cyclability of the complex hydride system in terms of reversible capacity and phase changes during cycling.

7. Evaluate the hydrogen desorption kinetics of the complex hydride system.

8. Examine the crystallographic phase changes that occur during decomposition of the complex hydride system to determine the reaction path during desorption and absorption of hydrogen.

Chapter 3

Experimental Methods

A number of experimental techniques and analytical tools are available to synthesize and characterize materials for hydrogen storage research. Here, an overview of the techniques used in this research are presented. For synthesis of metal hydrides and complex metal hydride systems, ball milling is an effective and relatively simple mechanism to mix and prepare new materials. It is also the most common method of sample preparation for metal hydride based hydrogen storage materials. Manometric methods, where one measures the pressure changes during absorption and desorption of hydrogen is commonly used to measure the hydrogen capacity of a storage material. The data obtained from manometric measurements can be used to determine the thermodynamics and kinetics of hydrogen uptake / release, making it ideal for such studies. The crystallographic phase changes that occur during hydrogenation and dehydrogenation are determined through X-ray diffraction (XRD). Differential scanning calorimetry (DSC) analysis is also very helpful in determining the heat of absorption and desorption. This technique can also be used to obtain the activation energy. Thermogravimetric analyses () measures the change in mass of a sample during heating and can directly measure the hydrogen storage capacity of a metal hydride.

3.1 Materials Synthesis

3.1.1 Mg_2NiH_4 synthesis

Mg_2NiH_4 is not commercially available and had to be synthesized and characterized in the lab. Mg_2NiH_4 was synthesized with ball milling appropriate amounts of MgH_2 (Acros 90% rest Mg) and Ni (Acros 99.9%, -325 mesh) powders. The stoichiometric ratio for MgH_2 to Ni was 2:1. For a total mass of 2.4 g, 1.135 g MgH_2 and 1.265 g of Ni are required. The powders were weighed and placed into a stainless steel ball mill jar with three 8 g stainless steel balls and milled for one hour in a SPEX 8000^{TM} shaker mill. After milling the mixture was loaded into a stainless steel sample holder and heated to 495 ºC under 95 bar of pressure for 4 hours in the PCTPro 2000 apparatus. The powder was then kept at 495 ºC for 4 hours to desorb all the hydrogen, and then was at 495 ºC and 95 bar for 4 hours for hydrogen absorption to take place. All powder handling was performed in an Ar glove box with less than 0.1% O_2 and a constant Ar flow rate of about 100 ml min^{-1}. XRD was used to verify that Mg_2NiH_4 was made.

3.1.2 $4NaBH_4$ / $5Mg_2NiH_4$ synthesis

$NaBH_4$ (Acros, 98+%) was used as-received and mixed in an argon filled glovebox with the synthesized Mg_2NiH_4 in a 4:5 stoichiometric ratio. The mixture was then ball milled for up to 2 hours in a SPEX 8000™ ball mill with a ball to powder ratio of 10:1.

3.2 Experimental Methodologies

3.2.1 Ball Milling Experiments

Ball milling experiments with different time periods were conducted to investigate the impact of high energy ball milling on the hydrogen desorption / absorption properties. Data

were collected from manometric measurements in the PCTPro 2000 to determine variations in the hydrogen desorption temperature. XRD was used for compositional or phase analysis, as well as grain size analysis. DSC was used to correlate phase changes with PCT data as well as determining the heat of reaction. Particle size analysis was performed with an SEM.

A 2.4 g mixture of $4NaBH_4$ / $5Mg_2NiH_4$ was ball milled for 10, 30, 60 and 120 minutes. A small amount of powder (about 0.31 g) was removed after each interval for XRD, SEM and DSC analysis, while the rest remained in the ball mill jar for further milling. The powder to ball ratio was kept approximately the same by removing a ball when the ball to powder ratio was changed significantly. Table 3.1 shows the ball to powder ratio and milling times for these experiments.

Table 3.1: Ball mill study ball to powder ratio

mill time [min]	**amount of powder [g]**	**number of balls (8 g each)**	**ball to powder ratio**
10	2.4	3	10:1
30	2.09	3	11.5:1
60	1.78	2	9:1
120	1.47	2	10.9:1

Ball mills can be quite loud. In order to lower the noise from the ball mill an acoustic isolation chamber was constructed as discussed in appendix C.2.

3.2.2 Thermodynamic Studies (Pressure Composition Temperature)

Pressure composition isotherm studies were made in order to determine the enthalpy of hydrogen absorption / desorption reactions. The PCT Pro 2000 was used to collect the isotherm data. Desorption and absorption isotherms were made at 350, 400, 450 and 475 ºC and at 400, 450 and 475 ºC, respectively. Desorption and absorption parameters used with the PCTPro 2000 are summarized in tables 3.2 and 3.3, respectively. The heading

f(ΔP) refers to the algorithm used to compute the aliquot pressure in the PCTPro 2000 during desorption and absorption isotherms and is dependent on the change in concentration versus change in pressure (dC/dP).

Table 3.2: PCT isotherm desorption parameters used with the PCT Pro 2000

Sample Temperature [ºC]	**$P_{reservoir}$ [bar]**	**P_{sample} [bar]**	**f(ΔP) [bar]**	**Reservoir Volume [ml]**
350	20	20	1.5	11.7
400	50	50	1.5	11.7
450	75	75	1.5	11.7
475	95	95	1.5	11.7

Table 3.3: PCT isotherm absorption parameters used with the PCT Pro 2000

Sample Temperature [ºC]	**$P_{reservoir}$ [bar]**	**P_{sample} [bar]**	**f(ΔP) [bar]**	**Reservoir Volume [ml]**
400	vacuum	vacuum	1.5	11.7
450	vacuum	vacuum	1.5	11.7
475	vacuum	vacuum	1.5	11.7

3.2.3 Hydrogen Back Pressure Experiments

The impact of back pressure on the formation of boride (MgB_2, $MgNi_{2.5}B_{2.5}$) phases during the hydrogen desorption experiments will be studied. Back pressures examined were vacuum, 1 bar and 5 bar. TPD experiments were used to determine the amount of hydrogen released as a function of time and temperature. XRD will be used to determine the crystallographic phases formed upon dehydrogenation.

3.2.4 Reservoir Volume Effects

The impact of the PCTPro 2000 reservoir volumes were examined using the system's 11.7, 167.7 and 1056.3 ml reservoirs. The size of the reservoirs impacts the gas pressure and is

important in hydrogen desorption of $4NaBH_4$ / $5Mg_2NiH_4$ composites.

3.2.5 Hydrogen Absorption and Desorption Cycling Studies

The $4NaBH_4$ / $5Mg_2NiH_4$ composite system was cycled several times to determine loss of capacity. XRD was used to determine the phases present in the system in the hydrogenated and dehydrogenated state after cycling.

The PCTPro 2000 was used for both non-equilibrium TPD and isothermal cycling experiments. For the TPD cycling experiments the sample started with a hydrogen back pressure of 1 bar in the 11.7 ml reservoir volume and was heated at a rate of 6 ºC min^{-1} to 450 ºC for desorption to happen. After this an absorption step was conducted at 400 ºC and 55 bar. The sample was then cooled under pressure. This desorption / absorption cycle was repeated four times. The difference between the TPD cycling tests and the isothermal tests were the heating and cooling of the sample between the cycles.

The isothermal cycling tests in the PCTPro 2000 were set to automatically charge and discharge the sample chamber with hydrogen at a constant temperature of 450 ºC. Initially, the sample was heated at 6 ºC min^{-1} to 450 ºC under a hydrogen back pressure of 1 bar to desorb hydrogen. Three isothermal cycling tests were performed:

- Experiment a: A hydrogen back pressure of 1-2 bar in the 1056.3 ml reservoir volume for all desorptions, and a hydrogen absorption of about 84 bar with the 167.7 ml reservoir.

- Experiment b: The first desorption was into 1 bar hydrogen back pressure while the remaining desorptions were under a hydrogen back pressure of about 4.5 bar. All desorptions were into the 167.7 ml reservoir, while the absorption pressure was about 84 bar in the 167.7 ml reservoir as well.

- Experiment c: The first desorption was into 1 bar hydrogen back pressure, but the

remaining isothermal back pressures for desorption were at about 3.5 bar with the absorption set at about 57 bar. The desorption reservoir volume for test C was 167.7 ml and the absorption volume was 11.7 ml.

Table 3.4: Parameters for the isothermal cycling studies

Test	1st TPD Deso back pressure [bar]	Isothermal Deso back pressure [bar]	Desorption Volume [ml]	Absorption Pressure [bar]	Absorption Volume [ml]
a	1	1-2	1056.3	84	167.7
b	1	4.5	167.7	84	167.7
c	1	3.5	167.7	57	11.7

3.2.6 Hydrogen Desorption Kinetics

The kinetics of hydrogen desorption were examined by the Kissinger analysis. Heat of reactions were measured with a DSC equipment using heating rates of 4, 6, 8 and 10 ºC min^{-1}. See section 3.3.5 for more details on the DSC experiments.

3.2.7 Crystallographic Phase and Reaction Path Analysis

X-Ray diffraction studies were performed for various stages of hydrogen desorption in the $4NaBH_4$ / $5Mg_2NiH_4$ composite. Samples were heated to a desired temperature (e.g., 350, 400, ...ºC), and equilibriated for 1 hour. Then the sample was evacuated and allowed to cool down. The sample was placed in an airtight holder and directly placed in the XRD machine.

3.3 Equipment Used

3.3.1 PCTPro 2000 Pressure Composition Temperature (PCT) machine

A PCTPro 2000 Sieverts instrument by Setaram was used to measure gas sorption properties of materials studied in this thesis. Thermodynamic properties and capacity analysis of

the complex hydride system were derived from the data. For temperature programmed desorption (TPD) analysis a ramp rate of 6 ºC to a temperature of 450 ºC or 500 ºC under a back pressure of vacuum, 1 bar or 5 bar was used. For more information on the use of the PCT machine see Appendix A.2. Figure 3.1 shows the PCT Pro 2000 machine used.

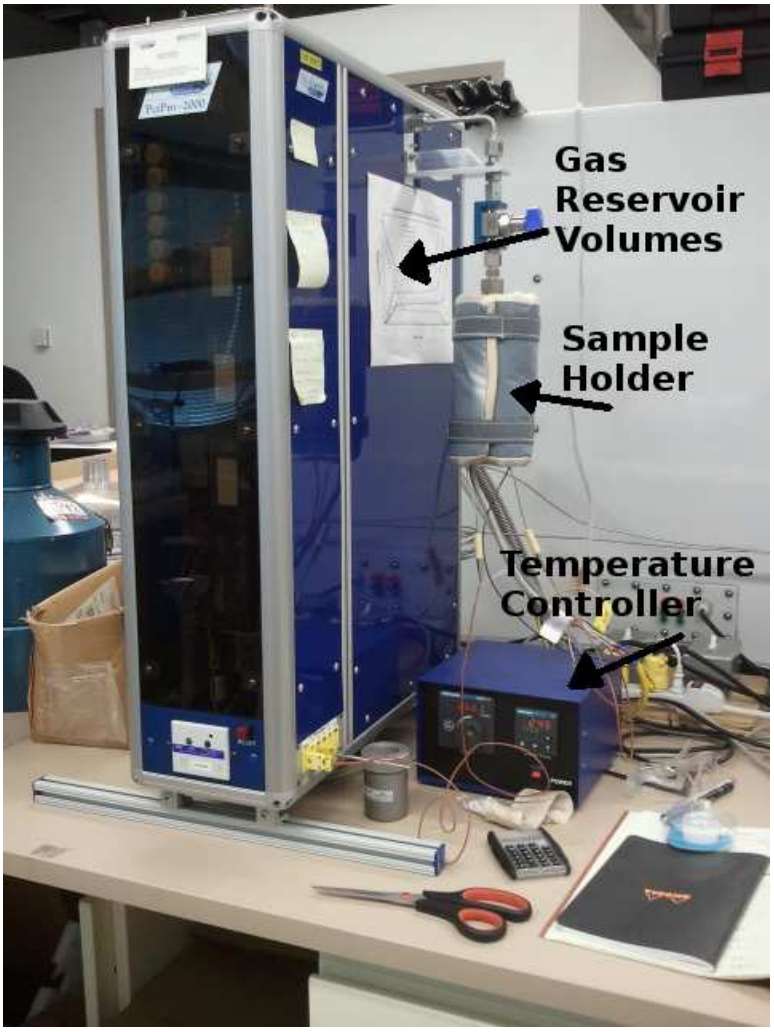

Figure 3.1: Setaram PCT Pro 2000 Pressure Composition Temperature (PCT) machine

Figure 3.2 shows a cross section of the autoclave and sample holder in the PCTPro 2000. The sample holder is inside the autoclave with two spacers on top of it to minimize

the dead volume. The sample holder's lid is a porous stainless steel filter which prevents the spread of powders to the rest of the machine, and allows for the passage of gas in/out of the sample holder. The autoclave is heated with a band heater which is wrapped in an insulation jacket (Figure 3.1).

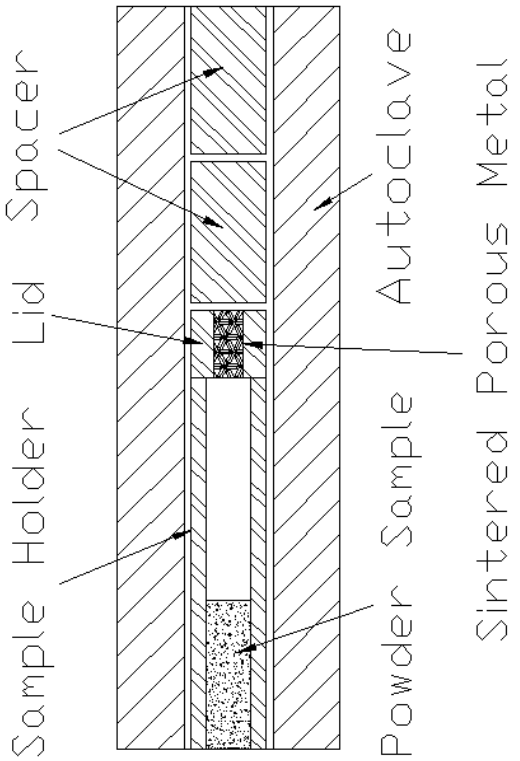

Figure 3.2: Autoclave diagram showing spacers and sample holder location.

Accuracy and Resolution

The PCTPro 2000 is equipped with 4 capacitance pressure transducers. Two of these transducers are used by the PID controlled electronic pressure regulator in the PCT Pro 2000. The other two are used for data collection, and include a high pressure sensor with a maximum range of 0 - 200 bar (MKS 870 microbaraton) and a low pressure sensor (MKS 890

microbaraton) for high sensitivity with a range of 0 - 5 bar. The accuracy of the transducers is 1.0% of the reading. The resolution of the lower pressure transducer (MKS 890 microbaraton) is about 1.1×10^{-4} bar and the resolution of the high pressure transducer (MKS 870 microbaraton) is about 33×10^{-4} bar.

3.3.2 Argon Glove Box

An argon glove box (Hydrogen Electrics LLC) was used to keep all of the samples in an air and moisture reduced environment. The oxygen content was measured using an Expedition Oxygen Analyzer sensor by OxyCheq with a resolution of 0.1% O_2. The oxygen level was kept below 0.3% and was typically at 0.1% or lower. The argon glove box is designed to have a constant argon purge through it at a rate of about 100 ml min^{-1}. The purity of argon used was 99.9998%.

Figure 3.3: Argon glovebox

3.3.3 Ball Mill

A SPEX 8000® shaker ball mill was used to prepare the samples. The ball to powder ratio was 10:1, and 10 minutes to 2 hour milling times were used. The jar used with the machine is loaded in the glovebox and sealed with an o-ring under the lid to keep it air tight. A stainless steel jar and balls were used. See Appendix A.1 for more details on ball milling.

3.3.4 X-Ray Diffractometer

A Bruker D8 Advance with a 0.6 mm slit, a Vantec-1 X-ray detector and a Cu Kα (λ = 1.5418 Å) X-ray source were used. The data was analyzed by EVA (version 14) and powder diffraction file (PDF) database version 9. The diffraction scans were made with a 0.02º step increment and a speed of 0.1 sec step^{-1} from 10 to 90º. See Appendix A.3 for more information on the fundamentals of XRD.

3.3.5 Differential Scanning Calorimeter (DSC)

DSC measurements were conducted with a TA instruments DSC Q10 (V9.9 Build 303). An argon flow of 50 ml min^{-1} was used during the measurements. The software used for determining peak positions was Universal Analysis 2000 version 4.5A. Typically about 8-11 mg of sample was loaded into an aluminum sample holder in an argon glove box and an aluminum lid was placed on top. This was then placed into an air tight transfer container (see section D) and transported to the DSC machine where the airtight holder was opened and the sample inside was placed into the DSC's sample chamber. The sample chamber was then purged with argon for at least 5 minutes. Ramp rates used varied from 4 - 10 ºC min^{-1}. The samples were all heated to 500 ºC.

3.3.6 Thermal Gravimetric Analysis (TGA) / DSC

A Setaram SETSYS Evolution TGA with simultaneous TGA / DSC capability was used for thermogravimetric and DSC analysis. The TGA sample chamber was evacuated and then purged with an argon flow of 50 ml min^{-1}. Heating rates of 4, 6, 8 and 10 ºC min^{-1} were used. The samples were all heated to 500 ºC. Typically about 6-10 mg of sample was loaded into an alumina sample holder with and without an alumina lid. This was then placed into an air tight transfer container (see section D) and transported to the TGA / DSC machine where the airtight holder was opened and the sample inside was placed onto the TGA / DSC's balance. The chamber was then closed and evacuated. The TGA / DSC was programmed in zones as follows:

- Zone 1
  - Evacuate sample for 20 minutes
  - Purge with argon for 30 minutes
  - Heat to 120 ºC at about 12 ºC min^{-1}
  - Hold for 30 minutes
- Zone 2
  - Heat at 4, 6, 8 or 10 ºC min^{-1} to 500 ºC
  - Hold for 10 minutes at 500 ºC
  - Cool to 50 ºC at 10 ºC min^{-1}
- Zone 3
  - Hold at 50 ºC for 40 minutes
  - Ramp at 12 ºC min^{-1} to 120 ºC
  - Hold for 30 minutes
- Zone 4
  - Heat at 4, 6, 8 or 10 ºC min^{-1} to 500 ºC

– Hold for 10 minutes at 500 ºC
– Cool to room temperature at 10 ºC min^{-1}
– End

Figure 3.4 shows the program schematically.

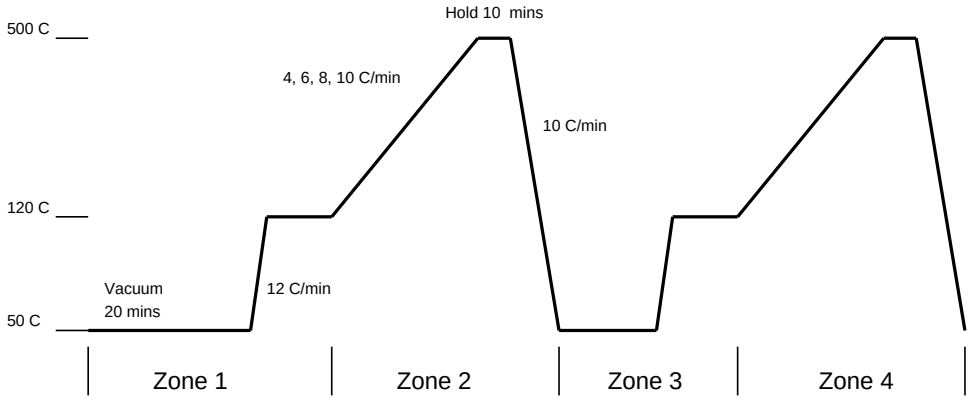

Figure 3.4: TGA/DSC temperature program

To correct for the buoyancy effects, which arises from heating of the chamber flow gas, as empty sample holder is scanned using the same heating profile of the sample. The empty holder data are then subtracted from the sample measurements to obtain the sample mass loss during the heating.

Chapter 4

Results and Discussion

4.1 The Proposed Binary System: $NaBH_4$ / Mg_2NiH_4

Vajo et al.'s success with the thermodynamic destabilization of the $LiBH_4$ / Mg_2NiH_4 system (see section 2.4.6) naturally leads to the question of what other compounds could show similar destabilization effects. Given lithium's relative scarcity compared to sodium, it seems relevant to consider the performance of a $NaBH_4$ / Mg_2NiH_4 composite system. The theoretical hydrogen storage capacity of this system is 4.5 and 5.1 wt%, when the end products consist of NaH and Na, respectively. A possible dehydrogenation reaction could be:

Step 1:

$$4NaBH_4 + 5Mg_2NiH_4 \rightleftharpoons 2MgNi_{2.5}B_2 + 4NaH + 8MgH_2 + 8H_2 \tag{4.1}$$

Step 2:

$$MgH_2 \rightleftharpoons Mg + H_2 \tag{4.2}$$

Table 4.1: Thermodynamic data for $NaBH_4$ and Mg_2NiH_4 under 1 bar hydrogen

	ΔH_{des} [kJ mol$_{H_2}{}^{-1}$]	Measured Temperature [ºC]	Hydrogen Capacity [wt%]
$NaBH_4 \rightarrow NaH + B + 3/2H$	-88.2 [32]	240 - 500 [32, 20]	7.9
$Mg_2NiH_4 \rightleftharpoons Mg_2Ni + 2H_2$	-65 [4, 22]	280 [20]	3.6

The reaction $NaBH_4 \rightharpoonup NaH + B + 3/2H_2$ is irreversible due to the formation of amorphous elemental boron. However, according to Garroni et al. [32], MgB_2 can be formed when MgH_2 is added to $NaBH_4$ as seen in reaction 4.3. Vajo et al.'s research with $LiBH_4$ and $LiBH_4$ / MgH_2 shows that these systems decompose to form amorphous boron and MgB_2, respectively, as well [5]. This indicates some similarity in the reactions of $LiBH_4$ and $NaBH_4$ based compounds. Because the $NaBH_4$ / MgH_2 system is reversible, due to the formation of MgB_2, Barkhordarian et al. achieved direct absorption in the $NaBH_4$ / MgH_2 system at 300 ºC and 200 bar of hydrogen in 48 hours [8].

$$2NaBH_4 + MgH_2 \rightleftharpoons 2NaH + MgB_2 + 4H_2 \tag{4.3}$$

Vajo et al.'s work with $4LiBH_4$ / $5Mg_2NiH_4$ has shown the formation of the ternary boride compound $MgNi_{2.5}B_2$ after decomposition. The similarity between the previously mentioned $NaBH_4$ / $LiBH_4$ / MgH_2 systems suggests that a $4NaBH_4$ / $5Mg_2NiH_4$ system will emulate the $4LiBH_4$ / $5Mg_2NiH_4$ system and produce $MgNi_{2.5}B_2$ as a product of decomposition. The enthalpy of desorption for the $4NaBH_4$ / $5Mg_2NiH_4$ system can be readily calculated when the product of decomposition is $MgNi_{2.5}B_2$, and is shown below in equation 4.4.

$$\Delta H_{des} = \left(2\Delta H_{f,MgNi_{2.5}B_2} + 4\Delta H_{f,NaH} + 8\Delta H_{f,MgH_2}\right) - \left(4\Delta H_{f,NaBH_4} + 5\Delta H_{f,Mg_2NiH_4}\right) \tag{4.4}$$

Using the data summarized in table 4.2, ΔH_{des} for reaction 4.4 is calculated and pre-

sented in table 4.3. The data for NaH, $NaBH_4$ and MgH_2 were obtained from the NIST-JANAF Thermochemical Tables [26], and the data for Mg_2NiH_4 and $MgNi_{2.5}B_2$ were obtained from Vajo et al. [4].

Table 4.2: Thermodynamic data used for the $4NaBH_4$ / $5Mg_2NiH_4$ desorption reaction

Compound	Δ**H**$_f$	**Standard Deviation**
	[kJ mol^{-1}]	**[kJ mol^{-1}]**
NaH	-56.4	$\pm$ 0.08
$NaBH_4$	-191.84	$\pm$ 0.39
Mg_2NiH_4	-196	n/a
$MgNi_{2.5}B_2$	-323	n/a
MgH_2	-76.15	$\pm$ 9.2

Table 4.3: Results for enthalpy of desorption calculation

Δ**H**$_{des}$	**[kJ mol$^{-1}_{H_2}$]**
Δ**H**$_{des}$ **low**	24
Δ**H**$_{des}$ **high**	43

It can be seen in Table 4.3 that depending on the choice of enthalpies from literature, there are two values for ΔH_{des}. They are within the range of enthalpies considered acceptable for hydrogen storage (see section 2.2) and therefore further investigation into this system is needed.

The $NaBH_4$ / Mg_2NiH_4 composite was characterized by Temperature Programmed Desorption (TPD), differential scanning calorimetry (DSC), X-ray diffraction (XRD) and scanning electron microscopy (SEM). The results are discussed in this chapter.

4.2 Preparation and Characterization of Mg_2NiH_4

Figure 4.1 shows the XRD profile of the Mg_2NiH_4 synthesized in the lab. The sample is dominantly monoclinic Mg_2NiH_4 with a small presence of hexagonal $Mg_2NiH_{0.3}$, which is

the incomplete transformation of the MgH_2 and Ni into Mg_2NiH_4. The Mg_2NiH_4 synthesized is orange in color as mentioned by Sato et al. [41].

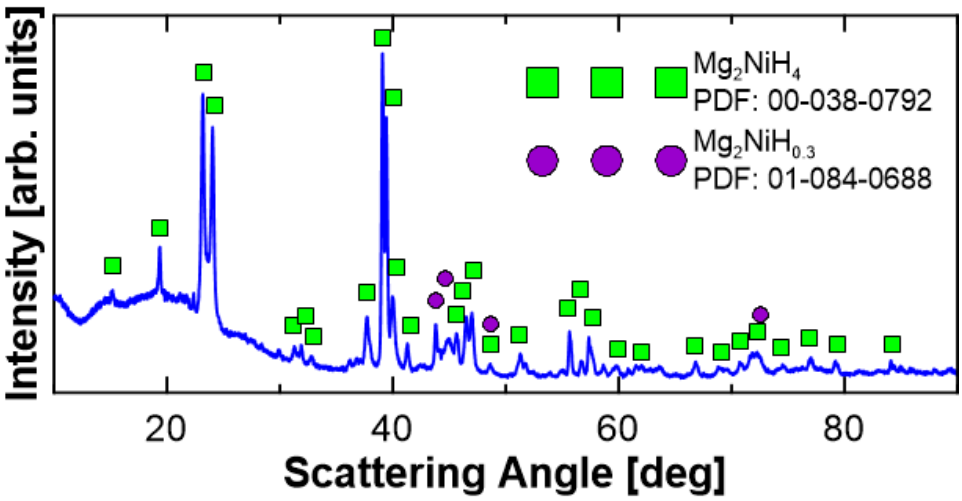

Figure 4.1: XRD scan of synthesized Mg_2NiH_4 showing a dominant presence of the monoclinic Mg_2NiH_4 phase and a small fraction of the hexagonal $Mg_2NiH_{0.3}$ phase (deg in 2θ).

Figure 4.2 shows the XRD scan of Mg_2NiH_4 after a TPD to 450 ºC. Mg_2Ni is dominant, along with a small amount of Mg_2NiH_4 and $Mg_2NiH_{0.3}$. It is not clear why there is Mg_2NiH_4 and $Mg_2NiH_{0.3}$ remaining after desorption, however, it is possible that hydrogen diffusion from the cores of Mg_2NiH_4 and $Mg_2NiH_{0.3}$ becomes the limiting step in the desorption of hydrogen. Figure 4.3 illustrates this scenario.

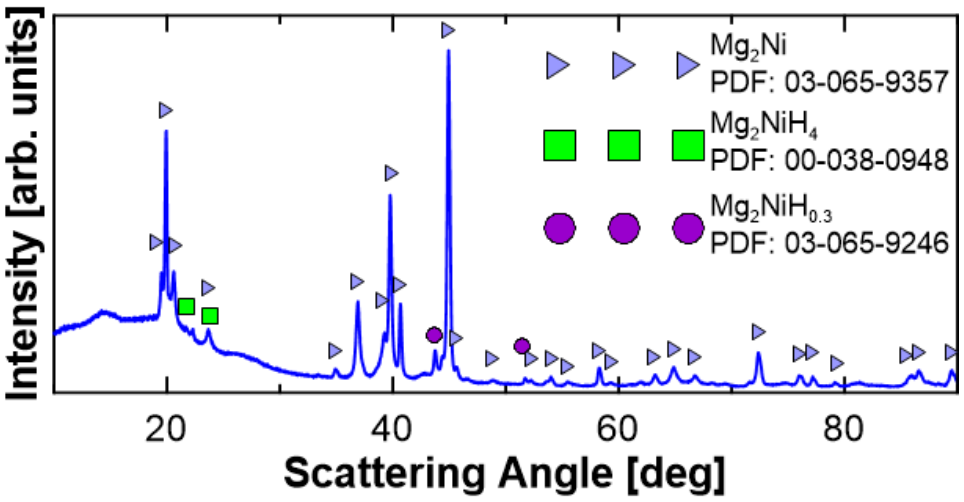

Figure 4.2: XRD scan of Mg_2NiH_4 after hydrogen desorption at 450 ºC (deg in 2θ).

Varin et al. have reported that after ball milling MgH_2, a γ-MgH_2 phase is formed, and when the γ-MgH_2 decomposes a small fraction of it forms an ultra-stable β-MgH_2 that does not break down during heating [2]. The Mg_2NiH_4 and $Mg_2NiH_{0.3}$ phases, however, are not the product of another phase introduced by ball milling and may have formed during the cooling period before sample removal with the small amounts of hydrogen left in the sample chamber after evacuation.

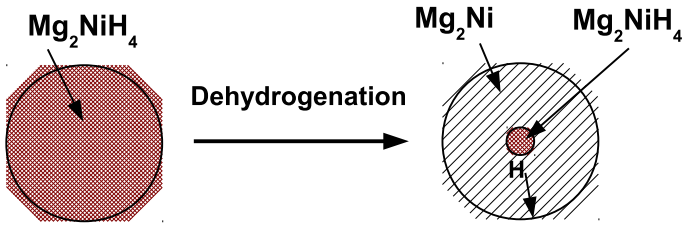

Figure 4.3: The dehydrogenation of Mg_2NiH_4 may be limited through mass transport of hydrogen.

Figure 4.4 shows the PCT isotherms that were measured for Mg_2NiH_4. The absorption

plateaus are higher than the desorption plateaus indicating a hysteresis between absorption and desorption enthalpy is present. This phenomenon is common in metal hydrides and is not fully understood. One explanation is plastic or elastic deformation of the crystal lattice during hydrogen absorption and desorption. As the hydrogen enters the crystal lattice it must expand to accommodate it, and conversely as it leaves during desorption the crystal lattice contracts behind it. The plastic and elastic energies required for the insertion and removal of hydrogen are different leading to different values of enthalpy for hydrogenation and dehydrogenation [20].

The theoretical capacity for Mg_2NiH_4 is 3.6 wt % H, and the observed capacity ranged from about 3 to 3.6 wt %. The desorption isotherm at 450 ºC shows a capacity of about 0.5 wt % H. The reason for this is unclear, but may be due to an incomplete absorption before the desorption test. However, the plateau pressure could still be read so it was not repeated due to time constraints.

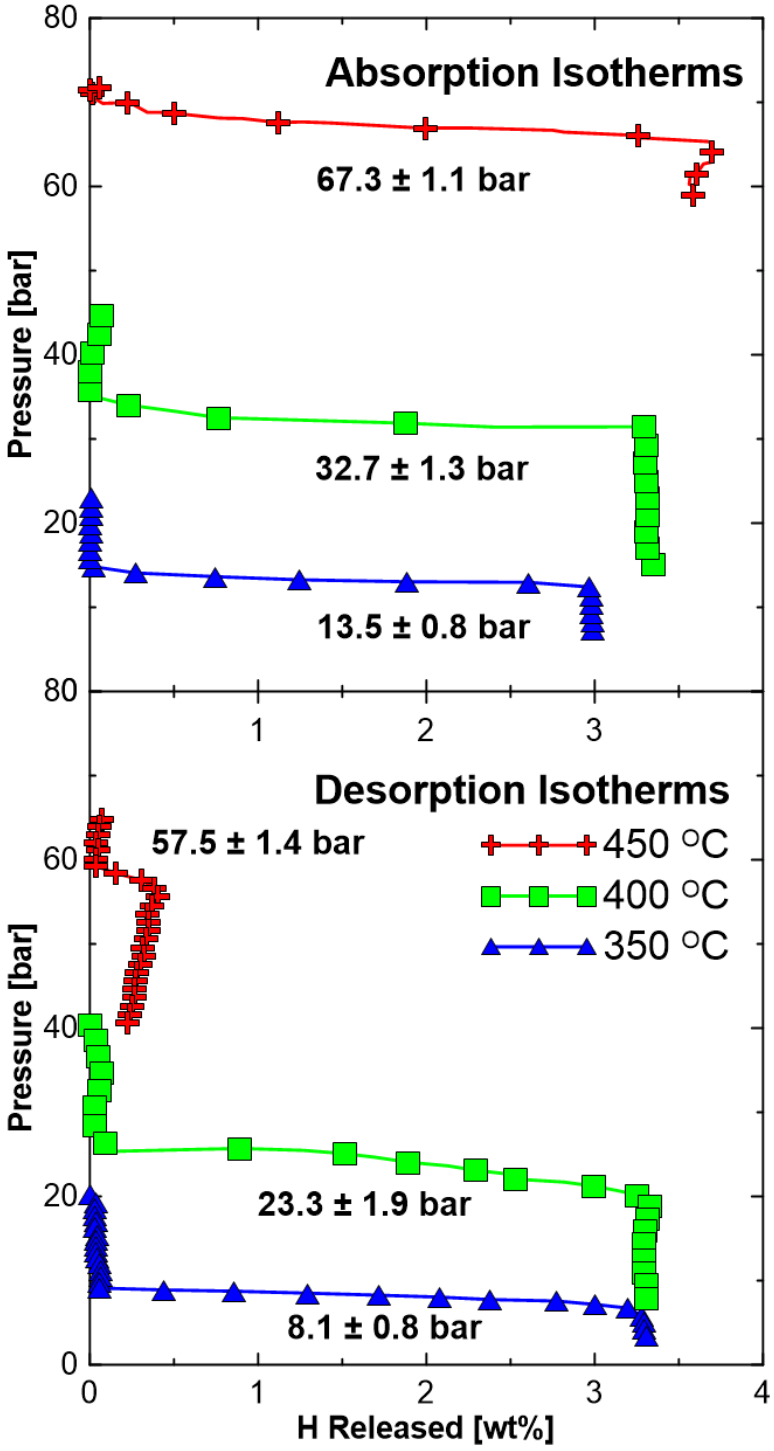

Figure 4.4: Mg_2NiH_4 absorption and desorption isotherms with the plateau pressures and standard deviations shown for the 350, 400 and 450 ºC tests.

Figure 4.5 shows the van't Hoff analysis for Mg_2NiH_4 obtained from the results shown in Figure 4.4. The desorption and absorption enthalpies obtained are 74 $\pm$ 5 kJ $mol_{H_2}^{-1}$ and -60 $\pm$ 3 kJ $mol_{H_2}^{-1}$ respectively. The absorption value is close to the value reported by Reilly and Wiswall of -64.5 kJ $mol_{H_2}^{-1}$ for enthalpy of formation [39]. The error bars are the standard deviation of the data set chosen to represent the plateaus from the absorption and desorption isotherms.

The change in entropy associated with the decomposition of Mg_2NiH_4 is 135 $\pm$ 7 J $mol_{H_2}^{-1}$ K^{-1}, which is very close to 130 J $mol_{H_2}^{-1}$ K^{-1} that most metal hydrides exhibit [2].

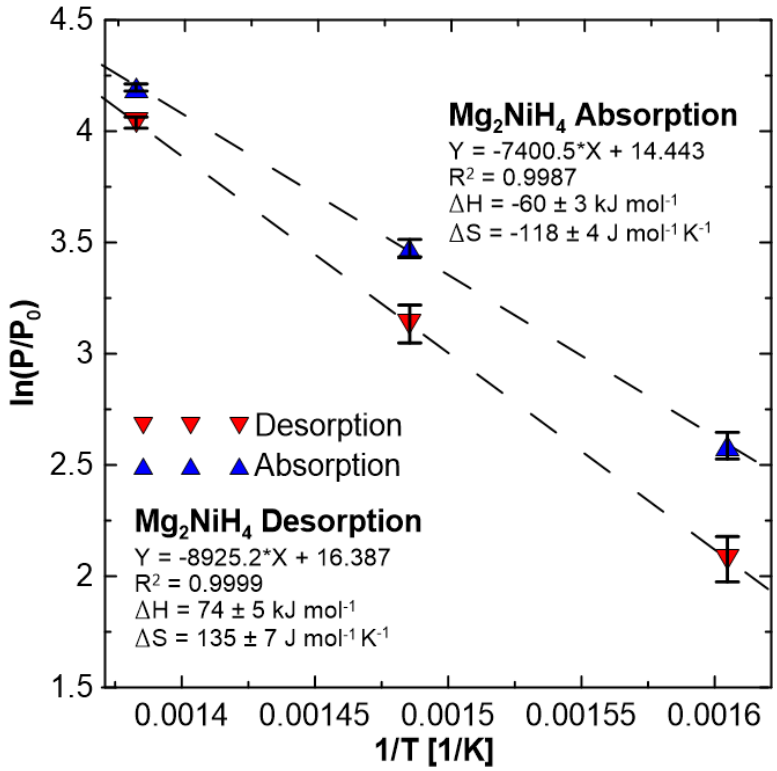

Figure 4.5: Van't Hoff analysis for Mg_2NiH_4

The kinetics of hydrogen desorption from Mg_2NiH_4 were studied by the differential calorimetric method. The activation energy of hydrogen desorption from Mg_2NiH_4 was

obtained from a Kissinger analysis as described in section 2.3.1. Figure 4.6 shows the DSC scans for Mg_2NiH_4 at four different scan rates β = 4, 6, 8 and 10 ºC min^{-1}. The peaks at I occur at about 235 ºC and according to Cermak and Kral, indicate a monoclinic to face centered cubic (fcc) phase transformation [41]. The peaks at II are the dehydrogenation of Mg_2NiH_4 and occur at about 280 ºC. The peaks at location III are unknown and are not reported in literature. These peaks are likely a result of the Mg_2Ni reacting with the aluminum sample holder used for the DSC experiment. An alumina crucible was used in a different DSC machine with Mg_2NiH_4 and no peak at III was observed.

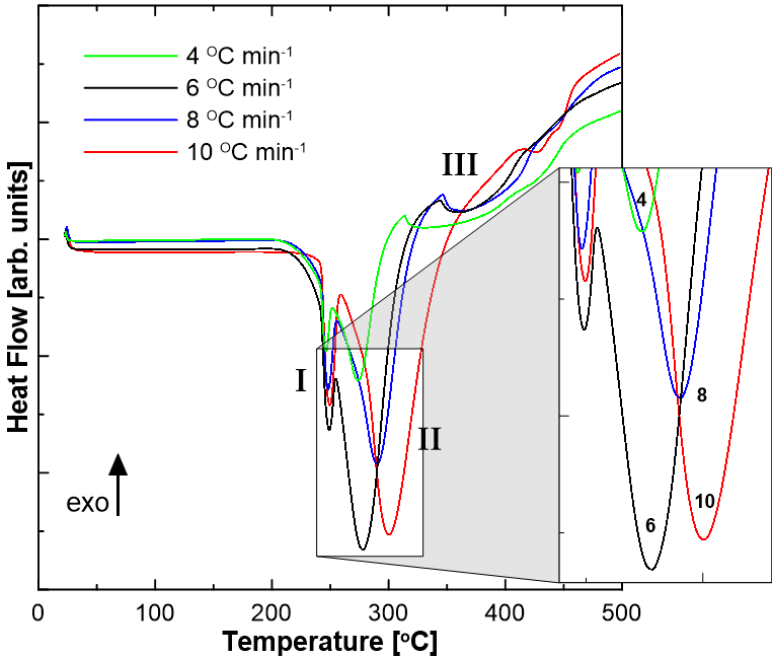

Figure 4.6: DSC scans at the heating rates 4, 6, 8 and 10 ºC min^{-1} for Kissinger analysis

Figure 4.7 shows the fitted data for the calculation of activation energy and it is 73 ± 9 kJ mol^{-1}. For an estimated error of ± 2 ºC in the peak position, the resulting error in activation energy is ± 9 kJ mol^{-1}. Errors are due to inhomogeneities in the powder resulting in inconsistencies in its hydrogen storage properties. The history of the sample

can influence the properties as well, for instance if it has been exposed to air or moisture either while in transport or through long periods of storage.

The activation energy for the synthesized Mg_2NiH_4 is different from that reported by Selvam et al. They obtained 183 kJ mol^{-1} for their Mg_2NiH_4 [40]. The discrepancy might be a consequence of the methodology used to synthesize the powder. Selvam et al. did not use ball milling in their procedure but rather started from finely ground Mg_2Ni which would have significantly different kinetic properties than ball milled powder. The difference in the size of the particles, the number of grain boundaries, and the presence of an oxide layer can play a large role in the activation energy of a metal hydride [2] and is discussed further in the section 4.6 on ball milling.

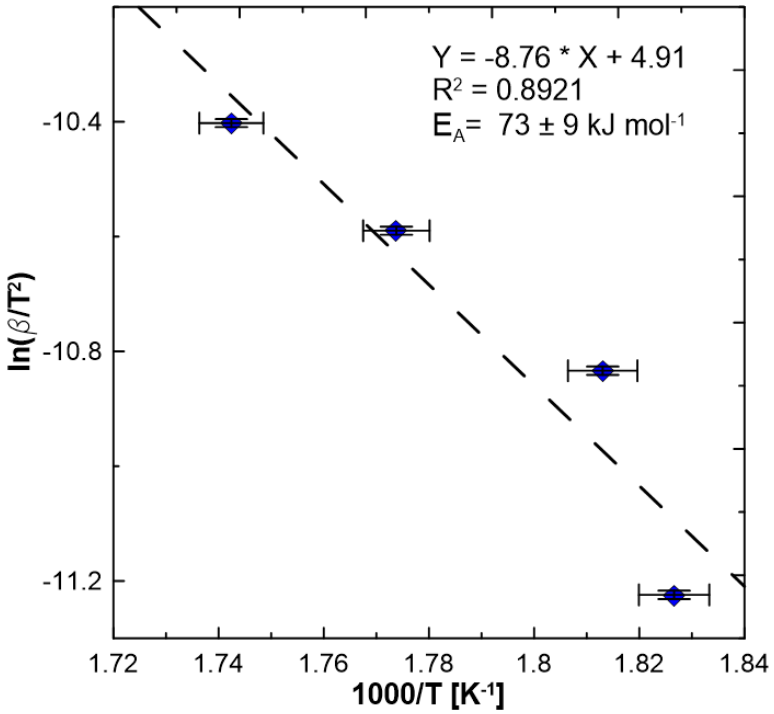

Figure 4.7: Kissinger analysis of the Mg_2NiH_4 DSC data presented in Figure 4.6.

4.3 Crystallographic Phases and Reaction Pathways

Figure 4.8 shows the XRD patterns of the as synthesized $4NaBH_4$ / $5Mg_2NiH_4$ composite (ball milled for 1 hour), heated to 300, 400 and 450 ºC under 1 bar hydrogen. The XRD pattern of the as-synthesized $4NaBH_4$ / $5Mg_2NiH_4$ composite shows peaks for Mg_2NiH_4 and $NaBH_4$, as well as the partially hydrogenated Mg_2Ni compound $Mg_2NiH_{0.3}$. The presence of $Mg_2NiH_{0.3}$ was observed in the as-synthesized Mg_2NiH_4 and is due to incomplete hydrogenation. By 300 ºC the Mg_2NiH_4 has decomposed into Mg_2Ni, while the $NaBH_4$ remains unchanged at this temperature. By 400 ºC the ternary boride phase $MgNi_{2.5}B_2$ has formed and only trace amounts of $NaBH_4$ and Mg_2Ni remain. A small amount of NaH is observed, suggesting that up to 400 ºC the $NaBH_4$ has not decomposed to Na. Excess Mg from the decomposition of Mg_2Ni to $MgNi_{2.5}B_2$ is also observed. By 450 ºC $NaBH_4$ and Mg_2Ni have completely decomposed into $MgNi_{2.5}B_2$, Mg, and Na / NaH. The XRD scan shows NaOH, which is likely due to reduction with oxygen and moisture contamination during handling and transport for analysis.

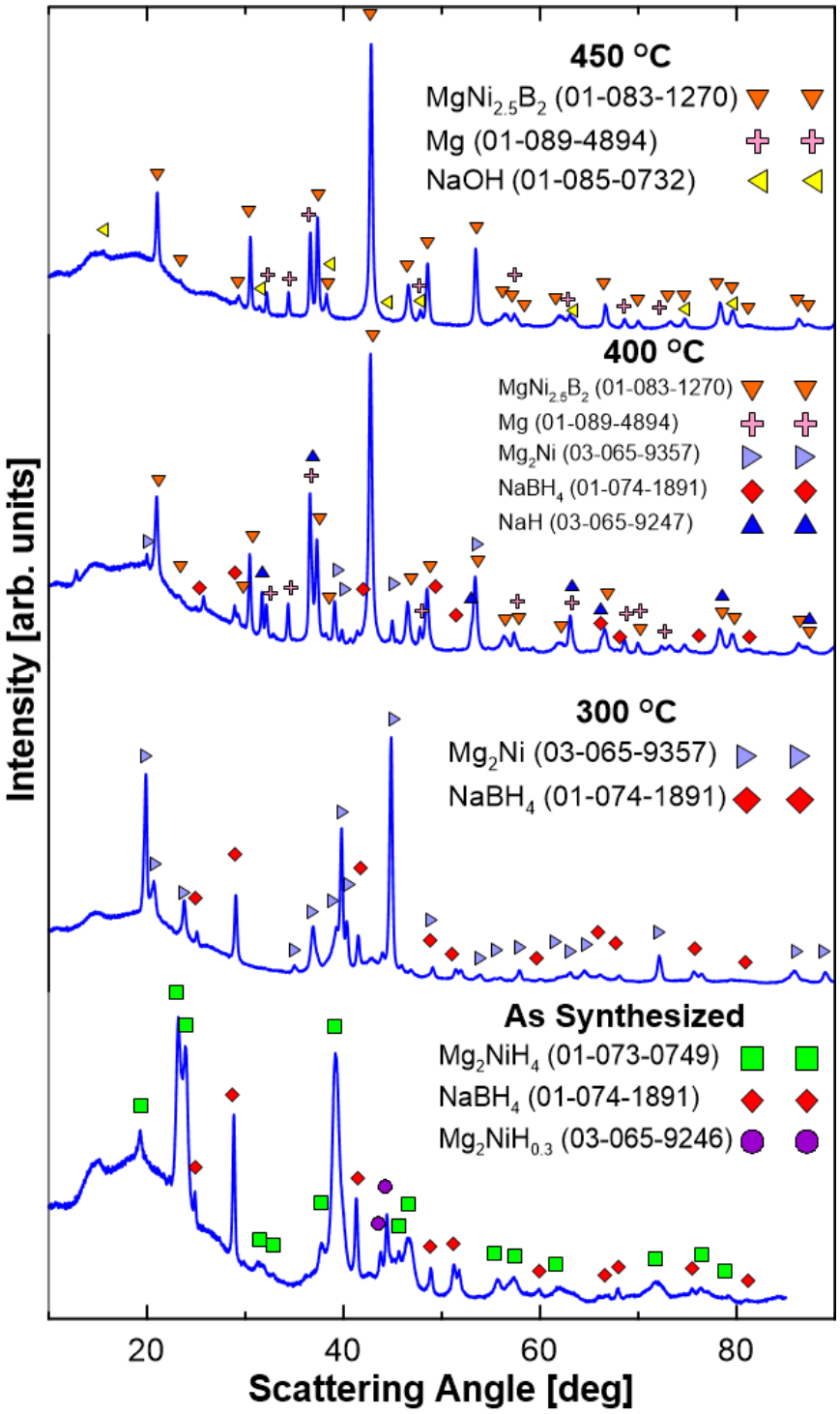

Figure 4.8: XRD plot of $4NaBH_4$ / $5Mg_2NiH_4$ showing the phases at each of the desorption steps for as synthesized, 300, 400 and 450 ºC. Powder diffraction file (PDF) numbers are shown in brackets to the right of the respective compounds (deg in 2θ).

The following reactions are proposed for the decomposition of the composite under 1 bar hydrogen pressure based on the XRD data:

$$4NaBH_4 + 5Mg_2NiH_4 \rightleftharpoons 4NaBH_4 + 5Mg_2Ni + 10H_2 \qquad T \leq 300^{\circ}C \qquad (4.5)$$

$$4NaBH_4 + 5Mg_2Ni \rightleftharpoons 4NaH + 2MgNi_{2.5}B_2 + 8Mg + 6H_2 \qquad T \leq 400^{\circ}C \qquad (4.6)$$

The final step proposed for the decomposition of the composite was observed under vacuum:

$$NaH \rightleftharpoons Na + H \qquad T \leq 425^{\circ}C \qquad (4.7)$$

We noticed the presence of Na compounds (e.g. NaOH, NaO_2 etc) on top of the stainless steel spacer which lies above the sample holder. The sample holder's lid is a porous stainless steel filter (5 micron) which allows for the gas to flow in and out of the sample tube. During decomposition (~450 ºC), some Na diffuses out and deposits on the spacer piece (Na has a melting temperature of about 98 ºC [35]). Figure 4.9 shows a photo of Na compounds deposited on the spacer. The amount of Na seen here is estimated to be about 7 mg (See Appendix B) or about 20% of the total Na available in the composite.

A: Desorption under vacuum

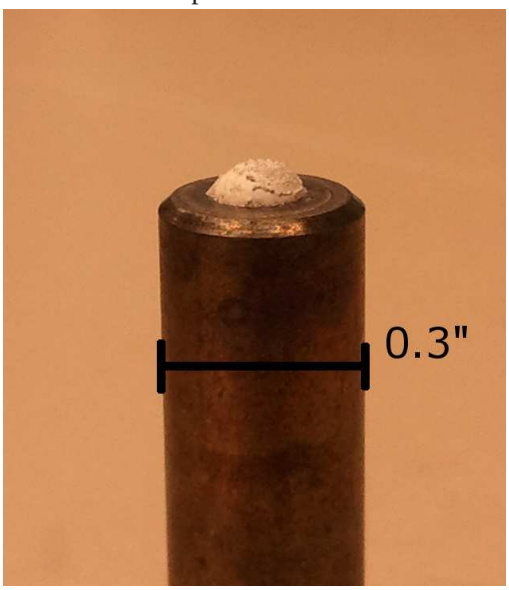

B: Desorption at 1 bar

Figure 4.9: Photo of sample holder spacer with Na compounds after heating the $4NaBH_4$ / $5Mg_2NiH_4$ under vacuum.

When desorption experiments were carried out under 1 bar of hydrogen significantly less Na diffusion occurs. Figure 4.9B shows the formation of Na - based compounds for a desorption made under 1 bar. We estimate the Na loss is about 5% in this case. Figure 4.10 shows the XRD scan of the deposit on the spacer that was obtained after a desorption experiment under vacuum. Several Na containing compounds can be identified. These are NaOH, NaO_2 and Na_2O_2. No sign of other metals present in the composite (Mg, Ni, B) can be seen.

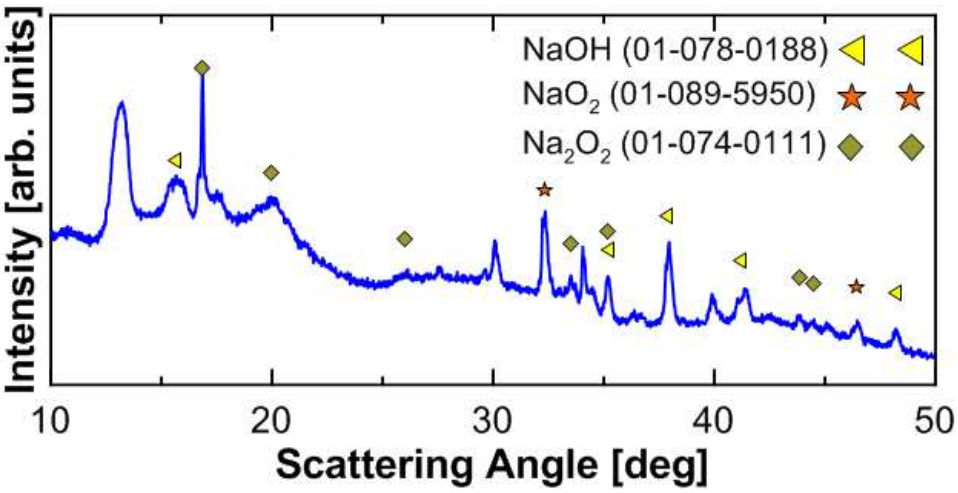

Figure 4.10: XRD scan of the Na compounds formed on the spacer (deg in 2θ).

Mg also appears to diffuse and desposit on the lid. Magnesium, however, does not diffuse through the porous lid onto the spacer. It crystallizes on the underside of the sample holder lid when the composite is heated to 450 ºC under vacuum (see Figure 4.11). This further corroborates reaction 4.6, as excess Mg is formed when the ternary boride $MgNi_{2.5}B_2$ is formed. As with the Na, the amounts of Mg that formed on the lid also varied.

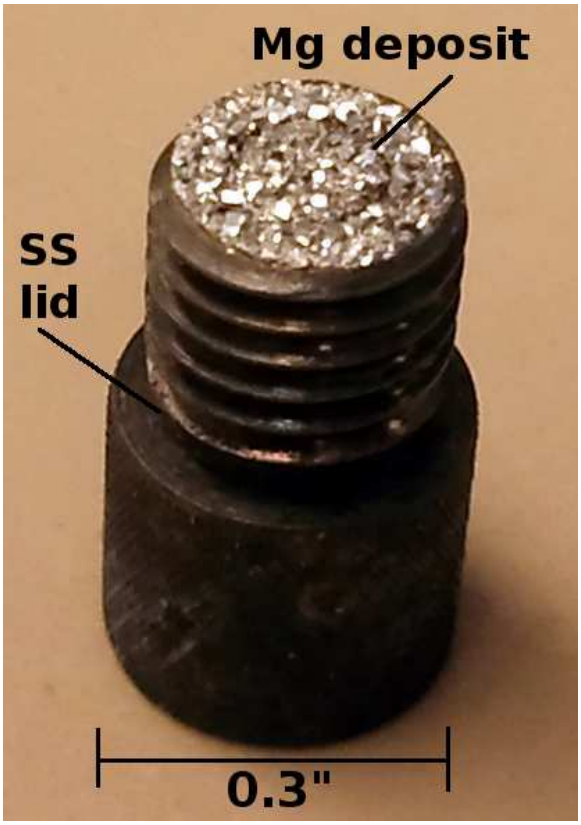

Figure 4.11: Photo of Mg crystallized on underside of sample holder lid

Figure 4.12 shows a diagram of the sample holder, lid and spacer with the location of the Na deposit on the spacer and the Mg deposit on the lid. The diagram shows how the sample holder, lid and spacer are situated in the autoclave. The diffusion of Na through the filter will cause a number of problems for use of the composite in applications of hydrogen storage. The loss of Na and Mg will reduce the capacity of the system. Safety hazards and contamination of components down stream of the hydrogen storage system are possible problems that will have to be overcome.

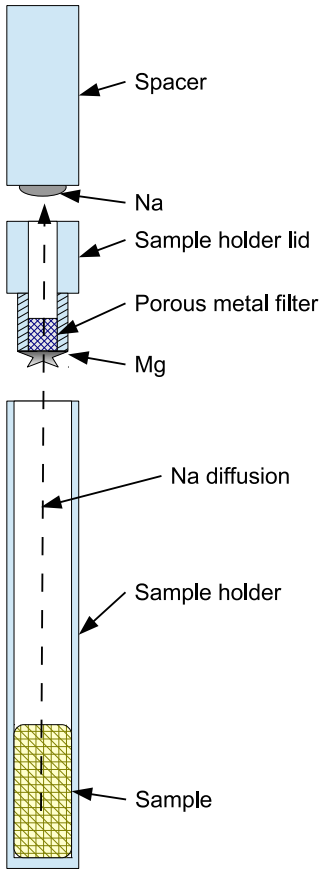

Figure 4.12: Diagram of the sample holder, lid and spacer with the location of the Na deposit on the spacer and the Mg deposit on the lid.

Pinkerton et al. observed foaming of the $LiBH_4$ / MgH_2 system during decomposition [29] due to $LiBH_4$ melting. This led to the composite overflowing the sides of their open sample holder. Garroni et al. have observed NaH contamination outside of their sample holders after absorption (for a $NaBH_4$ / MgH_2 composite), suggesting it may be due to the low melting temperature of Na (~98 ºC), which allows it to escape [35]. The melting point of $NaBH_4$ is ~505 ºC and occurs before hydrogen release [30] indicating that the addition of a destabilizing compound may reduce its melting temperature. Varin et al. observed a slight decrease in the melting point for $NaBH_4$ with increasing MgH_2, however, DSC scans

showed that after about 63 vol.% MgH_2 the peak associated with the melting of $NaBH_4$ disappeared [42]. The $4NaBH_4$ / $5Mg_2NiH_4$ DSC scans also show no peak associated with the melting of $NaBH_4$. However, foaming of the sample has been observed similar to Pinkerton et al.'s experience.

The foaming $4NaBH_4$ / $5Mg_2NiH_4$ composite may completely fill the sample holder enabling Na and Mg to get to the lid. However, as Figure 4.10 shows, only Na seems to diffuse through the stainless steel filter in the lid. As the temperature rises and the reactions proceed, Na and Mg are liberated from the composite and rise to the top of the foam due to their lower density. Na's melting point is ~98 ºC [35], which allows it as a liquid to flow through the stainless steel filter in the lid of the sample holder and onto the spacer. Mg, however, does not pass through the filter and deposits on the inside of the sample holder lid. More Na is seen on the spacer during decomposition under vacuum because NaH decomposes under vacuum in the composite. The melting point of NaH is 800 ºC so it won't melt and pass through.

Figure 4.13 shows X-ray diffraction patterns of the $4NaBH_4$ / $5Mg_2NiH_4$ composite after absorption steps. Each absorption step was preceded by a desorption step. The formation of $MgNi_2$, which does not hydrogenate [39] is observed, and partially accounts for the loss of capacity discussed in section 4.7. The formation of $MgNi_2$ may be the result of the break down of $MgNi_{2.5}B_2$ because the Ni rich ternary boride is closer in stoichiometry to $MgNi_2$ than Mg_2Ni. When the ternary boride $MgNi_{2.5}B_2$ decomposes and releases B it must either acquire more Mg, or lose excess Ni before its stoichiometry is correct.

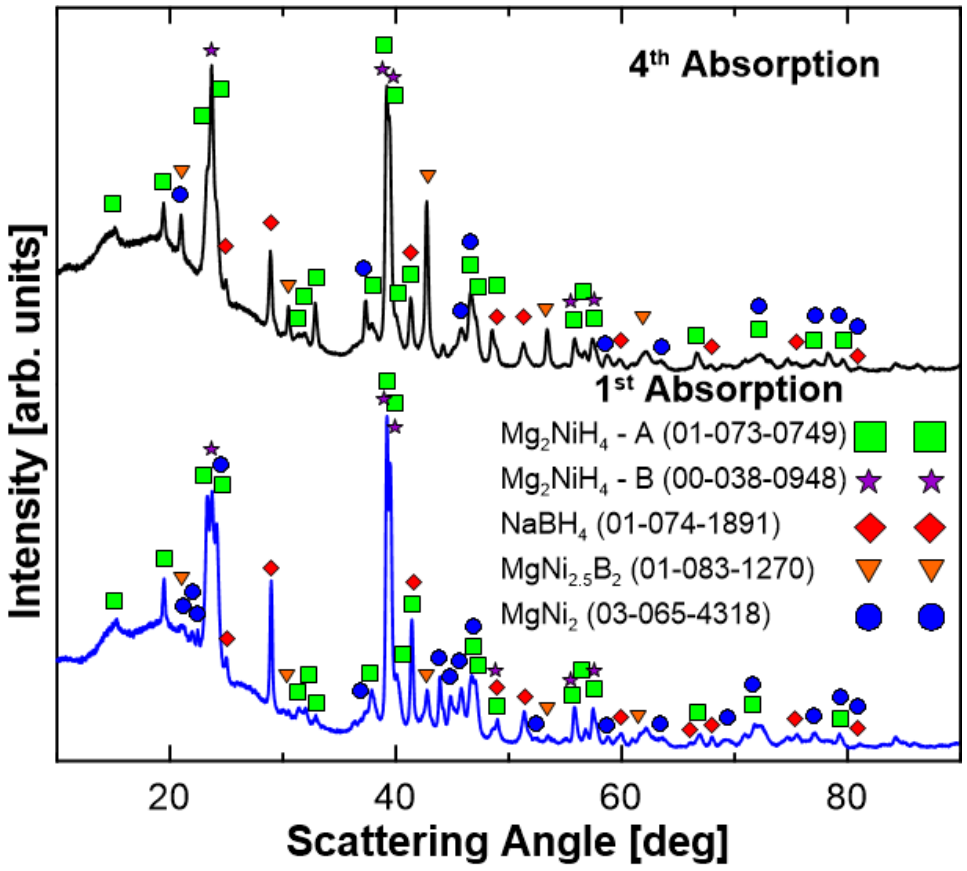

Figure 4.13: XRD analysis of $4NaBH_4$ / $5Mg_2NiH_4$ composite after the first and fourth absorptions. The hydride mixture was hydrogenated at 57 bar and 350 ºC and dehydrogenated at about 5 bar and 450 ºC (see TPD cycling in section 4.7) (deg in 2θ).

Analyzing the X-ray diffractograms of the composite after a rehydrogenation reaction is challenging because some materials are still present in their dehydrogenated form. This could signify that either a longer hydrogenation time is required, or full rehydrogenation is not possible. If full rehydrogenation is not possible, then reaction 4.8 shows a possible reaction pathway with decomposition chemicals still present during absorption. However, the stoichiometry of the chemicals is unknown and depends on the amount of rehydrogenation

possible and the amount of $MgNi_{2.5}B_2$ converted to $MgNi_2$ and Mg_2Ni.

$$Na + MgNi_{2.5}B_2 + Mg + H_2 \rightleftharpoons$$

$$MgNi_2 + Mg_2NiH_4 + NaBH_4 + MgNi_{2.5}B_2 + Mg \tag{4.8}$$

The products of absorption in reaction 4.8 show the unreacted species $MgNi_{2.5}B_2$ and $MgNi_2$ which suggests some irreversibility. The loss of Na is likely the reason $MgNi_{2.5}B_2$ does not decompose. The excess Mg is likely because $MgNi_{2.5}B_2$ and $MgNi_2$ are Mg poor compounds, leaving an excess of Mg in the reactor which then seems to collect on the underside of the lid. The excess Mg is not seen in the XRD analysis shown in Figure 4.13 because it collected on the lid and was not part of the sample tested. The Mg that collects on the underside of the lid does not contribute to the capacity of the system by forming MgH_2 during absorption. This could be due to the large size of the Mg crystals which are kinetically limiting due to large hydrogen diffusion paths and low surface area for hydrogen dissociation to occur.

4.4 Thermodynamic Studies (Pressure-Composition-Temperature)

The reaction enthalpy of the $4NaBH_4$ / $5Mg_2NiH_4$ composite depends on the chemical reaction pathway. Table 4.4 summarizes the enthalpies of a number of possible reactions involving $LiBH_4$, $NaBH_4$, Mg_2NiH_4 and MgH_2. Table 4.4 also presents the theoretical and the observed hydrogen desorption temperatures. The desorption temperature here refers to the temperature of the sample when hydrogen pressure is 1 bar. The theoretical desorption temperatures are calculated using the van't Hoff relation as described in equation 2.7 of

Chapter 2.2 and using the ΔH_{des} tabulated in table 4.4. The entropy of desorption, ΔS, is taken to be constant at 130 J mol^{-1} K^{-1}. The observed temperatures listed are typically generated from a TPD measurement performed under 1 bar hydrogen.

The theoretical T_{des} correspond to the temperature of the sample when $P_{H_2} \approx 1$ bar. This temperature is obtained from the van't Hoff equation and using the tabulated ΔH_{des} and ΔS_{des} of 130 J mol^{-1} K^{-1}. Heating to T_{des}, however, does not usually lead to a pressure of 1 bar, and higher temperatures are required. This is because most of these reactions are kinetically limited. The last column in table 4.4 shows the observed T_{des}, and reflects this fact.

The influence of pathways on the desorption enthalpy can be clearly seen for the $NaBH_4$ / Mg_2NiH_4 system, where a range of enthalpies that span from 34 to 61 kJ $mol_{H_2}^{-1}$ could exist. For reaction 12 in table 4.4, the equilibrium temperature corresponding to 1 bar of hydrogen is -12 ºC. This means that 2.3 wt% hydrogen should be spontaneously released at room temperature and atmospheric pressure. This, however, does not happen because the reaction is slow and heating is required for any desorption to take place.

There are a number of possible desorption routes for the Mg_2NiH_4 / $NaBH_4$ system and table 4.4 lists several of them (9 - 12). These are some of the expected routes based on proposed reaction pathways for similar systems such as $LiBH_4$ / Mg_2NiH_4 and $NaBH_4$ / MgH_2. The complete decomposition of $LiBH_4$ (e.g., 1 in table 4.4) has an enthalpy of 96 kJ $mol_{H_2}^{-1}$. The decomposition of $LiBH_4$ to LiH (2), however, has an enthalpy of about 68 kJ $mol_{H_2}^{-1}$, which is much lower than that required for complete decomposition. Vajo et al. reported that the addition of MgH_2 to $LiBH_4$ (3) reduces the enthalpy of decomposition to 46 kJ $mol_{H_2}^{-1}$, and has a theoretical desorption temperature of about 225 ºC [4]. They also reported that the addition of Mg_2NiH_4 to $LiBH_4$ (4) further reduced the enthalpy to 15 kJ $mol_{H_2}^{-1}$. The same trend was reported for $NaBH_4$ by Mao et al. for the addition of MgH_2 (7), which reduced the enthalpy by about 30 kJ $mol_{H_2}^{-1}$.

The theoretical temperature of desorption for many of the entries in table 4.4 were calculated using equation 2.7 with an entropy of 130 J mol^{-1} K^{-1} as it is constant across many metal hydride systems. However, Vajo et al. reported an entropy of 62.2 $\pm$ 3 J mol^{-1} K^{-1} H_2 for the $LiBH_4$ / Mg_2NiH_4 system and hypothesize that it may be different because of the two complex hydride anions in the hydrogenated state [4]. The $NaBH_4$ / Mg_2NiH_4 system was found in the work completed for this thesis to have an entropy that is close to 130 J mol^{-1} K^{-1}. Theoretical temperatures of desorption that have a reference listed beside them have been obtained from the literature. Enthalpies shown for reactions 9- 12 were calculated using data from NIST-JANAF Thermochemical Tables [26] and Vajo et al.'s data for Mg_2NiH_4 [4]. The experimental values for reactions are discussed further in this section.

Table 4.4: Thermodynamic properties of various hydrides and mixtures of hydrides for 1 bar hydrogen back pressure

#	**Reaction**	**Wt% H**	ΔH_{des} **[kJ mol$^{-1}_{H_2}$]**	**Theoretical T_{des} [°C]**	**Observed T_{des} [°C]**
1	$LiBH_4 \rightarrow Li+B+2H_2$	18.5	96 [26]	465	-
2	$LiBH_4 \rightarrow LiH+B+{}^3/_2H_2$	13.9	67-69 [5, 9]	410 [6]	400-500 [2]
3	$2LiBH_4+MgH_2 \rightarrow 2LiH+MgB_2+4H_2$	11.5	46 [4]	168 - 225 [5, 6]	270 [5]
4	$5Mg_2NiH_4+4LiBH_4 \rightarrow 2MgNi_{2.5}B_2+4LiH+8MgH_2+8H_2$	5	15 [4]	-25 [4]	250 [4]
5	$NaBH_4 \rightarrow Na+B+2H_2$	10.8	96 - 114 [43, 26]	465 - 604	577 [31, 2]
6	$NaBH_4 \rightarrow NaH+B+{}^3/_2H_2$	8	88 - 90 [32]	667 [32]	-
7	$2NaBH_4+MgH_2 \rightarrow 2Na+MgB_2+5H_2$	9.9	62-100.58 [35, 34, 31]	288 - 500	450-490 [35, 31, 34]
8	$2NaBH_4+MgH_2 \rightarrow 2NaH+MgB_2+4H_2$	7.9	64 [26]	219	-
9	$5Mg_2NiH_4+4NaBH_4 \rightarrow 2MgNi_{2.5}B_2+4Na+8Mg+18H_2$	5.1	61	196	450
11	$5Mg_2NiH_4+4NaBH_4 \rightarrow 2MgNi_{2.5}B_2+4NaH+8Mg+16H_2$	4.5	55	150	360
10	$5Mg_2NiH_4+4NaBH_4 \rightarrow 2MgNi_{2.5}B_2+4Na+8MgH_2+10H_2$	2.8	49	104	-
12	$5Mg_2NiH_4+4NaBH_4 \rightarrow 2MgNi_{2.5}B_2+4NaH+8MgH_2+8H_2$	2.3	34	-12	-
13	$MgH_2 \rightarrow Mg+H_2$	7.6	75 [2]	304	310
14	$Mg_2NiH_4 \rightarrow Mg_2Ni+2H_2$	3.4	65.8	233	280 [20]

Figures 4.15 and 4.14 show the absorption and desorption PCTs, respectively for the $4NaBH_4$ / $5Mg_2NiH_4$ system. The desorption equilibrium PCT measurements exhibit a number of pressure plateaus: A, B, and C, and correspond to the decomposition of Mg_2NiH_4, $NaBH_4$, and NaH, respectively (discussed further in section 4.3). The desorp-

tion isotherm at 475 ºC appears to be reabsorbing hydrogen as the pressure is decreased. The reason for this is unclear, but may be due to instrumental error, possibly a change in temperature of the reservoir volume.

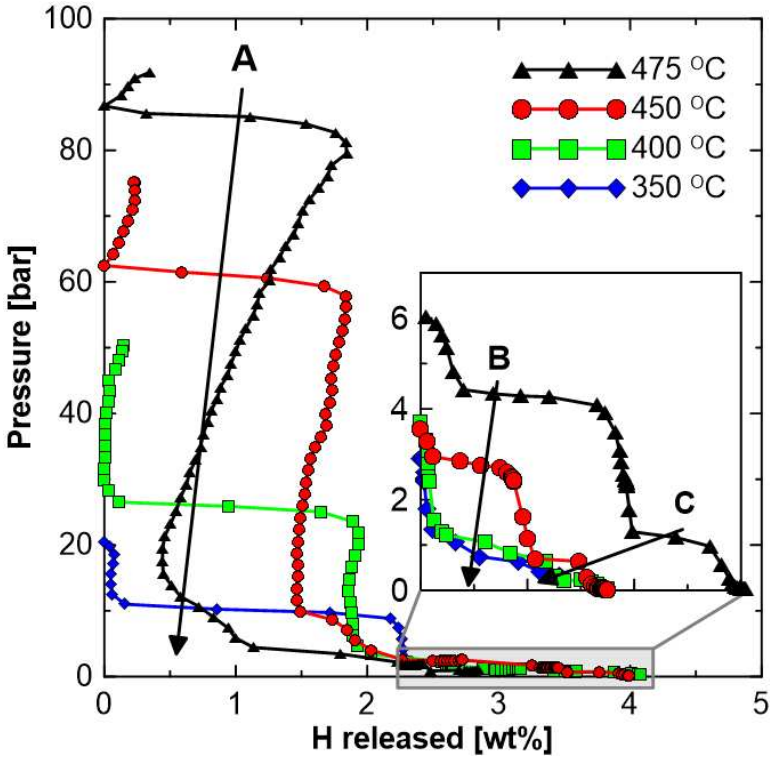

Figure 4.14: Desorption PCTs for $4NaBH_4$ / $5Mg_2NiH_4$ at 350, 400, 450 and 475 ºC. An upper plateau (A) is shown for Mg_2NiH_4 decomposition and low pressure plateaus for $NaBH_4$ (B and C).

Table 4.5 shows the equilibrium pressures and the standard deviation for plateaus A-C in Figure 4.14.

Table 4.5: Desorption Equilibrium Pressures for the $4NaBH_4$ / $5Mg_2NiH_4$ system

Temperature [ºC]	Pressure [bar]	Uncertainty [bar]
Plateau A		
350	9.96	0.91
400	25.3	1.3
450	60.4	1.8
475	85.7	2.4
Plateau B		
350	0.378	0.053
400	1.01	0.27
450	2.81	0.11
475	4.28	0.13
Plateau C		
400	0.213	0.01
450	0.672	0.041
475	1.15	0.1

Figure 4.15 shows the absorption isotherms for the $4NaBH_4$ / $5Mg_2NiH_4$ system at 400, 450 and 475 ºC. The plateaus for absorption are not as clear as for desorption, although an upper plateau for the absorption of $Mg_2Ni + H_2 \rightleftharpoons Mg_2NiH_4$ (I) and a lower plateau related to $NaBH_4$ absorption (II) are observed. The isotherm at 450 ºC is difficult to interpret because of the plateaus shown by the ♢ and △ symbols, either of which could represent the Mg_2NiH_4 absorption plateau. For this thesis the upper most plateau (♢) was taken as the Mg_2NiH_4 absorption plateau for two reasons: 1) the plateaus at I for 400 and 475 ºC show large amounts of hydrogen absorbed with few data points, whereas the △ plateau shows a much more sloped and slow absorption, and 2) The van't Hoff analysis has a better fit statistic for the ♢ plateau of $R^2 = 0.9976$, compared to 0.984 for the △ plateau.

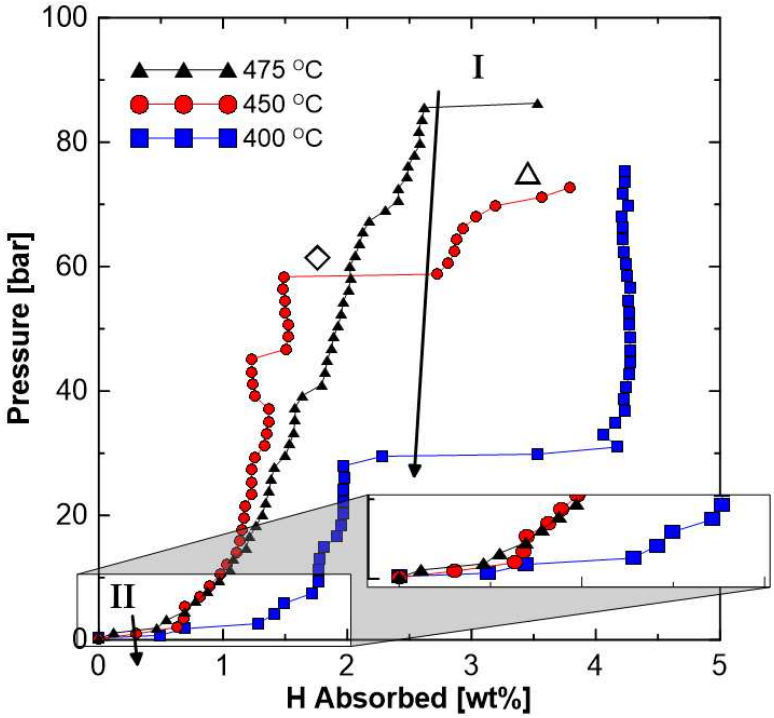

Figure 4.15: Absorption PCT measurements for $4NaBH_4$ / $5Mg_2NiH_4$ at 400, 450 and 475 ºC. An upper plateau related to Mg_2NiH_4 absorption, and a lower plateau related to $NaBH_4$ absorption can be observed

To clarify the lower plateau of the absorption isotherms a log-log plot of Figure 4.15 is shown in Figure 4.16. The lower plateau pressure (II) shows little distinction between the three temperatures tested indicating that further testing at the lower pressure plateau is required. Smaller aliquots (hydrogen doses) and longer equilibration times may help differentiate the lower plateaus.

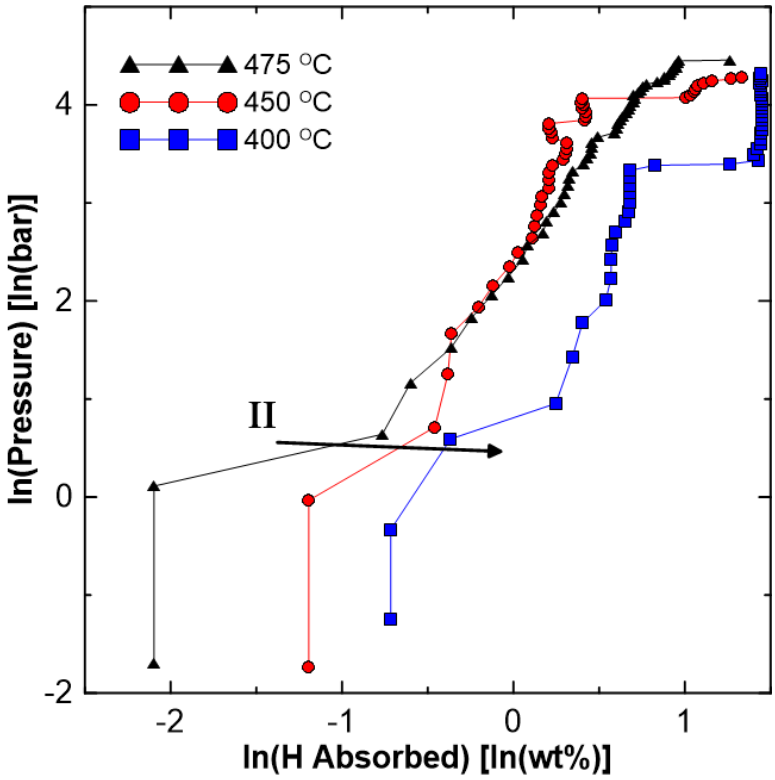

Figure 4.16: The natural logarithm of the wt % H absorbed and the pressure for the absorption PCT measurements of $4NaBH_4$ / $5Mg_2NiH_4$ at 400, 450 and 475 ºC.

Figure 4.17 shows the van't Hoff analysis of the desorption PCT curves. For the decomposition of Mg_2NiH_4 (plateau A) we obtain $\Delta H = 67 \pm 4$ kJ $mol_{H_2}^{-1}$. Selvam et al. have reported the value 65.8 kJ $mol_{H_2}^{-1}$ [40] for the decomposition enthalpy of Mg_2NiH_4 alone. For the plateau associated with the decomposition of $NaBH_4$ to NaH + B (plateau B), $\Delta H = 76 \pm 5$ kJ $mol_{H_2}^{-1}$, which is lower than, but comparable to the value of 88.2 kJ $mol_{H_2}^{-1}$ reported by Garroni et al. [32] for the decomposition of $NaBH_4$ to NaH. For the plateau associated with the decomposition of NaH to Na, $\Delta H = 95 \pm 7$ kJ $mol_{H_2}^{-1}$, and according to Banus et al. [43] it has a decomposition enthalpy of 114 kJ $mol_{H_2}^{-1}$. The larger error for the higher enthalpies is a result of the sensitivity of the van't Hoff plot to variations in pressure at lower pressures. The plateaus associated with $NaBH_4$ decomposition show a reduction

of the decomposition enthalpy indicating thermodynamic destabilization was successfully achieved in this composite system.

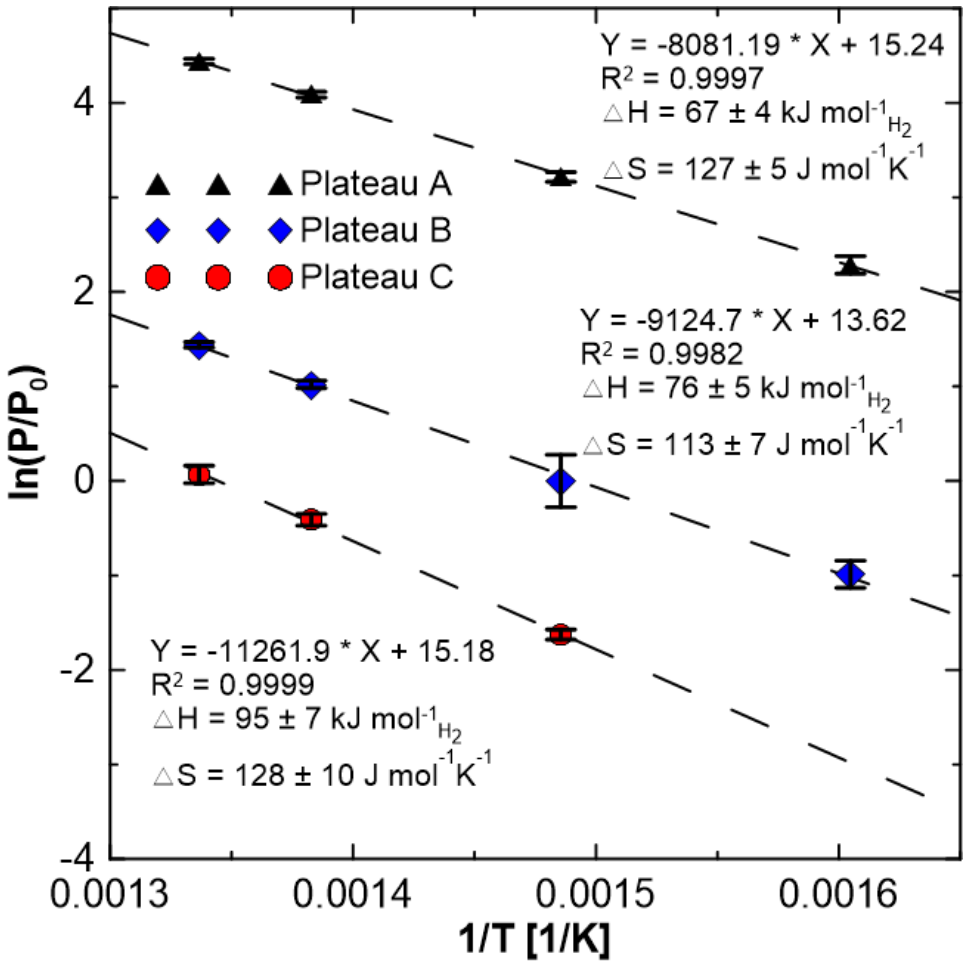

Figure 4.17: Van't Hoff analysis for the desorption PCT curves, the upper pressure plateau corresponding to the decomposition of Mg_2NiH_4 has the lowest enthalpy, while the decomposition of NaH has the highest enthalpy.

Desorption of hydrogen from Mg_2NiH_4, under 1 bar hydrogen back pressure initiates at 280 ºC according to Hirscher et al. [20]. In our experiment with Mg_2NiH_4 prepared here, desorption is observed at 300 ºC. The higher desorption temperature for the as synthesized Mg_2NiH_4 may be due to kinetic limitations rather than a change in thermodynamics. In the

$4NaBH_4$ / $5Mg_2NiH_4$ composite however, Mg_2NiH_4 decomposition under 1 bar hydrogen, commenced at 275 ºC. This shows a change in onset of about 25 ºC with respect to the same Mg_2NiH_4 tested under similar conditions indicating a possible kinetic effect.

The decomposition of $NaBH_4$ in the $4NaBH_4$ / $5Mg_2NiH_4$ composite begins at about 360 ºC. This is significantly lower than 577 ºC for $NaBH_4$ alone as reported by Varin et. al. [2]. It is also significantly lower than the $2NaBH_4$ / MgH_2 system which occurs at about 450 ºC [34]. Based on the experiments performed, it is apparent that the first step of the reaction, i.e., decomposition of Mg_2NiH_4 does not show any thermodynamic destabilization, whereas the next step, i.e., decomposition of $NaBH_4$, shows significantly more favourable thermodynamics. This is what we expected. The third plateau (C) associated with the decomposition of NaH to Na and H occurred at an observed temperature of about 420 ºC, and only occurred at lower than 1 atm pressures. For equilibrium pressures above atmospheric pressure, temperatures above 450 ºC are required (see plateau C in table 4.5).

Figure 4.18 shows the van't Hoff analysis of the absorption PCT curve for the hydrogenation of Mg_2NiH_4 (plateau I). The plateaus associated with the formation of $NaBH_4$ could not be resolved from the PCT data collected as mentioned earlier. However, the enthalpy of formation for the plateau associated with the hydrogenation of Mg_2NiH_4 is 59 ± 4 kJ $mol_{H_2}^{-1}$, which is similar to the enthalpy obtained in section 4.2 for Mg_2NiH_4 alone (60 ± 3 kJ $mol_{H_2}^{-1}$). This indicates that Mg_2NiH_4 is likely formed from Mg_2Ni, and not from an intermediate compound containing boron or other stoichiometries of Mg and Ni.

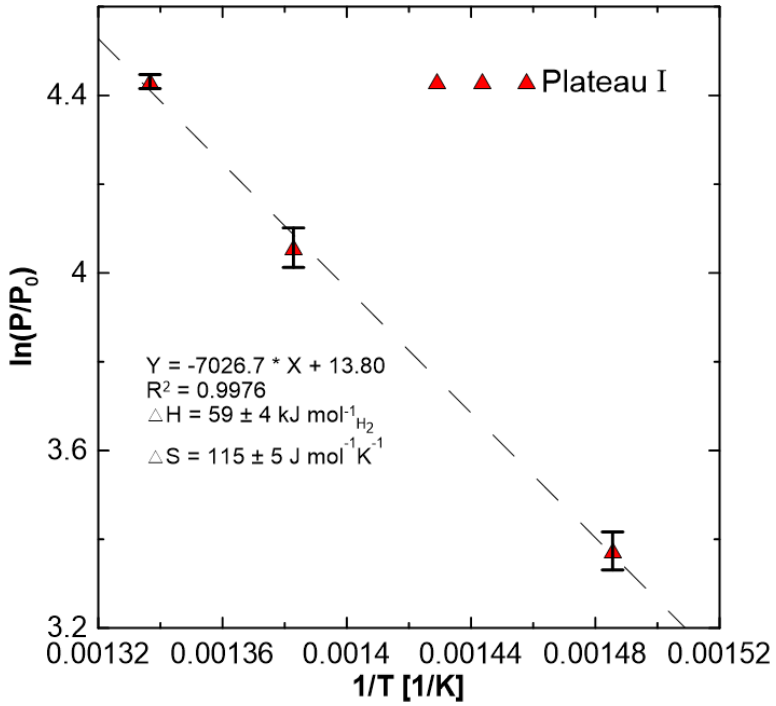

Figure 4.18: Van't Hoff analysis for absorption plateau I.

The equilibrium temperatures corresponding to 1 bar H_2 for the enthalpies obtained by PCT measurements for plateaus A, B and C are 242 ± 17, 311 ± 39, and 450 ± 50 ºC, respectively. Table 4.6 shows a summary of the enthalpies, entropies and temperatures associated with the $4NaBH_4$ / $5Mg_2NiH_4$ system. The observed temperature of desorption for plateau C was performed under vacuum.

Table 4.6: Comparison of desorption enthalpies and entropies, and temperatures obtained for $4NaBH_4$ / $5Mg_2NiH_4$

Plateau	ΔH_{des} **[kJ mol$^{-1}_{H_2}$]**	ΔS_{des} **[J mol^{-1}K^{-1}]**	**Theoretical T_{des} (1 bar) [ºC]**	**Observed T_{des} [ºC]**
A	67 ± 4	127 ± 5	242 ± 17	275
B	76 ± 5	113 ± 7	311 ± 39	360
C	94 ± 7	128 ± 10	450 ± 50	420 (vacuum)

As mentioned earlier, Vajo et al. reported a value of 62.2 $\pm$ 3 J mol^{-1} K^{-1} for the change in entropy of the $4LiBH_4$ / $5Mg_2NiH_4$ system after desorption. They attributed it to the additional entropy associated with having two complex anions $[BH_4]^-$ and $[NiH_4]^{4-}$. However, the entropy of the $4NaBH_4$ / $5Mg_2NiH_4$ system, with the same complex anions, was close to the 130 J mol^{-1} K^{-1} that is typically reported for metal hydrides [9]. This may indicate that the reactions taking place to liberate hydrogen are quite different.

4.5 Hydrogen Back Pressure Experiments

In some composites such as $LiBH_4$ / MgH_2 a hydrogen back pressure of greater than 1 bar is required during the desorption in order for the intermediate phase (e.g., MgB_2) to form [6, 29]. Three pressures, vacuum, 1 bar, and 5 bar were used to investigate the effects of back pressure on the formation of $MgNi_{2.5}B_2$.

According to Pinkerton et al. [29] hydrogen back pressure is required in the $LiBH_4$ / MgH_2 system to achieve reversibility. They report that the dehydrogenation of $LiBH_4$ to LiH and amorphous B is kinetically favored over the reaction of Mg to form MgB_2 unless the hydrogen pressure is above about 3 bar. In other words, the hydrogen pressure kinetically suppresses $LiBH_4$ decomposition enough to allow the formation of MgB_2 to occur before that of amorphous B. The $4LiBH_4$ / $5Mg_2NiH_4$ system Vajo et. al. studied also required a hydrogen pressure above 3 bar to form $MgNi_{2.5}B_2$ [4]. This indicates that the formation of the ternary boride is kinetically limited in relation to the decomposition of $LiBH_4$ as well.

Figure 4.19 shows the XRD patterns for the three different hydrogen back pressures after heating to 450 ºC. The pressures of vacuum, 1 bar, and 5 bar hydrogen all resulted in the formation of the ternary boride phase $MgNi_{2.5}B_2$. This is because pure $NaBH_4$ does not decompose before 500 ºC, and therefore will not decompose to form amorphous boron before it can react with the Mg_2Ni and form $MgNi_{2.5}B_2$.

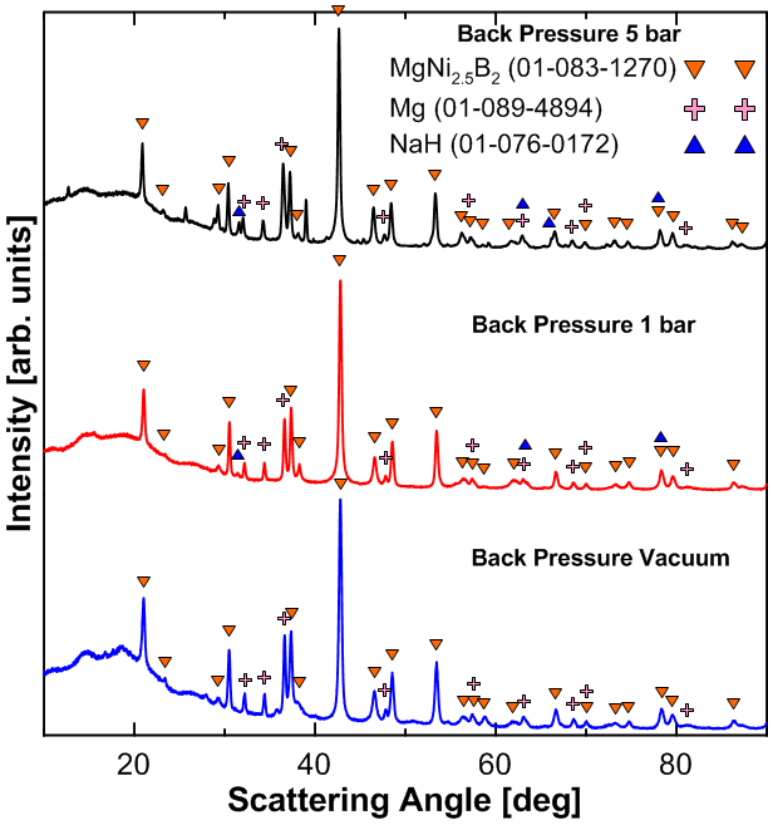

Figure 4.19: XRD scans of $4NaBH_4$ / $5Mg_2NiH_4$ after heating to 450 ºC under hydrogen pressures of vacuum, 1 bar and 5 bar (deg in 2θ).

During desorption the pressure in the sample holder will increase as the composite is heated and releases hydrogen. The increase in the pressure depends on the size of the reservoir volume that is chosen, a larger increase in pressure is observed for a smaller reservoir size. Figure 4.20B shows the change in the pressure of the sample holder for three different reservoir sizes. The smallest volume (11.7 ml) approaches almost 6 bar during hydrogen desorption, while the largest volume (1056.3 ml) only reaches about 1.2 bar. Figure 4.20A shows the corresponding hydrogen release for each of the reservoir volumes. The 167.7 and 1056.3 ml reservoirs show more hydrogen release than the 11.7 ml volume. The lower hydrogen release is due to the equilibrium pressure of desorption for $NaBH_4$ in

the composite.

The equilibrium pressure of desorption for $NaBH_4$ is quite low and is about 1 bar at 400 ºC and 2.8 bar at 450 ºC. Thus it will not decompose if the hydrogen back pressure is higher than these equilibrium desorption pressures. Neither the 1056.3 or the 167.7 ml reservoirs at 450 ºC are over 2.8 bar, hence the decomposition of $NaBH_4$ can proceed, as seen by the rise in pressure after the plateaus marked I in Figure 4.20A. However, the 11.7 ml reservoir at 350 ºC is at almost 4.5 bar from the decomposition of Mg_2NiH_4 (which has an equilibrium desorption pressure of about 60 bar). This is above the equilibrium desorption pressure of 2.8 bar, and therefore the decomposition of $NaBH_4$ cannot proceed until the temperature in the reactor rises to a point where the equilibrium desorption pressure is 4.5 bar. The onset of the pressure rise after plateau I is shifted to a higher temperature so that the equilibrium pressure of desorption is above the pressure in the sample holder.

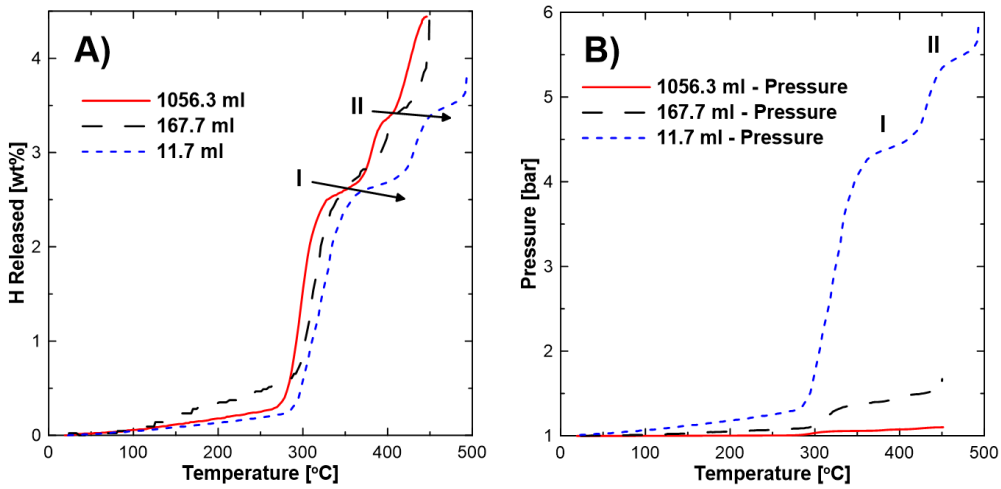

Figure 4.20: Impact of hydrogen back pressure on the plateaus observed during TPD experiments. Hydrogen release is shown in A, and pressure is shown in B.

Figure 4.21 shows the TPD profile of the $4NaBH_4$ / $5Mg_2NiH_4$ composite for three different hydrogen back pressures: vacuum, 1 bar and 5 bar in a constant volume reservoir (1056.3 ml). The different steps in decomposition that were determined in section 4.3 are

labeled: section a shows the decomposition of Mg_2NiH_4, section b shows the decomposition of $NaBH_4$ to NaH, and section c shows the decomposition of NaH into Na.

The effect on the amount of hydrogen released from the composite due to hydrogen back pressure is similar to that observed in Figure 4.20A. The desorption under 5 bar back pressure is limited to about 3.5 wt% H for desorption to 450 ºC, which is the same as that observed for desorption into the 11.7 ml reservoir (which runs to 500 ºC). The desorption under 1 bar and the larger volumes are also the same. However, there are two major differences when the composite is decomposed under vacuum: 1) - a third decomposition step is observed at c, related to the decomposition of NaH, and 2) - during the step labeled b in Figure 4.21, there is no plateau.

The third decomposition step, labeled c, is observed because the pressure in the sample holder is below the equilibrium pressure of desorption for NaH decomposition in the composite, which is about 0.67 bar at 450 ºC. This is a problem for any hydrogen storage system that will run under atmospheric (1 bar) operating conditions if the maximum capacity of the composite is required, as the temperature will have to be increased to raise the equilibrium pressure. For the decomposition of NaH a temperature of 475 ºC is required for an equilibrium desorption pressure of about 1.15 bar.

The extra plateau observed during the heating of $NaBH_4$ in step b under 1 and 5 bar hydrogen back pressure is explained by the equilibrium pressure of desorption. During desorption, when the pressure in the sample holder reaches that of the equilibrium pressure of desorption, the result is a plateau in the TPD measurements. The pressure and the temperature at the end of the plateau corresponds very well with the PCT equilibrium measurements made (section 4.4).

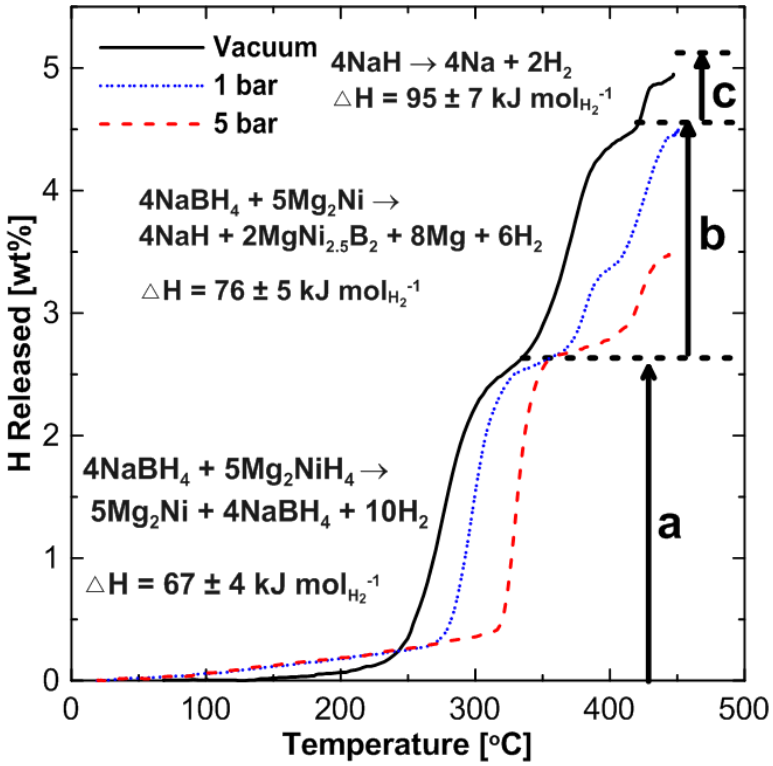

Figure 4.21: TPD for 3 different pressures, vacuum, 1 bar and 5 bar. The horizontal lines represent the theoretical weight percent obtained from the decomposition of the Mg_2NiH_4, $NaBH_4$ and NaH components of $4NaBH_4$ / $5Mg_2NiH_4$. Enthalpies are results of the PCT measurements discussed in section 4.4.

Figure 4.22 shows a combined TGA / DSC analysis of the $4NaBH_4$ / $5Mg_2NiH_4$ composite. The measurements were performed under flowing Argon. Similar to TPDs under vacuum, two dominant processes, namely decomposition of Mg_2NiH_4 and that of $NaBH_4$ occur. Because no hydrogen back pressure is present, steps, as observed in TPD profiles are not observed here. These experiments independently support our explanation that steps at ~400 ºC (step b of Figure 4.21), observed in TPDs under pressure, are a consequence of back pressure and do not signify reaction steps.

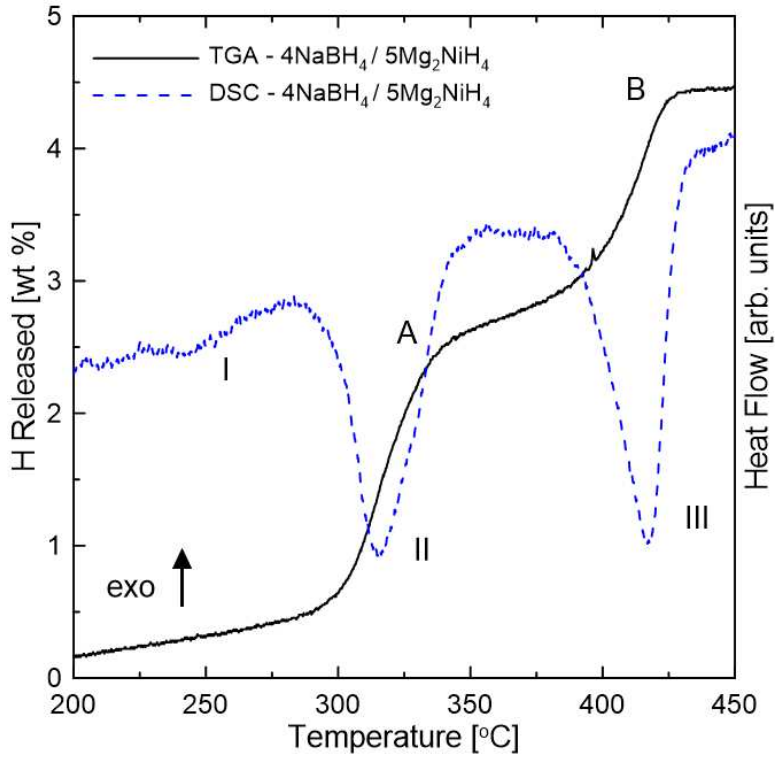

Figure 4.22: Combined TGA and DSC analysis under Argon flow for $4NaBH_4$ / $5Mg_2NiH_4$.

Table 4.7 shows the pressures and temperatures associated with hydrogen desorption at the end of plateau II in Figure 4.20. The pressures and temperatures observed were used to construct a van't Hoff plot.

Table 4.7: Isothermal plateau temperatures and pressures from TPD measurements.

Volume	**Pressure [bar]**	**Temperature [°C]**
1056.3 ml	1.1	410
167.7 ml	1.5	425
11.7 ml	5.5	500

The pressures and temperatures listed in table 4.7 are a consequence of the pressure build up in the sample holder reaching that of the equilibrium desorption pressure for the composite hydride. Therefore, each pressure and temperature point should lie on the PCT

isotherm curve observed in plateau B of Figure 4.17. Figure 4.23 shows the van't Hoff plot with the data from plateau II of the TPDs and the data from the PCT isotherms for plateau B compared. The results are very similar indicating that plateau II observed in TPD measurements are a consequence of the system reaching the equilibrium pressure. These plateaus are not related to formation of stable compounds.

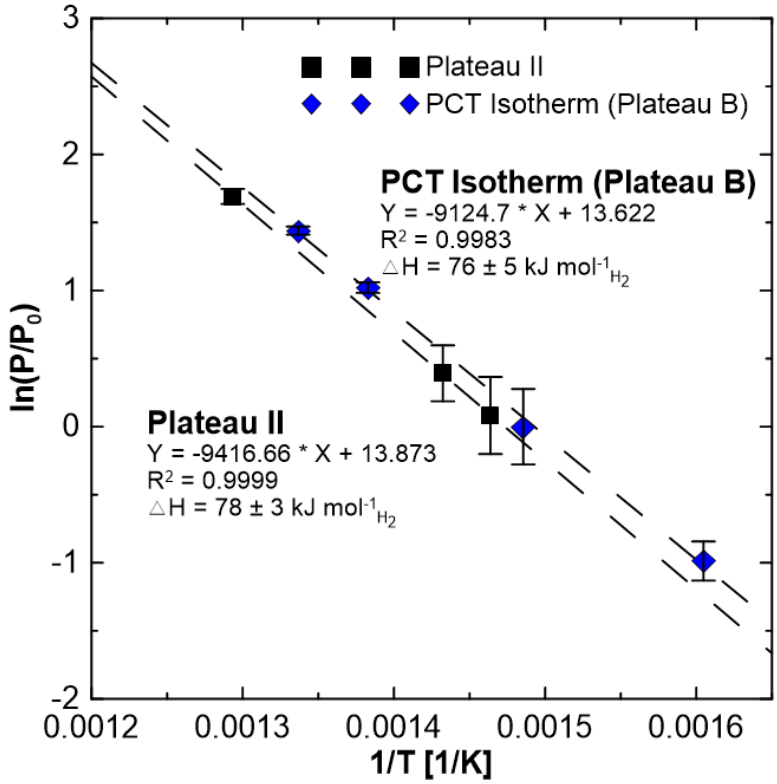

Figure 4.23: Van't Hoff plot with the data from plateau II of the TPDs and the data from the PCT isotherms for plateau B compared. The data are almost collinear indicating that plateau II is not related to a new reaction step.

4.6 Ball Milling Experiments of $NaBH_4$ / Mg_2NiH_4 Mixtures

Ball milling has been shown to have a strong impact on the hydrogen sorption and desorption properties in many hydride systems such as MgH_2 [2]. In general the kinetics of

hydrogen absorption / desorption is improved. Varin et al. have attributed the kinetic enhancement of ball milled MgH_2 to: i) grain size reduction, ii) particle size reduction, iii) formation of new phases, and iv) break up of oxide shell surrounding the particle [2]. Grain size reduction improves hydrogen diffusion into and out of the metal hydride by moving easier through an increased number of grain boundaries. Decreased particle size increases the surface area of the hydride and reduces the diffusion distances required to achieve hydrogen saturation in the hydride phase, and the formation of new phases with lower activation energy can improve kinetics, e.g., the γ - MgH_2 phase that appears after ball milling commercial β - MgH_2. The breakup of the oxide shell allows hydrogen dissociation to occur easier as it is much faster on a metal surface, and it also mitigates the slow diffusion through the oxide shell before entering the metal part of the particle, improving the kinetics.

Figure 4.24 shows the impact of ball milling on the hydrogen desorption temperature of the ball milled Mg_2NiH_4 / $NaBH_4$ mixture. Ball milling for up to 120 minutes has apparently little impact on the onset temperature of desorption. The Mg_2NiH_4 was also prepared fresh and had little exposure to oxygen or moisture, thus oxide phases are negligible. Therefore it may not be surprising that ball milling the mixture Mg_2NiH_4 / $NaBH_4$ up to 120 minutes does not show any significant impact on the hydrogen desorption properties. $NaBH_4$ has shown little change in structure and decomposition behavior from ball milling according to Varin et al. [44, 2]. Thus overall changes are insignificant when both powders are ball milled together for up to 120 minutes.

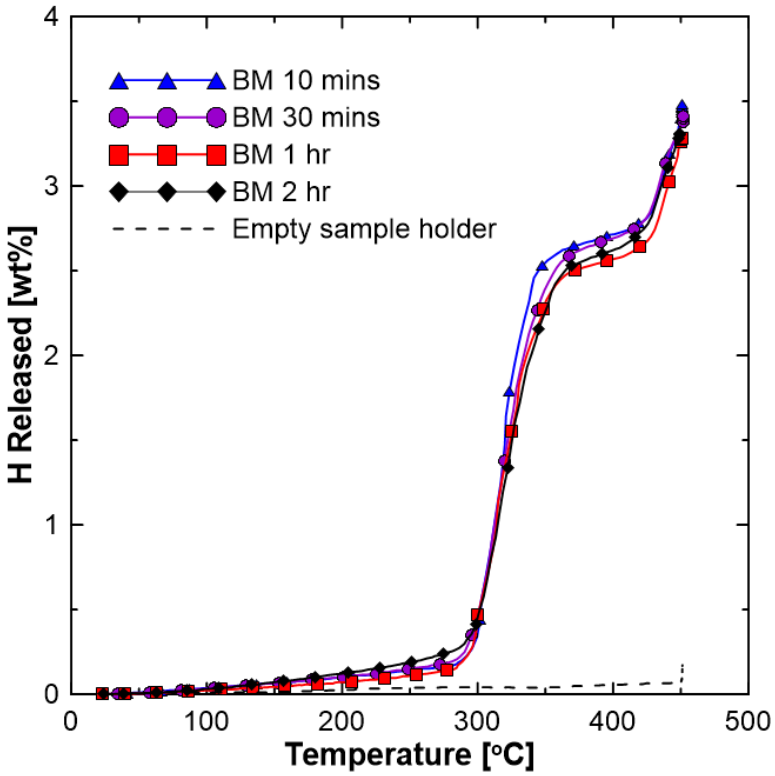

Figure 4.24: TPD study of ball milled $4NaBH_4$ / $5Mg_2NiH_4$ samples showing negligible impact on the onset of the desorption temperature for milling times up to 2 hours. The dashed line shows the 'apparent' hydrogen released due to gas heating.

There is a small loss in capacity with increasing the ball milling time, which has also been reported for other systems such as MgH_2 [2]. Ball milling for ten minutes shows the highest capacity at about 3.6 wt%, whereas 1 to 2 hours of ball milling shows 3.4 wt% H_2 release as seen in Figure 4.25. The total amount of hydrogen released from this system at 450 ºC is about 3.35 - 3.5 wt%. This is about 1 wt% less than the expected value of 4.5 wt%, when the decomposition proceeds to NaH (chapter 4.1). For these measurements, a small (11.67 ml) reservoir volume was used. The pressure rise, in these measurements, soon reached the equilibrium solid / gas pressure hence preventing further release of hydrogen. If we were to repeat these experiments a larger reservoir volume could be used to reduce

the impact of hydrogen back pressure. The impact of hydrogen back pressure and choice of reservoir volumes is discussed in section 4.5 in more detail.

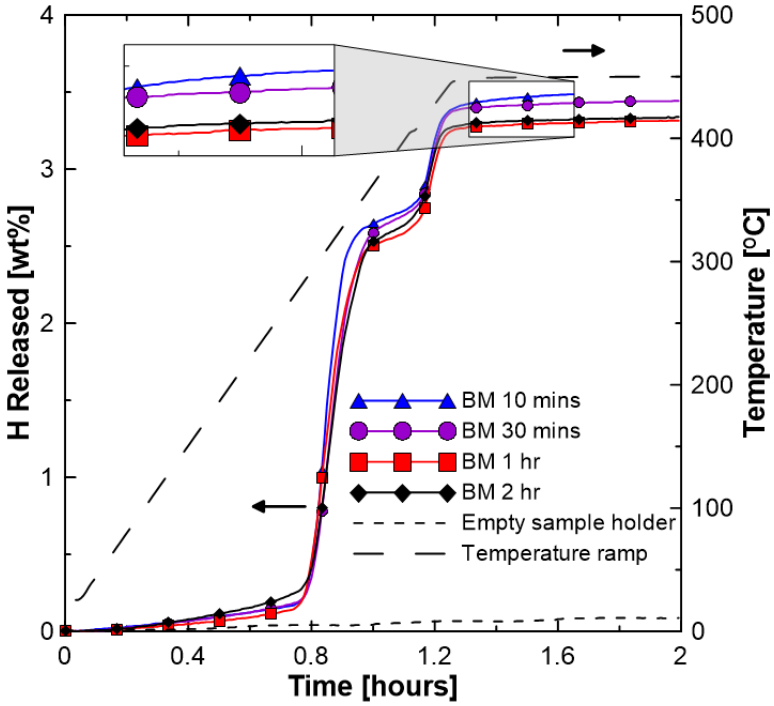

Figure 4.25: The variation in hydrogen release and temperature with respect to the milling time is about 0.15 wt% H_2.

DSC analysis was also conducted for each of the ball milled samples. Some small differences between the milling times were observed, however, the major endotherms, corresponding to hydrogen desorption, were centered in the range of 325 - 350 ºC and 430 - 460 ºC (Figure 4.26). The first major endotherm (II) corresponds to the decomposition of Mg_2NiH_4 and the second major endotherm (III) is that of $NaBH_4$ decomposition. The determination of the phases is discussed further in section 4.3.

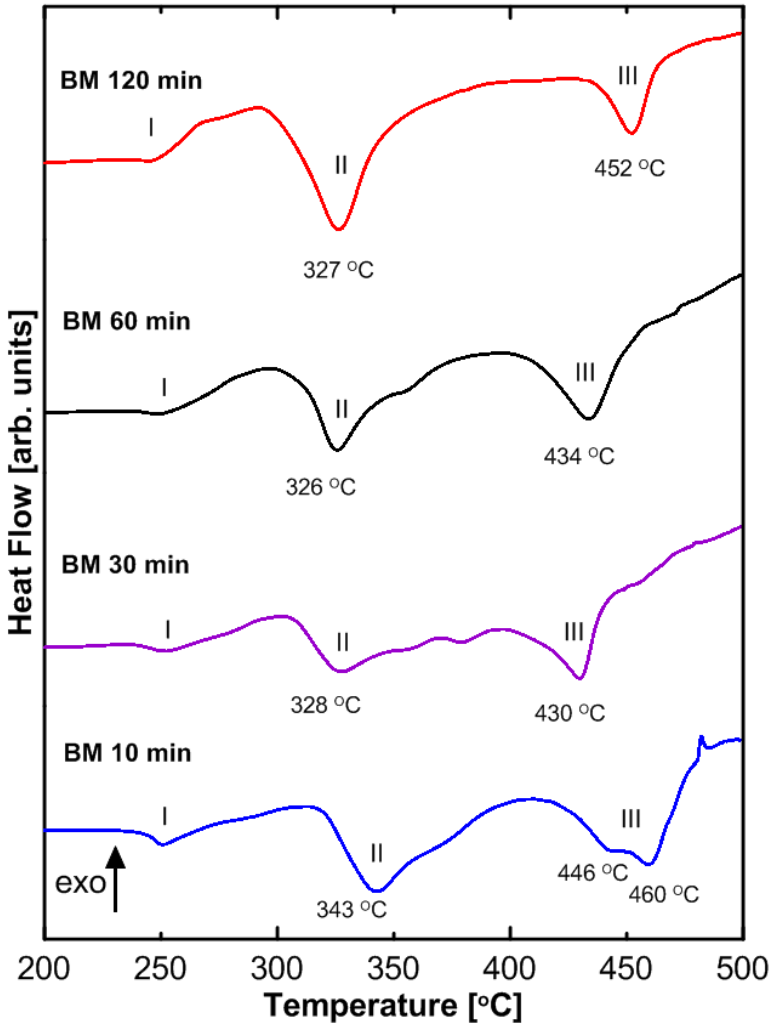

Figure 4.26: DSC Ball Mill study for $4NaBH_4$ / $5Mg_2NiH_4$ showing the major endotherms (II and III) for the powder mixture at between 325 - 350 ºC and 430 - 460 ºC. Endotherm designation: I: phase transition from monoclinic to fcc cubic, II: decomposition of Mg_2NiH_4, III: decomposition of $NaBH_4$.

There is a slight endothermic event (I) which decreases with the milling time of the composite system (Figure 4.26). This feature corresponds to a phase transition of Mg_2NiH_4. Before decomposition, Mg_2NiH_4 converts from a monoclinic phase to a fcc cubic structure [41]. This may indicate that as the mixture is ball milled for longer periods of time, the

phase change may no longer occur. This may be because the phase change to fcc occurs during ball milling, or because ball milling suppresses the phase change to fcc. XRD scans of the powder taken after ball milling do not show the fcc phase of Mg_2NiH_4, indicating that a phase change from monoclinic to fcc does not occur during ball milling. Whether the fcc transformation occurs during heating is unknown. In-situ XRD may help clarify this, however, we did not have access to this equipment.

Figure 4.27 shows the XRD patterns of $4NaBH_4$ / $5Mg_2NiH_4$ ball milled for different periods of time. Varin et al. have reported that upon ball milling γ-MgH_2 forms which has a slightly lower dehydrogenation temperature than MgH_2 [2]. The γ-MgH_2 usually forms under intense static pressure (8 GPa). For the $4NaBH_4$ / $5Mg_2NiH_4$ mixture no phase changes were observed after ball milling.

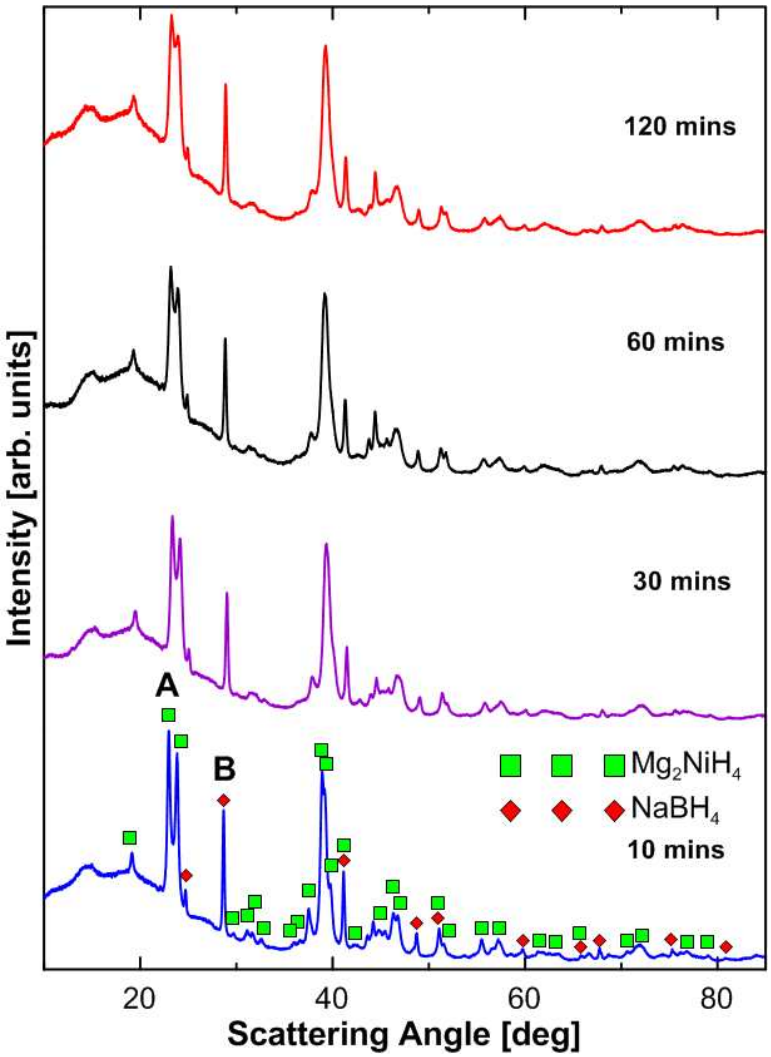

Figure 4.27: XRD patterns of the ball milled $4NaBH_4$ / $5Mg_2NiH_4$ powder at 10, 30, 60, and 120 minutes. The patterns are very similar, indicating no phase change. A broadening of the diffraction peaks can be observed (deg in 2θ).

Grain sizes were obtained using the broadening of the Bragg peaks (see section A.3.2) determined through a program written in Python (see appendix E) and the results are shown in Figure 4.28. For Mg_2NiH_4 and $NaBH_4$, scattering angles of $2\theta = 23.4°$ (A) and $2\theta = 29°$ (B) were used, respectively. Each of these scattering angles is unique to its respective phase and does not overlap with other peaks (Figure 4.27). Varin et al. have reported that

$NaBH_4$ is remarkably tough and resistant to ball milling resulting in little change in grain size after several hours of milling [2]. It can be seen that after 30 minutes of ball milling the grain size plateaus and does not change significantly for $NaBH_4$. The Mg_2NiH_4 grain size also remains unchanged after 30 minutes. This is most likely because the powder has already been milled for an hour during synthesis.

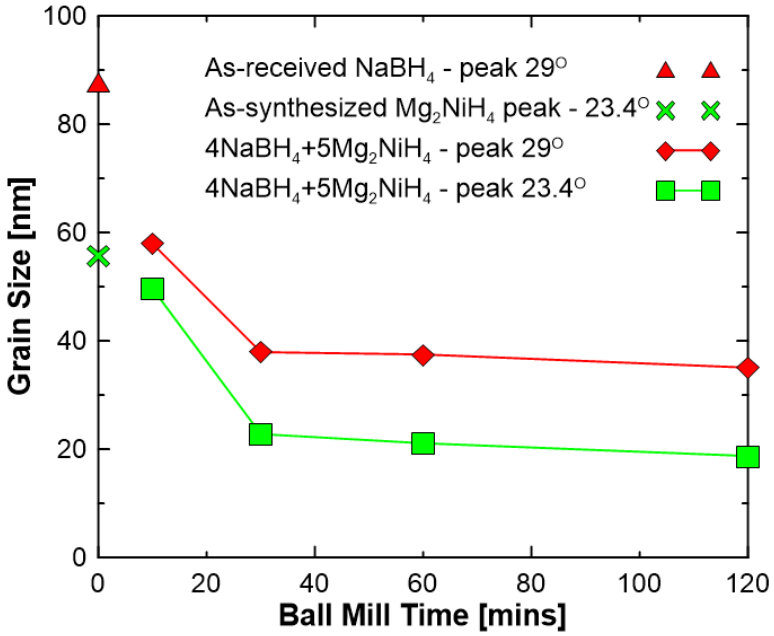

Figure 4.28: XRD grain size analysis of ball milled samples at 10, 30, 60 and 120 minutes for the mixture $4NaBH_4$ / $5Mg_2NiH_4$, and the grain size for the as received $NaBH_4$ and just synthesized Mg_2NiH_4 are shown at time zero.

Scanning electron microscopy (SEM) analysis of the ball milled samples after each stage of milling was performed to determine the effect of milling time on the particle size and shape. Figure 4.29 shows SEM images of both Mg_2NiH_4 and $NaBH_4$ before ball milling. The Mg_2NiH_4 particle size is much smaller than that of $NaBH_4$.

Mg_2NiH_4

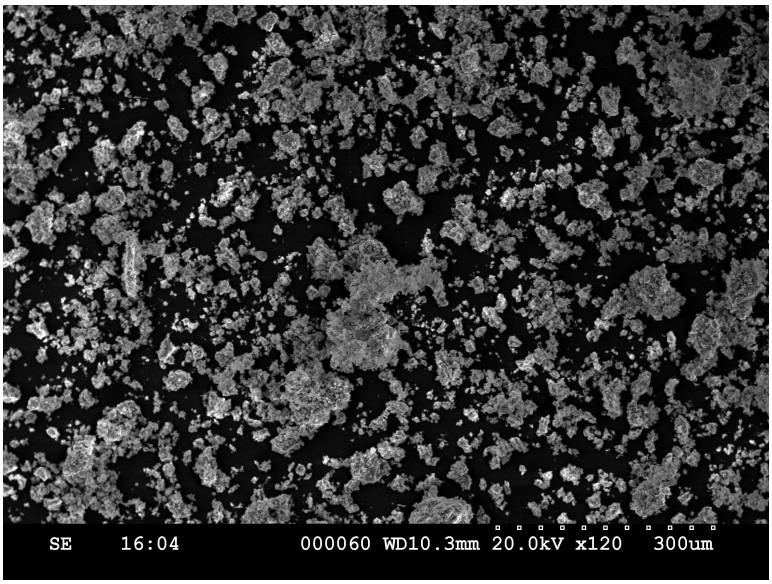

$NaBH_4$

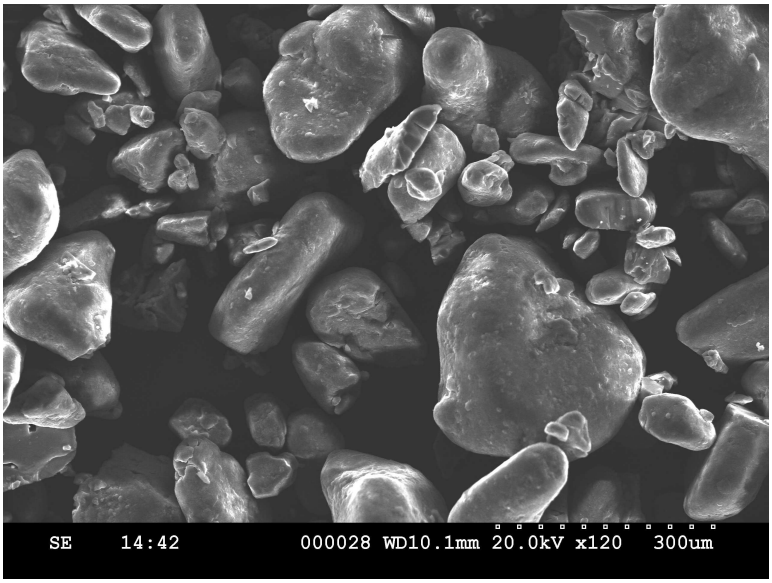

Figure 4.29: SEM analysis of as synthesized Mg_2NiH_4 and as received $NaBH_4$ shown at the same scale. The Mg_2NiH_4 particle size is much smaller than the $NaBH_4$. Scale 300 μm.

Figure 4.30 shows that ball milling $NaBH_4$ for 10 minutes to 2 hours does not yield

significant changes. The as received $NaBH_4$ shows some particle size reduction and the shape has changed from a smooth rounded surface to a jagged fractured surface with ball milling.

$NaBH_4$ ball milled 10 minutes

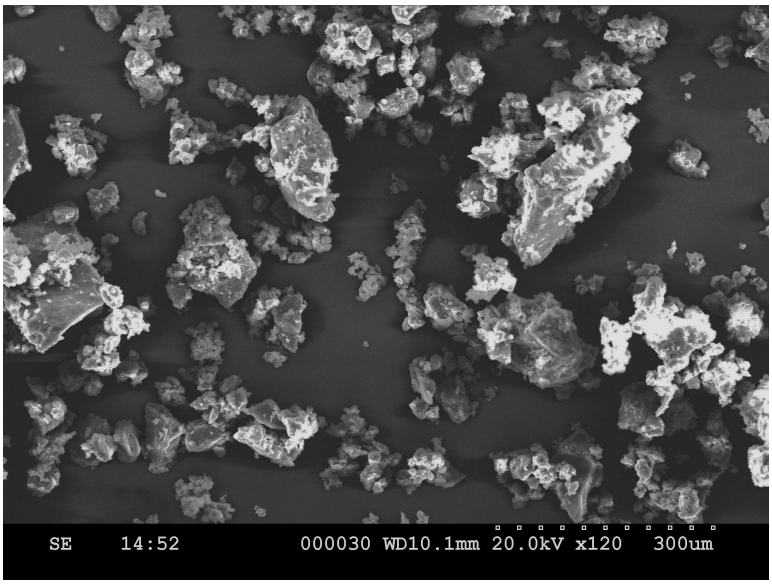

$NaBH_4$ ball milled 2 hours

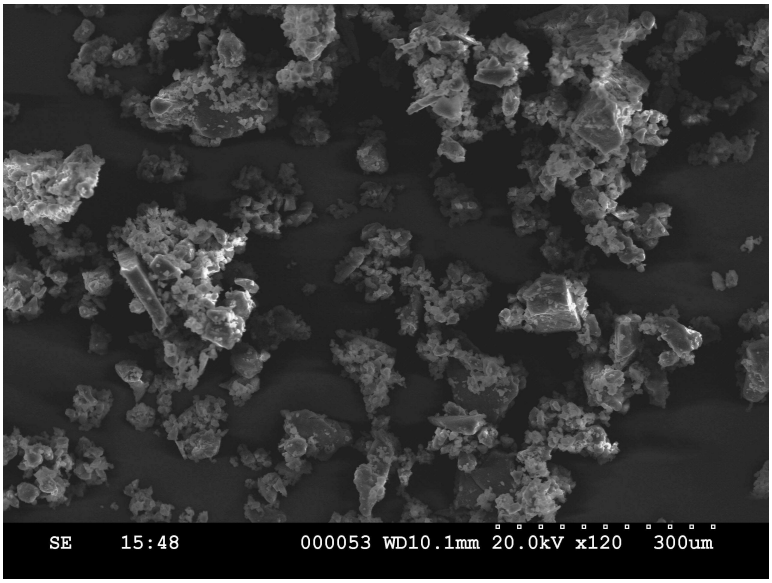

Figure 4.30: $NaBH_4$ ball milled for 10 minutes and 2 hours shows little difference, both show a fractured and jagged surface. Scale 300 μm.

Figure 4.31 shows that ball milling the $NaBH_4$ / Mg_2NiH_4 mixture from 10 to 120 minutes also does not show any noticeable change in particle size. The insignificant change

in grain size and particle size due to ball milling may help explain why ball milling has no significant impact on the desorption kinetics.

10 mins

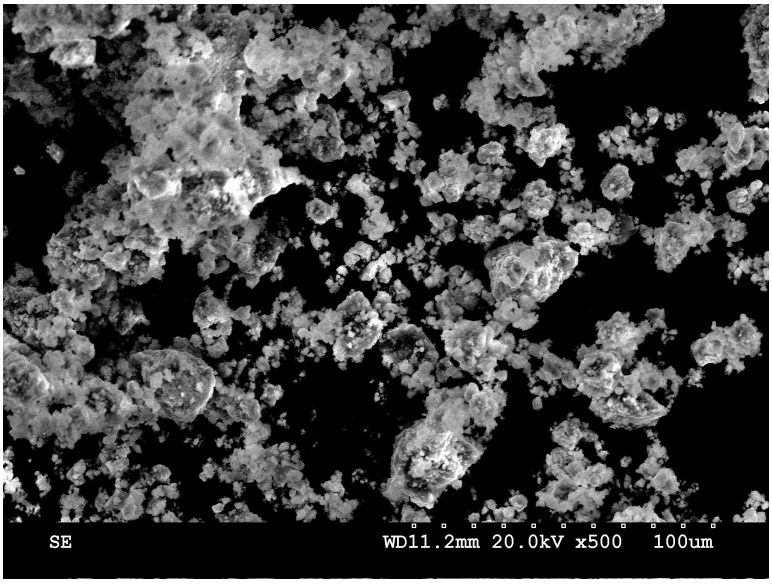

120 mins

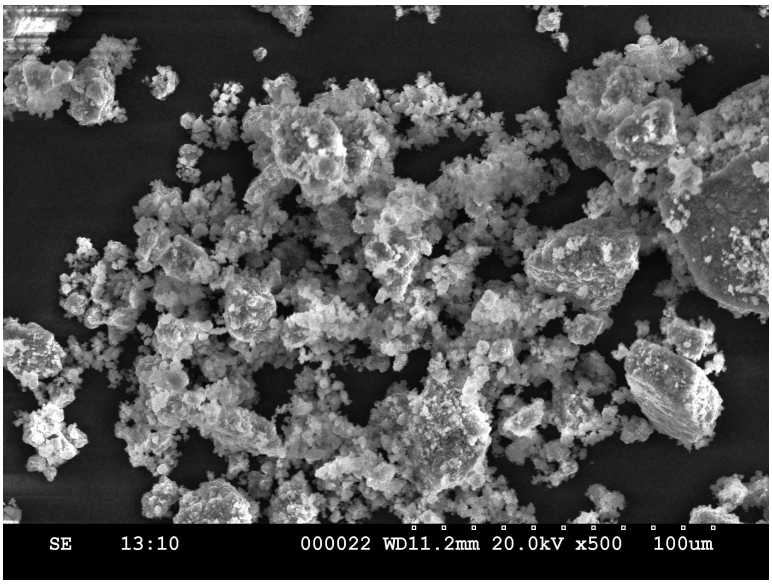

Figure 4.31: SEM of $4NaBH_4$ / $5Mg_2NiH_4$ ball milled for 10 and 120 minutes showing little impact on particle size. Scale 100 μm.

4.7 Hydrogen Absorption and Desorption Cycling Studies

The hydrogenation reversibility of a metal hydride system is important. Many systems have shown a loss of capacity after repeated cycling. In simpler systems like metal alloys (e.g., $LaNi_5H_6$, Mg_2NiH_4) decrepitation is the main cause [45, 2, 20]. Decrepitation is the breaking down of the hydride particles into smaller particles, often with the segregation of the atoms in the powder, as for example in $LaNi_5$ the separation of Ni [24]. In complex metal hydrides like borohydrides reversibility is difficult due to the high enthalpy of absorption which requires high temperatures and pressures [22].

The first cycling experiments for $4NaBH_4$ / $5Mg_2NiH_4$ composite consisted of a set of four experiments as shown in Figure 4.32. The details of the experimental parameters are discussed in section 3.2.5. The desorption experiments were performed with a small (11.7 ml) reservoir volume, which limited the desorption of the $4NaBH_4$ / $5Mg_2NiH_4$ composite as discussed in section 4.5. The loss of 0.7 wt% H after the first desorption occurs because of the formation of $MgNi_2$, which is a non hydriding alloy that forms during the hydrogen absorption step from the Ni rich $MgNi_{2.5}B_2$ (see section 4.3).

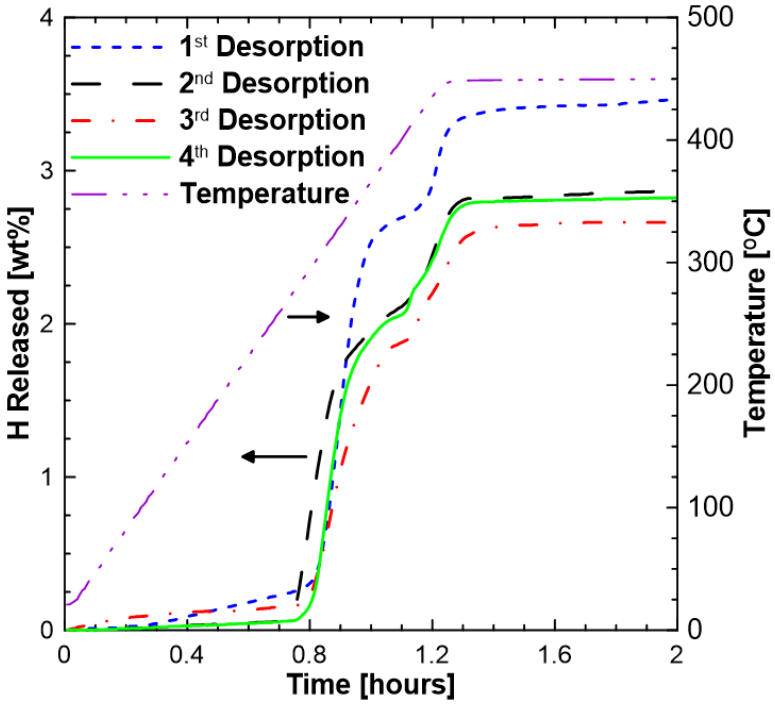

Figure 4.32: Analysis of cycled $4NaBH_4$ / $5Mg_2NiH_4$. A loss of 0.7 wt% H is observed due to the formation of $MgNi_2$.

Figure 4.33 shows the hydrogen capacity of two different batches of $4NaBH_4$ / $5Mg_2NiH_4$ composites as a function of cycling. The capacity loss is about 0.7 wt % H during the first 4 cycles. Vajo et al. observed a similar loss in capacity of 0.6 wt% H during cycling tests for the $4LiBH_4$ / $5Mg_2NiH_4$ composite, however they did not provide any explanations. They also observe a stabilization in reversible capacity after the first desorption from about 1.8 to 1.2 wt% H. They also noticed that longer ball milling times, up to 48 hours, improved the reversible capacity by up to 1.7 wt% H [4].

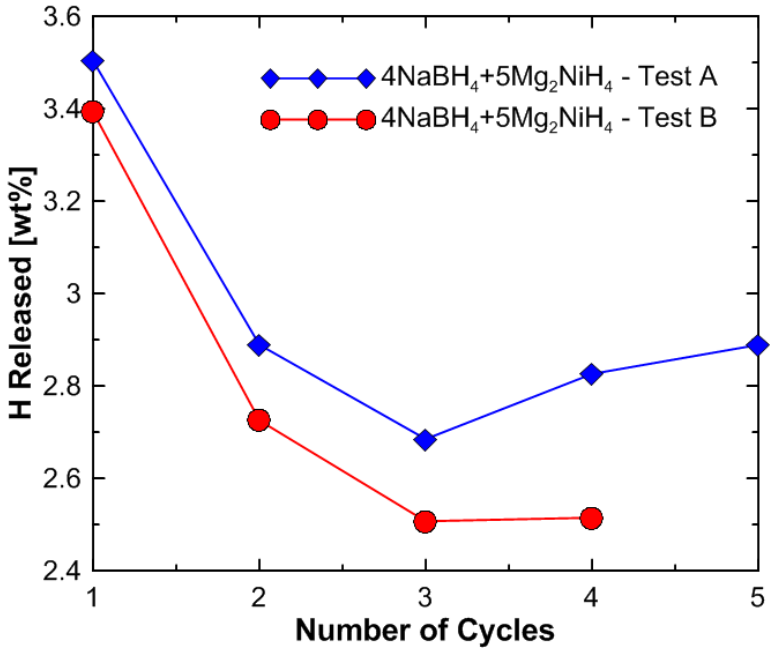

Figure 4.33: $4NaBH_4$ / $5Mg_2NiH_4$ H_2 capacity as a function of cycling. Two identical tests with different batches were run: Test A and Test B. Both tests show a similar drop in capacity.

In addition to these TPD cycling experiments, isothermal cycling experiments were also performed at 450 ºC. The first step consisted of a TPD scan made at 6 ºC min^{-1} and subsequent desorption and absorption steps were all done at 450 ºC. Figure 4.34 shows the isothermal hydrogen desorption /absorption cycling in the $4NaBH_4$ / $5Mg_2NiH_4$ composite. For these measurements larger reservoir volumes (167.7 and 1056.3 ml) were used to fully desorb the hydrogen content of the composite. The first two desorption measurements show capacity of 4-5 wt% H. However, after a few cycles, capacity drops to 3 wt% H (similar to data shown in Figure 4.33).

Table 4.8 shows the volumes and pressures used for the isothermal cycling experiments. For test a the pressure was maintained at about 1-2 bar during desorption and 84 bar for absorption. This allowed for complete decomposition of $NaBH_4$ to NaH as the reservoir

pressure was kept below the equilibrium desorption pressure of $NaBH_4$, but above that of NaH. An absorption pressure of 84 bar allowed for complete absorption of the $4NaBH_4$ / $5Mg_2NiH_4$ composite.

For test b, a pressure of about 4.5 bar was maintained throughout the desorptions. The desorption of hydrogen from $NaBH_4$ was limited under this hydrogen back pressure to plateau II as shown in Figure 4.20. Therefore, only partial decomposition of $NaBH_4$ to NaH was attained. Absorption at 84 bar allowed for complete absorption.

The hydrogen pressure for absorption for test c was lowered to 57 bar, which is below the equilibrium absorption pressure for Mg_2NiH_4 (about 67 bar). Accordingly, only the $NaBH_4$ phase of the composite was hydrogenated. The hydrogen back pressure for desorption was maintained at about 3.5 bar. The partial decomposition of $NaBH_4$ similar to test b was observed.

Table 4.8: Parameters for the isothermal cycling studies

Test	**1st TPD Desorp. pressure [bar]**	**Isothermal Desorp. pressure [bar]**	**Desorp. Volume [ml]**	**Abs. Pressure [bar]**	**Abs. Volume [ml]**
a	1	1-2	1056.3	84	167.7
b	1	4.5	167.7	84	167.7
c	1	3.5	167.7	57	11.7

Figure 4.34 shows the gravimetric capacity as a function of cycle number for three different sets of absorption and desorption settings. The first curve (a) shows a gradual loss of capacity from about 4.75 to about 2.5 wt% H, which is consistent with the TPD cycling experiments. Curve (b) is similar to curve (a), however the loss in capacity seems to occur much sooner. This is due to the limited desorption of $NaBH_4$ in experiment b. This implies that there is a gradual loss in capacity due to the decomposition of $NaBH_4$ after plateau II.

Curve (c) shows an immediate loss of capacity to about 1 wt% H. The capacity is constant over four cycles and it is representative of the partial decomposition of $NaBH_4$

as shown in Figure 4.20 from plateau I to Plateau II. This indicates that there is no loss in capacity from this step.

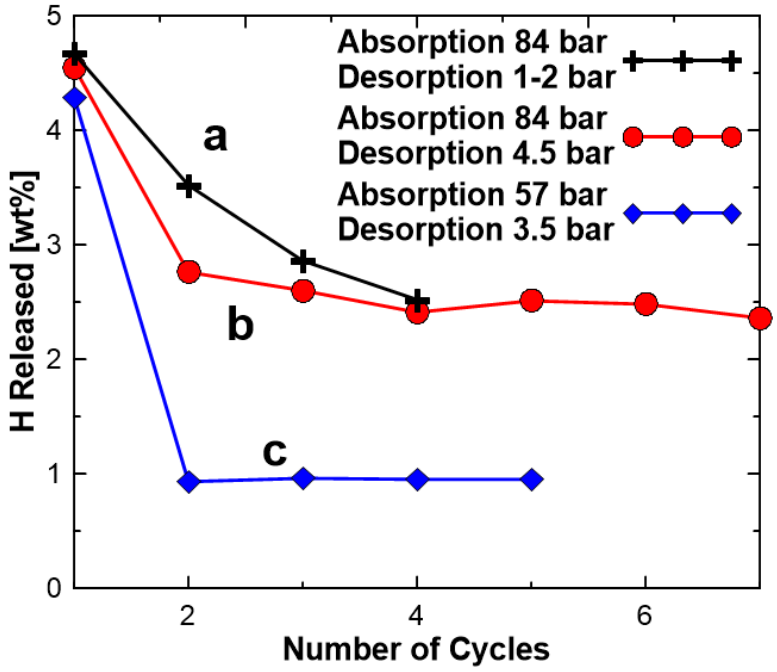

Figure 4.34: Capacity as a function of the number of cycles for isothermal cycling.

4.8 Hydrogen Desorption Kinetics of $4NaBH_4$ / $5Mg_2NiH_4$

The hydrogen desorption kinetics of the $4NaBH_4$ / $5Mg_2NiH_4$ system were examined using differential scanning calorimetry and the Kissinger method as described in section 3.3.5 and section 2.3.1. For these measurements the sample is heated at a constant heating rate (β = 4, 6, 8, 10 ºC min^{-1}) and the heat flow in and out of the sample is recorded. Figure 4.35 shows the DSC scans for different heating rates β. The first major endotherm (I), associated with the decomposition of Mg_2NiH_4, showed a systematic shift to higher temperatures when the heating rate β was increased. The second endotherm (II), associated with the decomposition of $NaBH_4$, however, decreases with the first two increases in β and then

increases significantly when β is increased to 10 °C min^{-1}. This makes the application of the Kissinger method difficult. The scatter in endotherm II's position may be a consequence of experimental conditions such as: reaction of the sample with the pan, the presence of residual air in the instrument, or sample loss during the heating. Sample loss during the heating may be a consequence of the sample foaming when it is heated beyond about 425 °C.

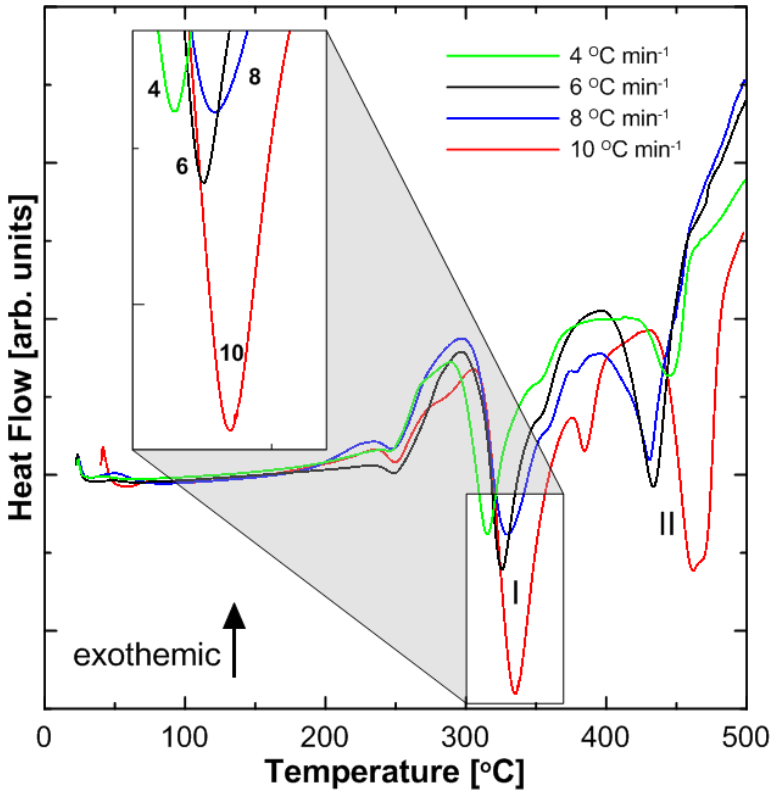

Figure 4.35: DSC scan of the $4NaBH_4$ / $5Mg_2NiH_2$ composite for different heating rates (β). The first endotherms' (I) peak positions increases with heating rate. The second endotherms (II) do not show a similar behavior.

Figure 4.36 shows the Kissinger analysis for the $4NaBH_4$ / $5Mg_2NiH_4$ mixture for the first endotherm. From the slope of the data an activation energy E_a = 131 $\pm$ 24 kJ mol^{-1} is obtained with an R^2 value of the linear fit of about 0.988, indicating a good fit.

However, when compared to the activation energy obtained from the ball milled Mg_2NiH_4 in section 4.2 of 73 $\pm$ 9 kJ mol^{-1} this is a substantial increase. The Mg_2NiH_4 activation energy as reported by Selvam et al. [40] is 183 kJ mol^{-1}. They prepared their Mg_2NiH_4 through the mixing of stoichiometric amounts of Ni and Mg which was then melted and powdered several times under argon. The resulting Mg_2Ni powder was then hydrogenated. The particle and grain size of their Mg_2NiH_4 particles would likely be larger than those created in our lab and could account for the discrepancy in activation energy.

The discrepancy in activation energy of hydrogen desorption has been reported in other systems such as MgH_2, $NaAlH_4$ [40, 2], and is most likely related to the surface properties of the system including surface area, grain size, oxidation, presence of catalysts and activation procedures [2, 20]. Varin et al. have reported activation energies for MgH_2 that range from 118 - 160 kJ mol^{-1} depending on the manufacturer of the powder, whether it was activated or not, whether it was ball milled or not, etc. They also reported that samples exposed to air had activation energies of 230 - 300 kJ mol^{-1}, which they reported were high because of moisture and air reacting with the Mg particles to form $Mg(OH)_2$ and MgO shells around the particles [2].

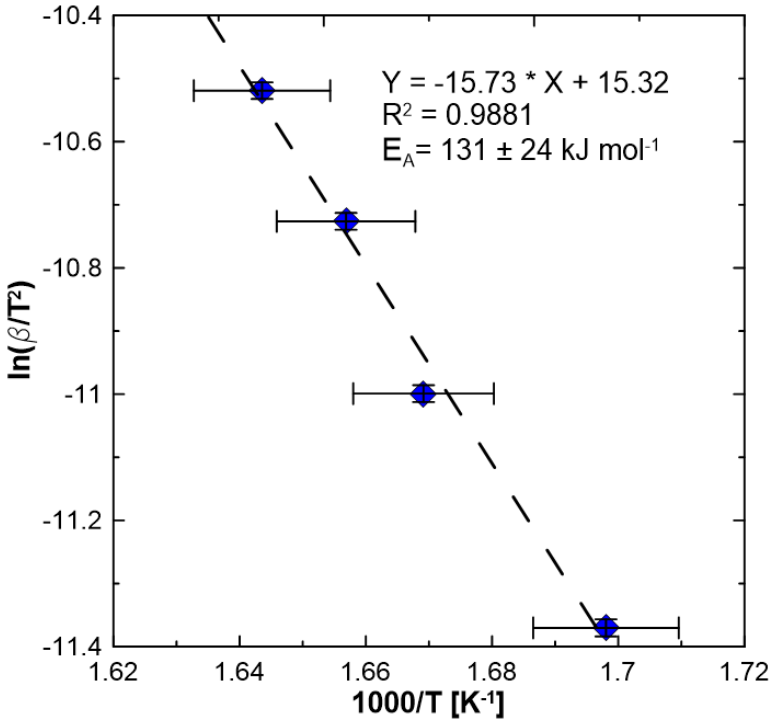

Figure 4.36: Fitted curve for Kissinger analysis of the first DSC endotherm (I).

The activation energy determined for the Mg_2NiH_4 component of the $4NaBH_4$ / $5Mg_2NiH_4$ mixture indicate that the hydrogen desorption kinetics of Mg_2NiH_4 are more sluggish than the kinetics of Mg_2NiH_4 alone. The reasons for the difference are unclear as the Mg_2NiH_4 in the composite seems to decompose alone in the $4NaBH_4$ / $5Mg_2NiH_4$ mixture. It could be that any free Ni that may have existed in the Mg_2NiH_4 after synthesis and may have acted as a catalyst was now spread out over both compounds and thus not as concentrated and available to the Mg_2NiH_4.

The theoretical thermodynamic temperature of desorption for the $NaBH_4$ component in the $4NaBH_4$ / $5Mg_2NiH_4$ composite is 311 ºC, however the observed temperature of desorption is 360 ºC. The difference is perhaps due to poor kinetics. Milanese et al. reported an improvement in kinetics from the addition of 3 wt% MgF_2 to the $NaBH_4$ / MgH_2 system

by decreasing the onset temperature from 440 to 410 ºC for the $NaBH_4$ component [31]. Bosenberg et al. reported that the addition of titanium isopropoxide to the $LiBH_4$ / MgH_2 system improved the kinetics by decreasing the onset of desorption of the MgH_2 component of the composite from 375 to 355 ºC [28]. The addition of catalysts such as MgF_2 to the $4NaBH_4$ / $5Mg_2NiH_4$ composite may improve the kinetics and improve the temperature of desorption so that it is closer to that calculated thermodynamically.

4.9 Comparison of Different Complex Metal Hydride Composites

Figure 4.37 shows the TPD analysis of the compounds Mg_2NiH_4, MgH_2, $NaBH_4$, $LiBH_4$ and their combinations. Hydrogen desorption in $NaBH_4$ occurs above 500 ºC. Addition of MgH_2, however reduces the onset of desorption to about 460 ºC. Thermodynamic destabilization has occurred. However, the kinetics were too sluggish during testing and the full curve is not shown. Addition of Mg_2NiH_4 to $NaBH_4$ has a much more pronounced effect on destabilizing the $NaBH_4$, consequently the onset of desorption is now about 360 ºC. There is no concerted reaction between the Mg_2NiH_4 and $NaBH_4$ during the first step of the dehydrogenation. In the $4LiBH_4$ / $5Mg_2NiH_4$ system, however, Vajo et al. reported that hydrogen release commences at 250 ºC via a concerted reaction between Mg_2NiH_4 and $LiBH_4$ [4].

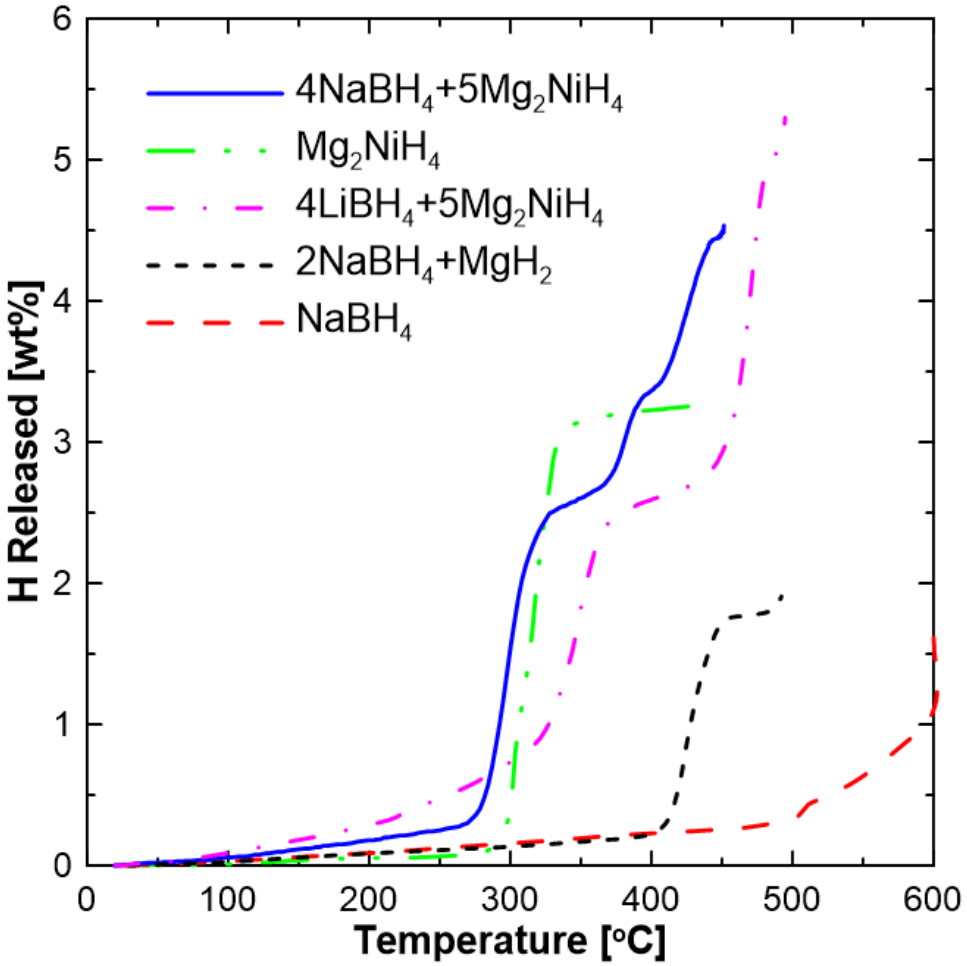

Figure 4.37: Comparison of $LiBH_4$ and $NaBH_4$ based composites and the destabilizing effect of MgH_2 and Mg_2NiH_4.

Table 4.9 shows a comparison of hydrogen storage properties for the systems shown in Figure 4.37.

Table 4.9: Comparison of several hydride storage systems (under 1 bar hydrogen pressure)

System	ΔH_{des} **[kJ mol**$_{H_2}{}^{-1}$**]**	T_{des} **(observed) [ºC]**	**H weight [%]**
$4NaBH_4/5Mg_2NiH_4$	75	360	4.5
Mg_2NiH_4	65	280	3.6
$4LiBH_4/5Mg_2NiH_4$	15	250	2.5
$2NaBH_4/MgH_2$	62-100.58 [35, 31, 34]	450	9.88
$NaBH_4$	106.8	577	10.8

4.10 Summary

Monoclininc Mg_2NiH_4 was synthesized and characterized. The hydrogen desorption and absorption enthalpy were 74 $\pm$ 5 and 60 $\pm$ 3 kJ $mol_{H_2}^{-1}$, respectively. The activation energy of the hydrogen desorption reaction was about 73 $\pm$ 9 kJ mol^{-1}. Heating Mg_2NiH_4 to 300 ºC and 1 bar led to formation of Mg_2Ni and hydrogen release. Mg_2Ni can be reversibly hydrogenated to form Mg_2NiH_4.

Crystallographic phase analysis shows that $4NaBH_4$ / $5Mg_2NiH_4$ decomposes in at least three steps with the first step being the decomposition of Mg_2NiH_4 starting at around 275 ºC, the second step the decomposition of $NaBH_4$ to form NaH (at about 360 ºC), and the third step the decomposition of NaH to Na at around 425 - 450 ºC. The $MgNi_{2.5}B_2$ compound forms by 400 ºC.

The thermodynamics of $4NaBH_4$ / $5Mg_2NiH_4$ were studied using a manometric method and the enthalpy of decomposition was determined to be 67 $\pm$ 4, 76 $\pm$ 5 and 95 $\pm$ 7 kJ $mol_{H_2}^{-1}$ for the decomposition of Mg_2NiH_4, $NaBH_4$ and NaH respectively. This compares to a decomposition enthalpy of 66, 90 and 96-114 kJ $mol_{H_2}^{-1}$ for Mg_2NiH_4, $NaBH_4$, and NaH, respectively. The absorption enthalpy of 59 $\pm$ 4 kJ $mol_{H_2}^{-1}$ corresponding to the Mg_2NiH_4 phase of the composite was obtained. The onset temperature of hydrogen desorption for $NaBH_4$, in the composite, was reduced to about 360 ºC from 500 ºC for pure $NaBH_4$ and

450 ºC for $2NaBH_4$ / MgH_2 indicating thermodynamic destabilization.

$4NaBH_4$ / $5Mg_2NiH_4$ was tested under a hydrogen back pressure of vacuum, 1 and 5 bar. Formation of the ternary boride $MgNi_{2.5}B_2$ did not show any dependance on hydrogen back pressures.

The $4NaBH_4$ / $5Mg_2NiH_4$ composite was ball milled for 10, 30, 60 and 120 minutes. No effect on the desorption kinetics or thermodynamics was found due to ball milling. A small capacity loss of about 0.15 wt% was noticed for ball milling up to 120 minutes. Grain size of the composite $4NaBH_4$ / $5Mg_2NiH_4$ was affected slightly due to ball milling with a reduction from about 90 nm to about 40 nm for the $NaBH_4$, and 55 nm to 20 nm for the Mg_2NiH_4. Both of these reductions in grain size occurred within 30 minutes of ball milling. Particle size analysis showed little change in particle size for ball milling up to 120 minutes. The desorption kinetics may not be affected due to the small change in particle size.

Hydrogen absorption and desorption into the $4NaBH_4$ / $5Mg_2NiH_4$ composite was studied up to 5 cycles. A loss in capacity of about 0.7 wt% hydrogen was observed due to the formation of the non-hydriding phase $MgNi_2$ and the loss of Na outside of the sample holder. Isothermal cycling tests were conducted under back pressures of 1 to 4.5 bar and absorption pressures of 57 and 84 bar. Hydrogen capacity during these cycles, reduced from about 4.5 to 2.5 wt% H for experiments rehydrogenated under 84 bar hydrogen, and 4.5 to 1 wt% H for experiments rehydrogenated under 57 bar hydrogen pressure.

Kinetic analysis of $4NaBH_4$ / $5Mg_2NiH_4$ was undertaken using the Kissinger method and an activation energy of 131 ± 24 kJ mol^{-1} was obtained for the decomposition of the Mg_2NiH_4 composite. Determination of the desorption activation energy for the $NaBH_4$ component in the composite was not possible with DSC. The activation energy of the $NaBH_4$ component in the composite may be determined by the Arrhenius method instead of the Kissinger method.

The effect of hydrogen absorption / desorption cycling on the phases formed was stud-

ied. The loss in hydrogen capacity of the Mg_2NiH_4 phase during cycling resulted from: a) the formation of $MgNi_2$ (non-hydriding binary alloy), b) the formation of non-hydrogenable Mg and, c) the loss of Na from the sample holder.

The TPD analysis of compounds like Mg_2NiH_4, MgH_2, $NaBH_4$, $LiBH_4$ and their combinations were compared. The $4NaBH_4$ / $5Mg_2NiH_4$ composite had an observed dehydrogenation of the $NaBH_4$ component starting at 360 ºC, the $NaBH_4$ component of the $NaBH_4$ / MgH_2 composite started desorbing hydrogen at 450 ºC. In the $4LiBH_4$ / $5Mg_2NiH_4$ composite the concerted reaction between the two components of the system started desorbing hydrogen at 250 ºC. The individual complex hydrides $NaBH_4$ and Mg_2NiH_4 showed hydrogen desorption at 577 and 280 ºC respectively.

Chapter 5

Conclusions

A novel complex hydride composite $4NaBH_4$ / $5Mg_2NiH_4$ was successfully prepared, and examined as a potential hydrogen storage material. Single phase Mg_2NiH_4 was synthesized by ball milling and solid state reactions at 495 ºC and under 95 bar hydrogen pressure. Mixtures of $4NaBH_4$ / $5Mg_2NiH_4$ were then prepared by ball milling, and hydrogen absorption / desorption experiments were performed. The addition of Mg_2NiH_4 led to a successful thermodynamic destabilization of $NaBH_4$ through formation of $MgNi_{2.5}B_2$. This destabilization reduced the hydrogen desorption temperature of $NaBH_4$ from 577 to 360 ºC under 1 bar hydrogen. The initial desorption capacity of this composite is about 5 wt%.

Hydrogen desorption from $4NaBH_4$ / $5Mg_2NiH_4$ was determined to occur in three steps:

Reaction 1	$4NaBH_4 + 5Mg_2NiH_4 \rightleftharpoons 4NaBH_4 + 5Mg_2Ni + 10H_2$	$\Delta H = 67 \pm 4$ kJ $mol_{H_2}^{-1}$
Reaction 2	$4NaBH_4 + 5Mg_2Ni \rightleftharpoons 4NaH + 2MgNi_{2.5}B_2 + 8Mg + 6H_2$	$\Delta H = 76 \pm 5$ kJ $mol_{H_2}^{-1}$
Reaction 3	$NaH \rightleftharpoons Na + H$	$\Delta H = 95 \pm 7$ kJ $mol_{H_2}^{-1}$

The enthalpies of hydrogen desorption for $NaBH_4$ and NaH are reported to be 106.8 and 114 kJ $mol_{H_2}^{-1}$ respectively. Thus the addition of Mg_2NiH_4 has led to the reduction of the enthalpies of $NaBH_4$ and NaH. Formation of the stable ternary boride $MgNi_{2.5}B_2$ leads to this destabilization. The enthalpy of absorption corresponding to Mg_2NiH_4 in the composite was 59 ± 4 kJ $mol_{H_2}^{-1}$.

The impact of ball milling time, desorption back pressure, and hydrogen absorption /

desorption cycling was also studied. The following conclusions could be drawn:

- Ball milling the $4NaBH_4$ / $5Mg_2NiH_4$ for up to 2 hours had little impact on the crystallinity and the hydrogen desorption / absorption properties of this mixture.
- $MgNi_{2.5}B_2$, was formed under 0, 1, and 5 bar of hydrogen back pressure during the desorption step. This is in contrast to $4LiBH_4$ / $5Mg_2NiH_4$ where a back pressure of at least 3 bar is required.
- The $4NaBH_4$ / $5Mg_2NiH_4$ composite was cycled a few times to assess the repeated hydrogen release / uptake. The initial capacity of about 4.8 wt% H was reduced to about 2.5 wt% H after 4 cycles. The loss in capacity is attributed to the formation of $MgNi_2$ and loss of Na.
- Measurements of the activation energy of hydrogen desorption from Mg_2NiH_4 alone and mixed with $NaBH_4$ yielded 73 ± 9 and 131 ± 24 kJ mol^{-1} respectively.

The use of $NaBH_4$ (with more abundant Na) to replace $LiBH_4$ in the complex metal hydride composite looks promising and generally provided better performance.

5.1 Future Work

- Formation of other possible ternary boride phases can be investigated. For these experiments, binary magnesium hydrides such as Mg_2FeH_6 or Mg_2CoH_5 and complex metal hydrides like $NaBH_4$ or $LiBH_4$ can be used. There are no reports of mixtures of these composites.
- Mixtures of alanates, such as $NaAlH_4$, and binary hydrides like Mg_2NiH_4 can also be studied. Here Al would form a ternary phase with the Mg and Fe or Co. One of the more attractive reasons for using aluminum is its relative abundance and low cost

relative to boron. Mg_2AlNi_2 alloys are known to form and have been reported by Parente et al. [46].

- To improve the kinetics of hydrogen desorption and absorption the addition of catalysts can be investigated. Catalysts such as TiF_3 and $TiCl_3$ have been shown to improve hydrogen desorption and absorption rates in $NaAlH_4$ and $LiBH_4$, as well as the composite system $NaBH_4$ / MgH_2 [23, 35].

- Preliminary tests have shown that ball milling the hydride system for up to 24 hours significantly reduces the hydrogen desorption temperature, with a concerted desorption starting at around 100ºC. The necessity for long term ball milling of $NaBH_4$ may be due to the hardness of $NaBH_4$. Studies of extended ball milling times up to 24 hours or more are thus recommended. Ball milling $NaBH_4$ alone for an extended time and then mixing with Mg_2NiH_4 is also suggested because the composite may release hydrogen during milling. This may occur because of the large energy input from the ball milling, which may cause the composite to reach the desorption temperature over extended milling times. This will be a concern if the temperature of desorption for the composite is lowered enough to bring it into the temperature range of the ball milling jar during milling.

- Because of the difficulty in determining the phase transitions and reaction pathways of the hydride system during decomposition and absorption, in-situ thermal XRD would be very useful. During in-situ XRD diffraction, patterns of the sample are collected while the temperature of the sample is changed. With ex-situ XRD, there is always a concern that when a sample is cooled, while hydrogen is not fully desorbed, some absorption may occur. See Appendix A.3.3.

Bibliography

[1] A Ter-Gazarian. *Energy storage for power systems*. P. Peregrinus-Institution of electrical engineers, Herts (GB), 1994.

[2] R.A. Varin, T. Czujko, and Z.S. Wronski. *Nanomaterials for Solid State Hydrogen Storage*. Fuel Cells and Hydrogen Energy. Springer, 2008.

[3] Professional Engineering Publishers. *Renewable Energy Storage: Its Role in Renewable and Future Electricity Markets*. IMechE Seminar Publication. Wiley, 2005.

[4] John J. Vajo, Wen Li, and Ping Liu. Thermodynamic and kinetic destabilization in $LiBH_4/Mg_2NiH_4$: promise for borohydride-based hydrogen storage. *Chemical Communications*, 46(36), 2010.

[5] J. J. Vajo, S. L. Skeith, and F. Mertens. Reversible storage of hydrogen in destabilized $LiBH_4$. *Journal of Physical Chemistry B*, 109(9), 2005.

[6] John J. Vajo and Gregory L. Olson. Hydrogen storage in destabilized chemical systems. *Scripta Materialia*, 56(10), 2007.

[7] Jun Yang, Andrea Sudik, and C. Wolverton. Destabilizing $LiBH_4$ with a metal (M = Mg, Al, Ti, V, Cr, or Sc) or metal hydride (MH_2, MgH_2, TiH_2, or CaH_2). *Journal of Physical Chemistry C*, 111(51), 2007.

[8] Gagik Barkhordarian, Thomas Klassen, Martin Dornheim, and Ruediger Bormann.

Unexpected kinetic effect of MgB_2 in reactive hydride composites containing complex borohydrides. *Journal of Alloys and Compounds*, 440(1-2), 2007.

[9] A. Zuttel, A. Borgschulte, and L. Schlapbach. *Hydrogen as a Future Energy Carrier*. John Wiley & Sons, 2008.

[10] Thomas Cherico Wanger. The lithium future-resources, recycling, and the environment. *Conservation Letters*, 4(3), 2011.

[11] Jun Yang, Andrea Sudik, Christopher Wolverton, and Donald J. Siegel. High capacity hydrogen storage materials: attributes for automotive applications and techniques for materials discovery. *Chemical Society Reviews*, 39(2), 2010.

[12] URL `http://www.h2can.ca/`.

[13] R. K. Ahluwalia, T. Q. Hua, J. K. Peng, S. Lasher, K. McKenney, J. Sinha, and M. Gardiner. Technical assessment of cryo-compressed hydrogen storage tank systems for automotive applications. *International Journal of Hydrogen Energy*, 35(9), 2010.

[14] Salvador .M. Aceves, Gene Berry, Diane Cooke, Francisco Espinosa-Loza, Elias Ledesma-Orozco, Ibo Matthews, Guillaume Petitpas, Tim Ross, Ray J. Smith, and Vernon Switzer. Extended dormancy, vacuum stability, and para-ortho hydrogen conversion in cryogenic pressure vessels. Technical report, Lawrence Livermore National Laboratory, Livermore, 2007.

[15] D. Teichmann, K. Stark, K. Muller, G. Zottl, P. Wasserscheid, and W. Arlt. Energy storage in residential and commercial buildings via liquid organic hydrogen carriers (lohc). *Energy & Environmental Science*, 5(10):9044–9054, 2012.

[16] A. Shukla, S. Karmakar, and R. B. Biniwale. Hydrogen delivery through liquid organic hydrides: Considerations for a potential technology. *International Journal of Hydrogen Energy*, 37(4):3719–3726, 2012.

[17] F. Sotoodeh and K. J. Smith. Kinetics of hydrogen uptake and release from heteroaromatic compounds for hydrogen storage. *Industrial & Engineering Chemistry Research*, 49(3):1018–1026, 2010.

[18] S. P. Verevkin, V. N. Emel'yanenko, and A. Heintz. Liquid organic hydrogen carriers: An upcoming alternative to conventional technologies. thermochemical studies. *Industrial & Engineering Chemistry Research*, 51(37):12150–12153, 2012.

[19] L. Schlapbach and A. Zuttel. Hydrogen-storage materials for mobile applications. *Nature*, 414(6861), 2001.

[20] M. Hirscher and K. Hirose. *Handbook of Hydrogen Storage: New Materials for Future Energy Storage*. John Wiley & Sons, 2010.

[21] Shin-ichi Orimo, Yuko Nakamori, Jennifer R. Eliseo, Andreas Zuettel, and Craig M. Jensen. Complex hydrides for hydrogen storage. *Chemical Reviews*, 107(10), 2007.

[22] I. P. Jain, Pragya Jain, and Ankur Jain. Novel hydrogen storage materials: A review of lightweight complex hydrides. *Journal of Alloys and Compounds*, 503(2), 2010.

[23] B. Bogdanovic, R. A. Brand, A. Marjanovic, M. Schwickardi, and J. Tolle. Metal-doped sodium aluminium hydrides as potential new hydrogen storage materials. *Journal of Alloys and Compounds*, 302(1-2), 2000.

[24] D.P. Broom. *Hydrogen Storage Materials: The Characterisation of Their Storage Properties*. Green Energy and Technology. Springer, 2011.

[25] M. S. Wellons, P. A. Berseth, and R. Zidan. Novel catalytic effects of fullerene for $LiBH_4$ hydrogen uptake and release. *Nanotechnology*, 20(20), 2009.

[26] M.W.J. Chase. *NIST-JANAF Thermochemical Tables*. Journal of physical and chemical reference data. Monograph. American Inst. of Physics, 1998.

[27] Bang Jie Zhang and Bin Hong Liu. Hydrogen desorption from $LiBH_4$ destabilized by chlorides of transition metal Fe, Co, and Ni. *International Journal of Hydrogen Energy*, 35(14), 2010.

[28] Ulrike Boesenberg, Stefania Doppiu, Lene Mosegaard, Gagik Barkhordarian, Nico Eigen, Andreas Borgschulte, Torbert R. Jensen, Yngve Cerenius, Oliver Gutfleisch, Thomas Klassen, Martin Dornheim, and Ruediger Bormann. Hydrogen sorption properties of MgH_2-$LiBH_4$ composites. *Acta Materialia*, 55(11), 2007.

[29] Frederick E. Pinkerton, Martin S. Meyer, Gregory P. Meisner, Michael P. Balogh, and John J. Vajo. Phase boundaries and reversibility of $LiBH_4$/MgH_2 hydrogen storage material. *Journal of Physical Chemistry C*, 111(35), 2007.

[30] J. Urgnani, F. J. Torres, M. Palumbo, and M. Baricco. Hydrogen release from solid state $NaBH_4$. *International Journal of Hydrogen Energy*, 33(12), 2008.

[31] Chiara Milanese, Sebastiano Garroni, Alessandro Girella, Gabriele Mulas, Vittorio Berbenni, Giovanna Bruni, Santiago Surinach, Maria Dolors Baro, and Amedeo Marini. Thermodynamic and kinetic investigations on pure and doped $NaBH_4$-MgH_2 system. *Journal of Physical Chemistry C*, 115(7), 2011.

[32] S. Garroni, C. Pistidda, M. Brunelli, G. B. M. Vaughan, S. Surinach, and M. D. Baro. Hydrogen desorption mechanism of $2NaBH_4 + MgH_2$ composite prepared by high-energy ball milling. *Scripta Materialia*, 60(12), 2009.

[33] Christopher C. Nwakwuo, Nico Eigen, Martin Dornheim, and Rudiger Bormann. Effect of group IV elements on the thermodynamic property of NaH+Al. *Renewable Energy*, 43, 2012.

[34] J. F. Mao, X. B. Yu, Z. P. Guo, H. K. Liu, Z. Wu, and J. Ni. Enhanced hydrogen

storage performances of $NaBH_4$-MgH_2 system. *Journal of Alloys and Compounds*, 479(1-2), 2009.

[35] S. Garroni, C. Milanese, A. Girella, A. Marini, G. Mulas, E. Menendez, C. Pistidda, M. Dornheim, S. Surinach, and M. D. Baro. Sorption properties of $NaBH_4/MH_2$ (M = Mg, Ti) powder systems. *International Journal of Hydrogen Energy*, 35(11), 2010.

[36] D. M. Liu, Y. F. Zhu, and L. Q. Li. Synthesis mechanism and properties of Mg-Mg_2Ni composite hydrogen storage alloy produced by hydriding combustion synthesis. *Materials Science and Technology*, 24(11), 2008.

[37] Yang Liu, Qian Li, Genwen Lin, Kuochib Chou, and Kuangdi Xu. Properties of Mg_2NiH_4 prepared by microwave-assisted activation synthesis from micro-particles. *Journal of Alloys and Compounds*, 468(1-2), 2009.

[38] Jiri Cermak and Lubomir Kral. Hydrogenation of Mg and two chosen Mg-Ni alloys. *International Journal of Hydrogen Energy*, 33(24), 2008.

[39] J. J. Reilly and R. H. Wiswall. Reaction hydrogen with alloys magnesium and nickel and formation of Mg_2NiH_4. *Inorganic Chemistry*, 7(11), 1968.

[40] P. Selvam, B. Viswanathan, C. S. Swamy, and V. Srinivasan. Studies on the thermal-characteristics of hydrides of mg, Mg_2Ni, Mg_2Cu and $Mg_2Ni_{1-x}M_x$ (M = Fe, Co, Cu or Zn - $0 < x < 1$) alloys. *International Journal of Hydrogen Energy*, 13(2), 1988.

[41] T. Sato, H. Blomqvist, and D. Noreus. Attempts to improve Mg_2Ni hydrogen storage by aluminium addition. *Journal of Alloys and Compounds*, 356, 2003.

[42] R. A. Varin, T. Czujko, Ch Chiu, R. Pulz, and Z. S. Wronski. Synthesis of nanocomposite hydrides for solid-state hydrogen storage by controlled mechanical milling techniques. *Journal of Alloys and Compounds*, 483(1-2), 2009.

[43] M. D. Banus, J. J. McSharry, and E. A. Sullivan. The sodium-sodium hydride-hydrogen system at 500-600-degrees. *Journal of the American Chemical Society*, 77(7), 1955.

[44] R. A. Varin and C. Chiu. Structural stability of sodium borohydride ($NaBH_4$) during controlled mechanical milling. *Journal of Alloys and Compounds*, 397(1-2), 2005.

[45] Karl J Gross, K. Russel Carrington, Steven Barcelo, Abhi Karkamkar, Justin Purewal, and Philip Parilla. Recommended Best Practices for the Characterization of Storage Properties of Hydrogen Storage Materials. Technical report, V2-64 U.S. D.O.E. Hydrogen Program, 2009.

[46] A. Parente, A. Nale, M. Catti, E. Kopnin, and P. Caracino. Hydrogenation properties of Mg_2AlNi_2 and mechanical alloying in the Mg-Al-Ni system. *Journal of Alloys and Compounds*, 477(1-2), 2009.

[47] C. Suryanarayana. Mechanical alloying and milling. *Progress in Materials Science*, 46(1-2), 2001.

[48] F. D. Maslan and T. M. Littman. Compressibility chart for hydrogen and inert gases. *Industrial and Engineering Chemistry*, 45(7), 1953.

[49] B.D. Cullity and S.R. Stock. *Elements of x-ray diffraction*. Pearson education. Prentice Hall, 2001.

[50] O. Palchik, A. Gedanken, and Y. Rubinstein. Simple air-tight powder x-ray diffraction cell. *Review of Scientific Instruments*, 74(6), 2003.

Appendix A

Experimental Techniques

A.1 Ball Milling for Materials Preparation

Ball milling has traditionally been used for mixing, changing the particle shapes, and size reduction. Since the 1960s ball milling has been used as a method for alloying metals and creating nano-materials. A very common type of high energy ball mill is a shaker or vibrational mill popularized by its manufacturer SPEX®. This milling method combines a back and forth motion with a lateral movement of the ends of the vial so that it moves in a figure eight [47]. A schematic of the jar's motion and that of the ball in a shaker / vibrational mill is shown in Figure A.1.

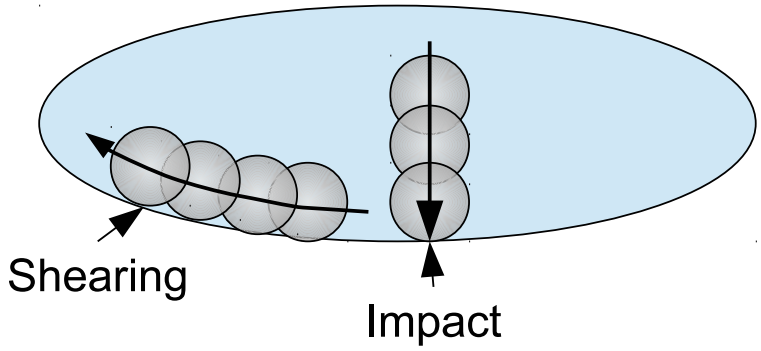

Figure A.1: Schematic of high energy ball milling process

The SPEX 8000® is classified as a high energy ball mill due to the amount of energy transferred from the balls to the powder being milled inside. The kinetic energy of the balls

in the system is given by equation A.1.

$$E = 1/2mv^2 \tag{A.1}$$

where m is the mass of the balls and v is their velocity. With ball speeds on the order of 5 m s^{-1} and a ball mass typically 8 g, a high energy ball mill will have about 20 mJ of energy per ball [47]. Most of this energy is dissipated as heat, with less than 1 % of the energy transmitted through impact [47]; however, some amount of shear is realized as the balls move along the walls of the jar.

The jars used for milling come in a variety of materials. Stainless steel is among the most common material.

The size of the balls used for milling as well as the ball to powder mass ratio are important. Typically a mass ratio of 10:1 ball:powder is used for the preparation of metal hydrides, but ratios from 5:1 up to 50:1 have been reported in the literature. A typical SPEX milling is performed for 1 to 5 hours, but times have been reported to be in the hundreds of hours [2].

Mechanical alloying is achieved through the milling of more than one type of elemental metal powder. The method is a non-equilibrium, low temperature solid-state processing method. Mechanical alloying is basically a repeated stressing, deformation, fracture, and cold welding of powder particles, which can be seen schematically in Figure A.2.

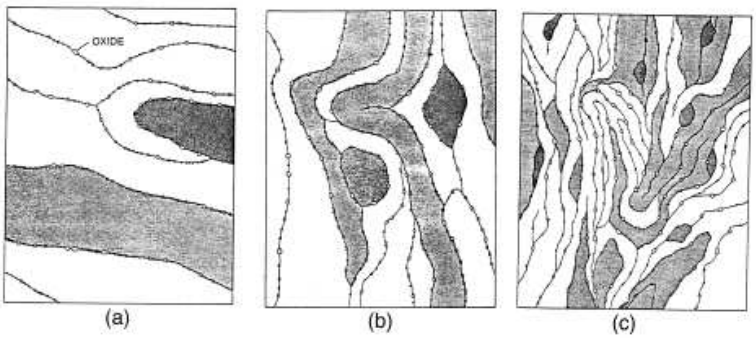

Figure A.2: Mechanical alloying steps [47] [©Progress in Materials Science, 2001, by permission]

Particle size reduction and grain size reduction occur in ball milling, which improves the ability of hydrogen to diffuse into or out of the metal powder particles. Figure A.3 shows the effect of milling time on particle size and grain size. In general a decrease in particle and grain size occurs, however a plateau occurs where the particle and grain size no longer become any smaller, this is because an equilibrium is reached between the fracturing of particle into smaller sizes and the welding of particles into larger sizes [47].

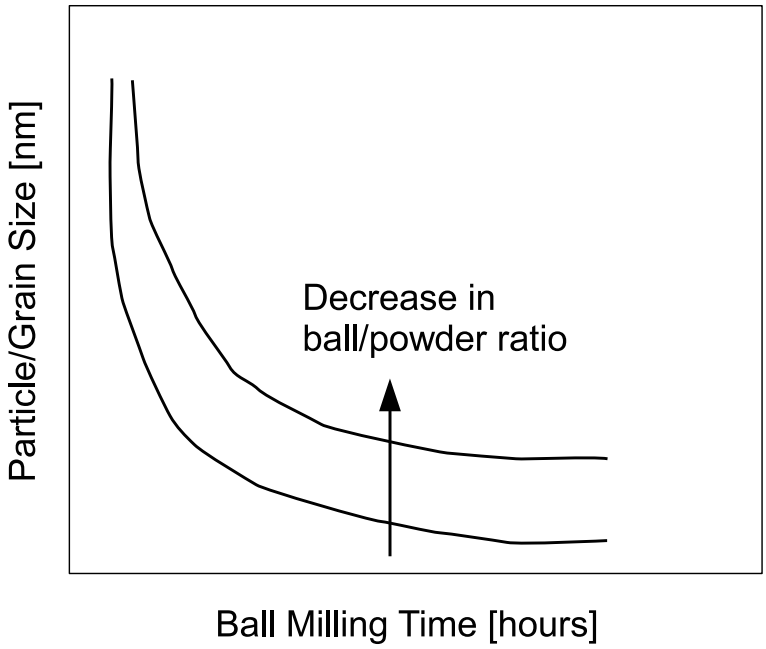

Figure A.3: Particle and grain size reduction as a function of milling time and ball to powder ratio ([47]) [©Progress in Materials Science, 2001, by permission]

For metal hydrides, the oxide shell that surrounds a lot of metals is broken up by the milling process enabling fresh surfaces to be exposed to the hydrogen. With a decrease in particle size there is an increase in specific surface area of the powder. The extra surface area that is not oxidized leads to significant improvements in the kinetics of the hydrogen desorption.

A.2 Pressure-Composition-Temperature (PCT)

A PCT (or Sievert's apparatus) is a manometric method for studies of gas absorption / desorption into solids and liquids. It consists of a temperature controlled autoclave which houses the sample reactor, gas manifold and valves, a vacuum pump, pressure transducers, gas (H_2, He) supplies, and reservoir volumes. Figure A.4 shows the schematic of a PCT

system.

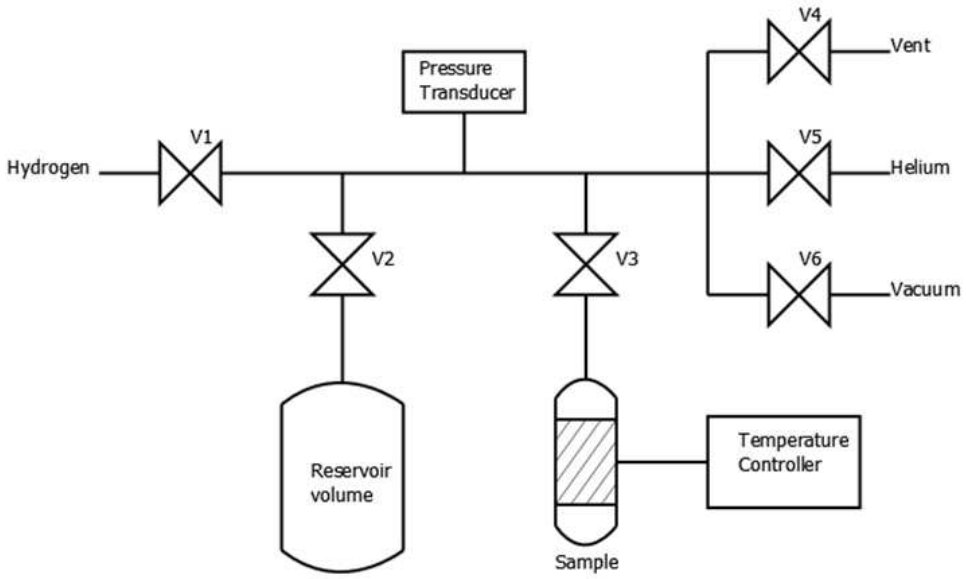

Figure A.4: Simplified schematic of a Sievert apparatus

The sample, which is usually in powder form, is placed into the temperature controlled reactor. The hydrogen pressure in the reservoirs is controlled by an electronic pressure regulator.

The basis of PCT measurements is the ideal gas law:

$$PV = nRT \tag{A.2}$$

where P = pressure, V = volume, n = moles of gas, R = gas constant (0.082 L atm K^{-1} mol^{-1}) and T = temperature. The ideal gas law assumption is valid here because the compressibility factor for hydrogen for the pressures used here (<200 bar) is negligible [2]. Masla et. al. [48] show that the compressibility of hydrogen between 1 and 150 bar and temperatures between 20 and 400 ºC is between 1 and 1.10.

During a hydrogen absorption process gas pressure drops. This change in pressure (ΔP)

can be used to determine the quantity of hydrogen that is absorbed. The converse is true for desorption, where a rise in pressure signifies the release of hydrogen. Equation A.3 shows the relationship between a change in pressure and the change in the number of moles associated with it.

$$\Delta n_{abs/des} = \Delta P_{dec/inc} \frac{V}{RT} \tag{A.3}$$

The weight percent (wt%) of hydrogen released can then be calculated from equation A.4.

$$wt\% = \frac{2M_{H_2} \triangle n_{abs/des}}{m_{sample}} \tag{A.4}$$

where M_{H_2}= molar mass of hydrogen (1.008 g/mol), $\triangle n_{abs/des}$ is the moles of hydrogen absorbed or desorbed and m_{sample} is the mass of the sample in the reactor.

A common and quick experiment is to heat the sample temperature from room temperature to a desired level, at a constant heating rate. This is referred to as a temperature programmed desorption or TPD. The rise in the hydrogen pressure provides a measure of the amount of hydrogen stored in the materials. Different metal hydride systems can also be compared by the temperature at which hydrogen starts to release.

A.2.1 Van't Hoff Analysis

The enthalpy of desorption / absorption is related to the equilibrium pressure at which the hydrogen is desorbed / absorbed and the relationship can be described by the van't Hoff equation (equation 2.6). The equilibrium pressure for a fixed temperature can be obtained from a pressure-composition-temperature (PCT) plot, sometimes called isothermal pressure-concentration curve (seen in Figure A.5a).

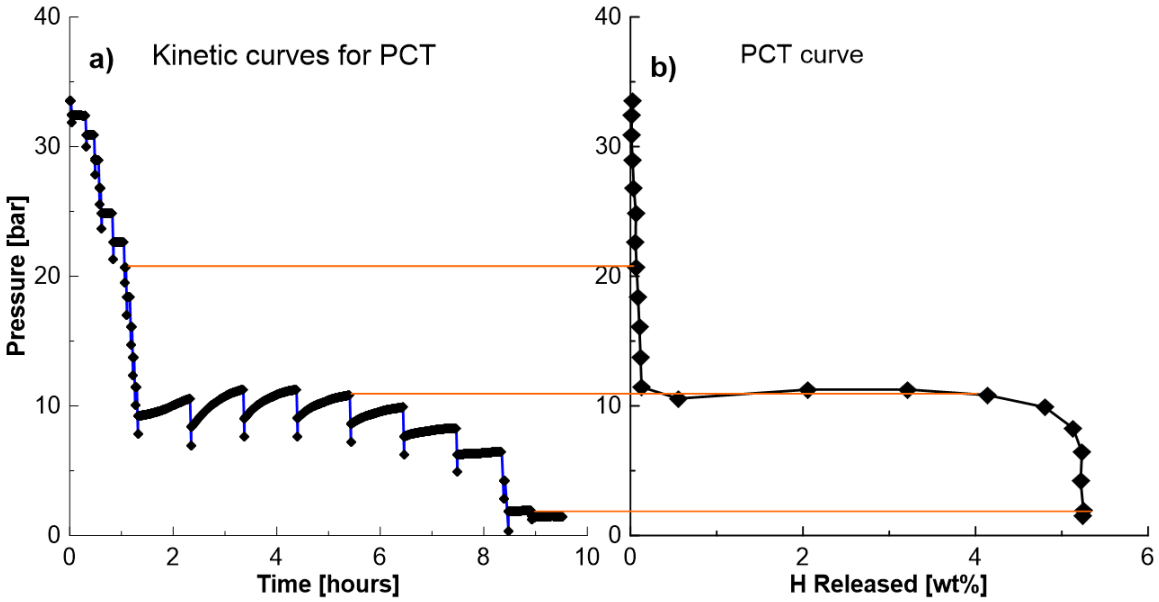

Figure A.5: PCT measurement for desorption

Figure A.5a shows how single step kinetic hydrogen desorption reactions are used to produce an absorption PCT isotherm. For these measurements the sample is first heated to the desired temperature and pressurized. A small dose of hydrogen is then subtracted from the sample (this can be observed in Figure A.5a by the several sharp peaks) and allowed to desorb until it reaches equilibrium; this is the point where the hydrogen gas and the hydrogen in the solid are in equilibrium. This process of subtracting a known amount of hydrogen to the sample and reaching equilibrium is repeated several times until the metal hydride no longer has any hydrogen. At this point the pressure in the sample starts to fall with each subtraction of hydrogen(Figure A.5a).

Figure A.5b shows the PCT curve derived from the kinetic hydrogen absorption graph shown in Figure A.5a. The equilibrium pressure for each dose of hydrogen is plotted versus the amount of hydrogen added for that dose. The result is a PCT curve showing the equilibrium absorption pressure of the metal hydride for the temperature examined.

A series of isothermal pressure-concentration (or PCT) curves at different temperatures allows the computation of the desorption / absorption enthalpy by using the van't Hoff relationship. Figures 2.6a and 2.6b in Chapter 1 show this.

A.2.2 Sample Volume Calibration

In the PCTPro 2000 apparatus, there is a temperature gradient from the sample holder to the reservoir. This implies that the gas temperature is not uniform. The temperature gradient makes it difficult to calculate the change in moles of gas due to absorption and desorption using the ideal gas law [45]. Fortunately, a correction to the sample's dead volume would be sufficient to correct for this non-uniformity. The dead volume is the extra space surrounding the sample in the heated reactor up to the valve. It is usually minimized through the use of spacer bars placed in the reactor, but is not completely eliminated. The dead volume is schematically shown in Figure A.6, where the space around the sample and spacer is occupied by a small amount of gas only.

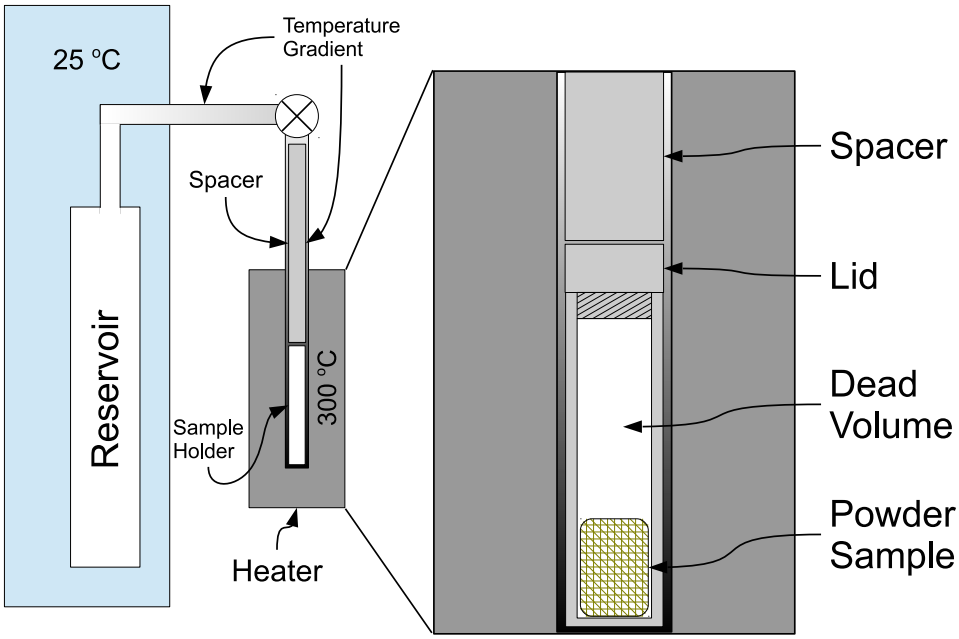

Figure A.6: Schematic of temperature gradient in hydrogen above the loaded sample. The temperature gradient starts at 300 ºC in the heater and ends at 25 ºC in the reservoir. The sample dead volume and spacer can be seen directly above the sample.

Higher temperature leads to gas expansion and makes the dead volume appear smaller. A simple calibration procedure is then used to determine the apparent volume at the temperature of interest.

The calibration procedure involves determining an apparent sample dead volume to compensate for the temperature gradient. Figure A.7 shows a simplified Sieverts apparatus schematic.

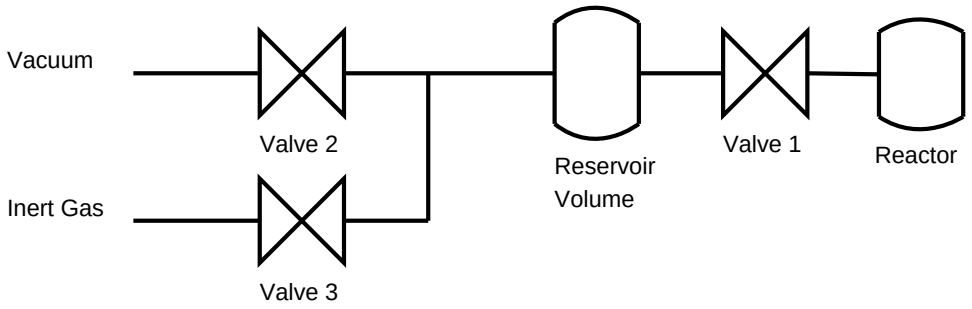

Figure A.7: Simplified Sieverts schematic for volume calibration

Volume Calibration Steps

There are two steps for calibrating the reactor volume (using Figure A.7).

1. Evacuate the reactor volume and system volume and close the valve between them (Valve 1).

2. Introduce inert gas (argon or helium) into the reservoir volume to a prescribed pressure P_1.

3. Close all valves to system volume (Valves 2 and 3).

Open valve to the reactor and record the change in pressure.

1. Close the valve to the reactor with the inert gas still in it at pressure P_2 and evacuate the system volume.

2. The reactor valve (Valve 1) is then opened and the pressure (P_3) is noted.

Here system volume (V_S) refers to the volume of the piping connecting the various components in the Sieverts apparatus between the valves as well as the reservoir volume (V) shown in Figure A.7. Care should be taken to ensure that all the components are at thermal

equilibrium when the pressure readings are made. Equation A.5 shows the relationship between pressure change, the volume being calibrated (V_R) and the system volume (V_S which is known).

$$P_1 V_R = P_2 (V_R + V_S) \tag{A.5}$$

Rearranging equation A.5 for V_R leads to equation A.6.

$$V_R = \frac{(P_2 V_S)}{(P_1 - P_2)} \tag{A.6}$$

Because of the difference in temperature between the reactor and the rest of the system, calibration must be repeated for each temperature that an absorption or desorption is done. This calibration procedure can only be performed for absorption as hydrogen will evolve from the sample if the pressures used are below the equilibrium pressure of the hydride.

A typical Sieverts system may have several calibrated volumes of different sizes in order to be able to handle various amounts of hydrogen being desorbed or absorbed. This relates to the equilibrium pressure of the hydride sample, as for a given temperature the hydride will absorb or desorb hydrogen until it reaches the equilibrium temperature, at which point it will no longer absorb or desorb hydrogen. This pressure increases with increases in temperature.

A.2.3 Volume Selection

Care should be taken when selecting the volume of the system during an experiment because the rate of absorption or desorption will vary with the proximity to the equilibrium pressure. For desorption, if the volume chosen is too small, it will only release hydrogen until it reaches its equilibrium pressure. At this point the rate of hydrogen release will decrease as the driving force is reduced. Eventually hydrogen release will stop at the equilibrium

pressure where an equal amount of hydrogen is being desorbed as is being absorbed. If the volume chosen is too large then the change in pressure from desorption will be too small for the pressure sensor to resolve accurately and the resolution of the data will suffer.

A similar effect can be seen for absorption. If the volume chosen is too small for the experiment the pressure drops to the equilibrium pressure and absorption will stop, even if the hydride holds more hydrogen. If the volume is too high the pressure drop measured will be small and will suffer from poor data resolution in a similar manner to desorption.

Proper volume selection is required such that the largest constant driving force is obtained by choosing as large a volume as possible, but the resolution in data is maximized by choosing as small a volume as possible. These are conflicting requirements and both need to be satisfied as much as possible. The concept of driving force can be clearly seen in Figure A.8 for desorption where the farther away from the equilibrium pressure (solid black curve) the larger the driving force for hydrogen release there is.

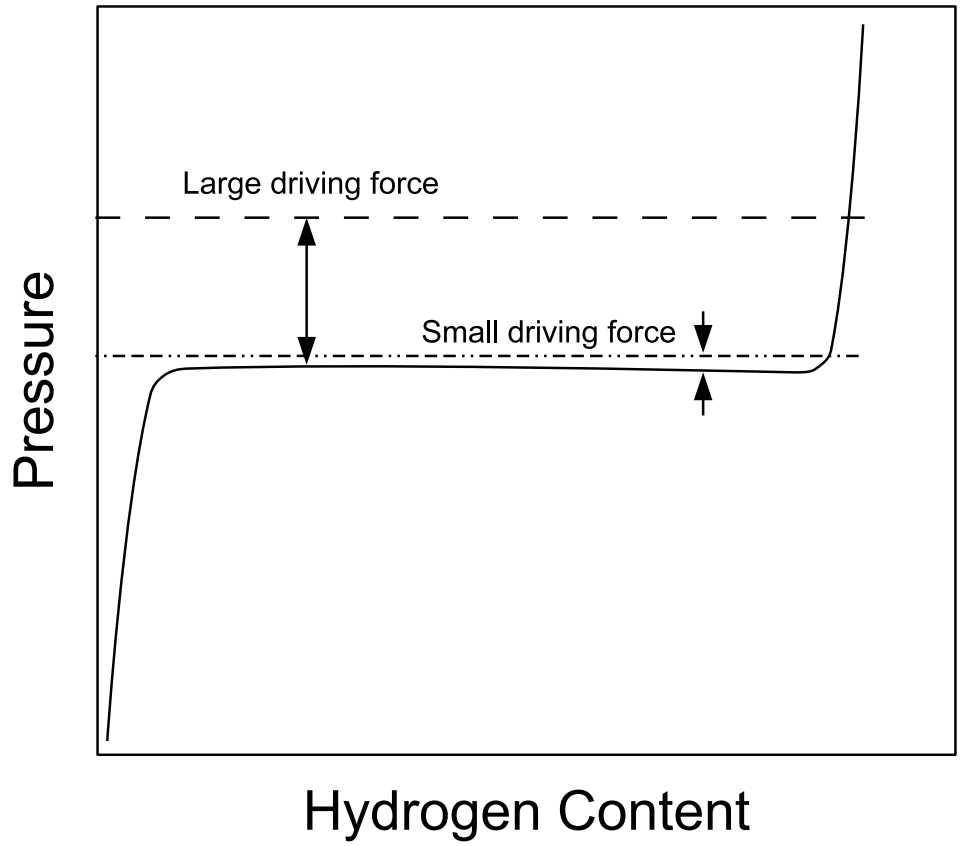

Figure A.8: Illustration of driving force for absorption where the equilibrium pressure is the solid black curve and two absorption pressures are applied: a very small driving force and a large driving force.

A.2.4 Desorption Pressure

The initial pressure at which desorption was performed varied from 1 bar to about 5 bar. Figure A.9 shows an apparatus with a sample reactor (V_R) and reservoir volume (V_S) to illustrate the procedure.

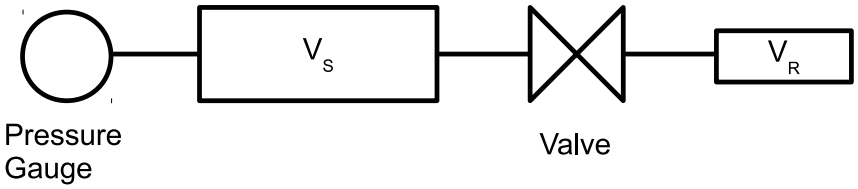

Figure A.9: A simplified schematic diagram of PCT equipment

Usually the sample reactor (V_R) is pressurized to stop the hydrogen from desorbing at temperatures above the equilibrium temperature for isothermal measurements. The calculation to determine the pressure required in the sample reactor (P_R) before opening the valve is shown in equation A.7.

$$P_R = \frac{P_T (V_S + V_R)}{V_S} \tag{A.7}$$

where P_S is the sample reactor pressure and P_T is the pressure in the total system after opening the valve. This calculation is done after the system volume calibration has been completed. Equation A.7 is valid only if the reservoir volume (V_S) is evacuated before opening the valve.

A.2.5 Error due to Temperature Fluctuations During the Manometric Measurements

The temperature of the reservoir in the PCT Pro 2000 is controlled through a heater and is set to a constant temperature about 5 ºC above ambient temperature 22 - 27 ºC. The temperature fluctuations are within ± 0.5 ºC. Figure A.10 shows the reservoir temperature variations over 2.5 days. The temperature varies from 25.8 to 27 ºC over this period. The temperature fluctuations directly impact the pressure measurements. Using the ideal gas law, a ± 0.5 ºC fluctuation corresponds to about ± 0.03 wt % error in the hydrogen capacities determined.

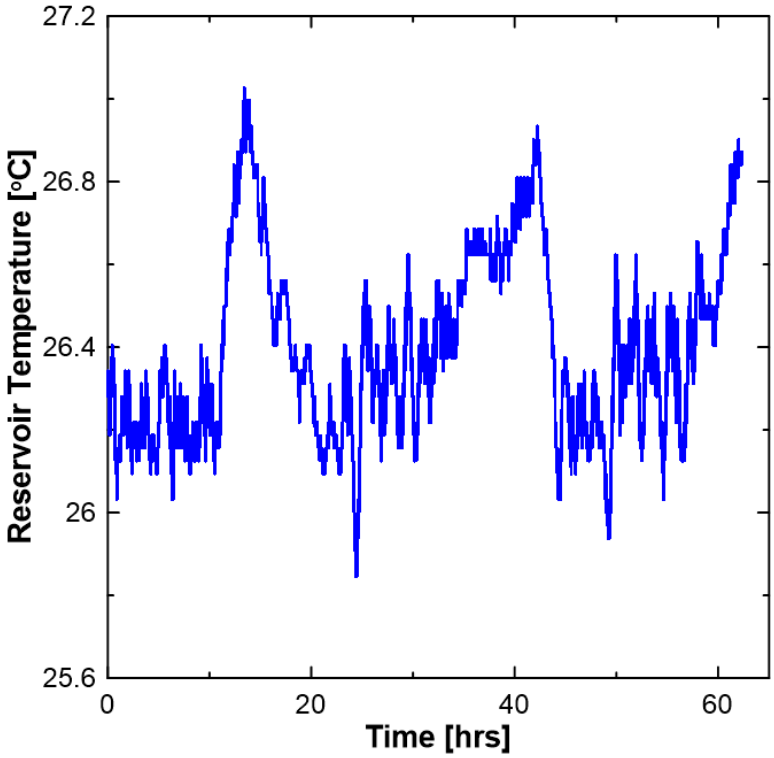

Figure A.10: PCT Pro 2000 reservoir temperature over about 2.5 days

During a TPD measurement, when the sample is heated, pressure increases because of both the gas expansion and by any hydrogen which is desorbed during the heating. For the different reservoir sizes a temperature ramp of 6 ºC min^{-1} under 1 bar of hydrogen back pressure was completed to measure the gas expansion part of the pressure increase. Figure A.11 shows this apparent hydrogen desorption effect. During the temperature ramp from 25 to 450 ºC, the apparent desorption is about 0.08 wt %, assuming a sample size of 0.2 g, which is typically used in the experiments reported in this thesis. When the temperature is maintained a 450 ºC for 5 hours, gas continues to expand, and the apparent desorption reaches 0.16 wt %.

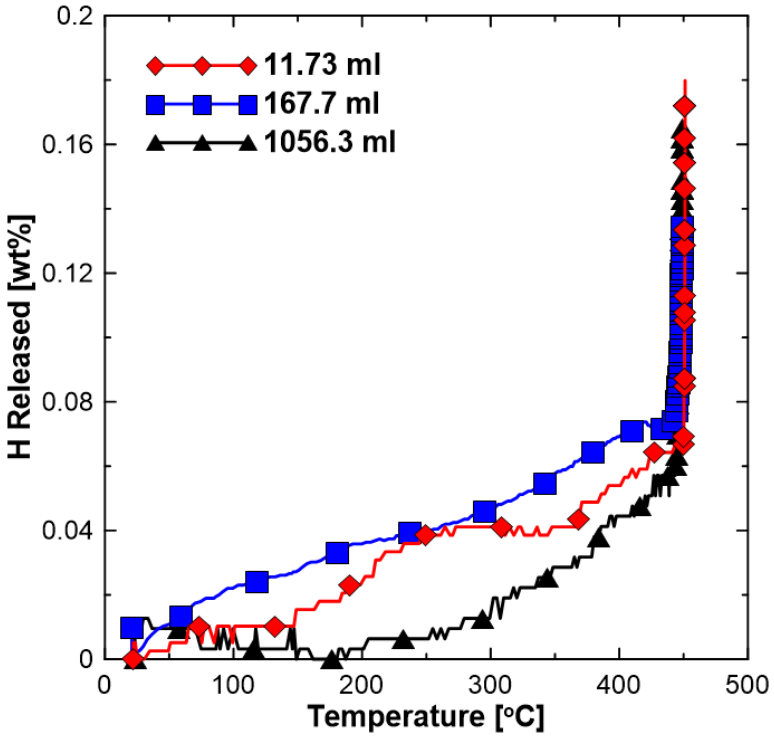

Figure A.11: Gas expansion during a TPD measurement of an empty sample holder. The rise in pressure can be interpreted as hydrogen release. Data are shown for 3 different reservoir volumes.

A.3 X-Ray Diffraction (XRD)

Through XRD powder analysis, bulk phase properties such as crystallographic phases, grain size and lattice spacings can be determined. Crystallographic phases can be obtained by using a database of known powder diffraction files. Grain size is calculated from the Scherrer equation and lattice spacings are determined from Bragg's law [49]. For this thesis a Bruker D8 Advance with a 0.6 mm slit, a Vantec-1 X-ray detector and a Cu Kα source for X-rays were used. The analysis software was EVA version 14 with powder diffraction file (PDF) database version 9.

A.3.1 Crystallographic Phases

The crystallographic phase can be determined through XRD powder analysis. X-rays directed at a sample will reflect back at the same angle that they were hit. Because X-rays are electromagnetic radiation waves, their intensity can be attenuated and accentuated by the addition of other X-rays waves with different phase angles. This is called constructive and destructive interference respectively.

Constructive interference is governed by Bragg's law of diffraction (equation A.8), where λ is the wavelength of the X-rays, d is the interplanar distance between atoms in a crystal and θ is the angle of incidence.

$$\lambda = 2\text{dsin}\theta \tag{A.8}$$

Powder diffraction X-ray analysis takes advantage of the multiple orientations of crystallites (grains) to provide information about the crystallographic data of the materials. Figure A.12 shows several separate particles with several crystallites in each of the particles. Each crystallite has a single crystal orientation, with each particle having several crystallites and several orientations. The crystallites are separated by a grain boundary.

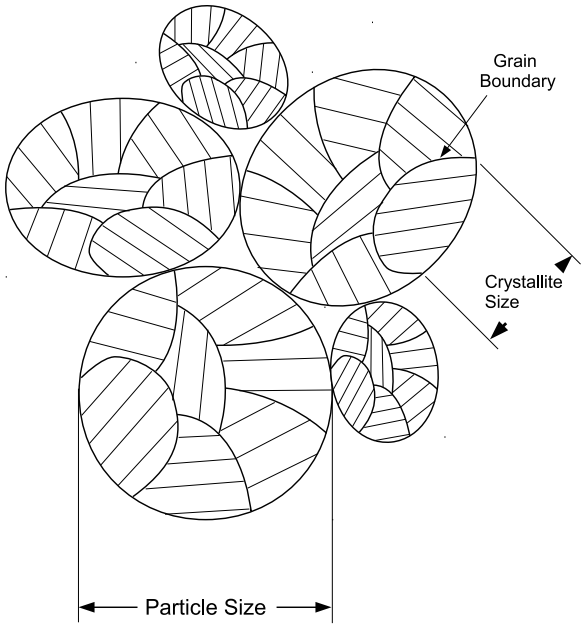

Figure A.12: Multiple crystallites (grains) and particles.

The XRD pattern is unique for every material with a crystal structure so that the identification of an unknown sample, through the use of a database of known patterns, can be obtained.

A.3.2 Grain and Particle Size

The grain size refers to the size of the individual crystallites that compose a larger particle. The size of these grains can be determined by the Scherrer equation shown in equation A.9.

$$d_g = \frac{0.9\lambda}{\beta_{FWHM}\cos\theta} \tag{A.9}$$

where d_g is the grain size, λ is the wavelength of radiation used, β_{FWHM} is the full width at half the maximum peak height (FWHM) used to determine the grain size, and 2θ is the diffraction angle of the peak. The multiplier can vary from 0.9 to 1 and depends on the shape of the crystallites [49]. Typically only grain sizes less than 100 nanometers can be

determined accurately.

A.3.3 Effect of Hydrogen Back Pressure During Sample Cooling

The hydrogen pressure in the sample holder could affect the composition of the hydride composite during cool down. All the samples studied here in this thesis were evacuated before cooling, otherwise some hydrogen absorption would have occurred during the cooling. This is shown in Figure A.13. Two samples were cooled under different hydrogen back pressures. For the sample cooled down under 1 bar hydrogen back pressure $NaBH_4$ and Mg_2NiH_4 phases are observed. As the sample cools down the equilibrium pressure for absorption reached and the absorption of hydrogen can take place.

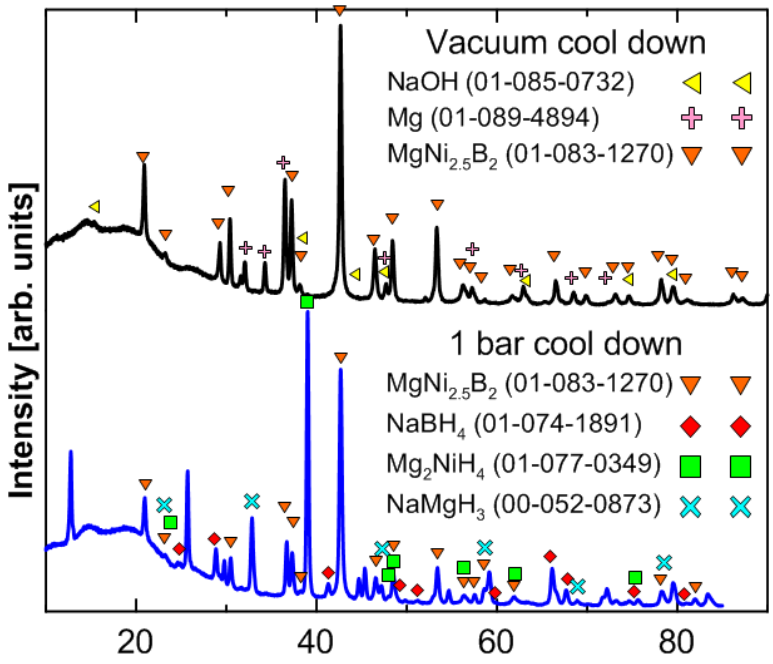

Figure A.13: Effect of hydrogen back pressure during cooling on hydride composition

A.4 Differential Scanning Calorimetry (DSC)

During a chemical reaction, heat is either released (exothermic) or absorbed (endothermic). Thus formation of new phases or compounds can be detected by measurement of the heat of reaction, i.e., exotherms / endotherms. The phase changes that a hydride undergoes as it releases and absorbs hydrogen can be measured through the use of a differential scanning calorimeter (DSC). Here the sample and an empty reference sample are heated at a constant rate and the difference in heat required to keep the sample at the same temperature as the reference sample is recorded as a function of temperature or time [24].

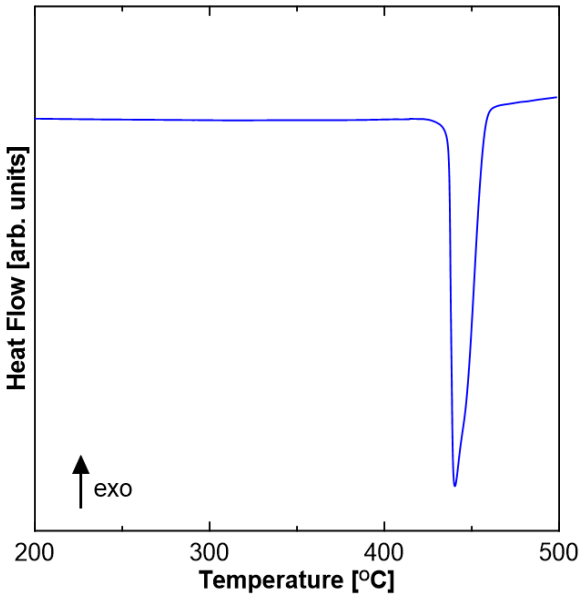

Figure A.14: DSC scan for the desorption of the MgH_2

Figure A.14 shows the calorimetric desorption profile for the MgH_2. The desorption scans are shown with downward peaks indicating that the phase changes are endothermic, while for absorption peaks are pointing up thus indicating exothermic reaction. Not all of the peaks represent hydrogen release and absorption. Changes in phase from solid to liquid or from one crystal structure to another are also seen as these changes require energy

transfer into or out of the system.

Appendix B

Estimation of Na Loss From the Sample Holder

A simple image processing method was used to estimate the Na loss during the hydrogen desorption reaction of $4NaBH_4$ / $5Mg_2NiH_4$. Figure B.1 shows the picture of the Na compounds deposited on the spacer. Using Irfanview software and the known diameter of the spacer, the diameter and height of the Na-based dome was estimated. This data was used in Solidworks to reconstruct the dome and calculate its volume. The mass of Na was then calculated from the density and the estimated value of volume.

Figure B.1: Photo of Na on spacer in reactor

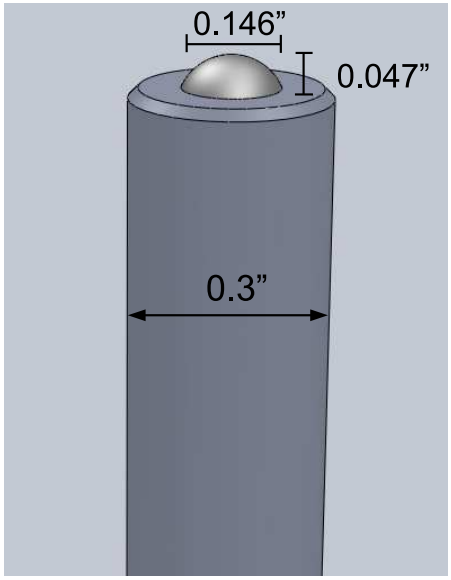

Figure B.2: Solidworks rendering of Na on sample holder spacer

Appendix C

Acoustic Box for Ball Mill

A Spex 8000™ ball mill generates considerable noise. In order to keep the noise level in the lab to a minimum an acoustic box was designed and built to house the ball mill. Because the acoustic box is sealed, a ventilation system was incorporated with fans pushing air into the box on one side and out of the box on the other side through a specially designed ducting for noise mitigation. A microcontroller was programmed and used to turn the fans on and off when the acoustic box reached a certain temperature (about 30 °C). Figure C.1 shows the rendered drawing of the enclosure made before construction began with the cover on the ventilation system made clear so that the ventilation design can be seen.

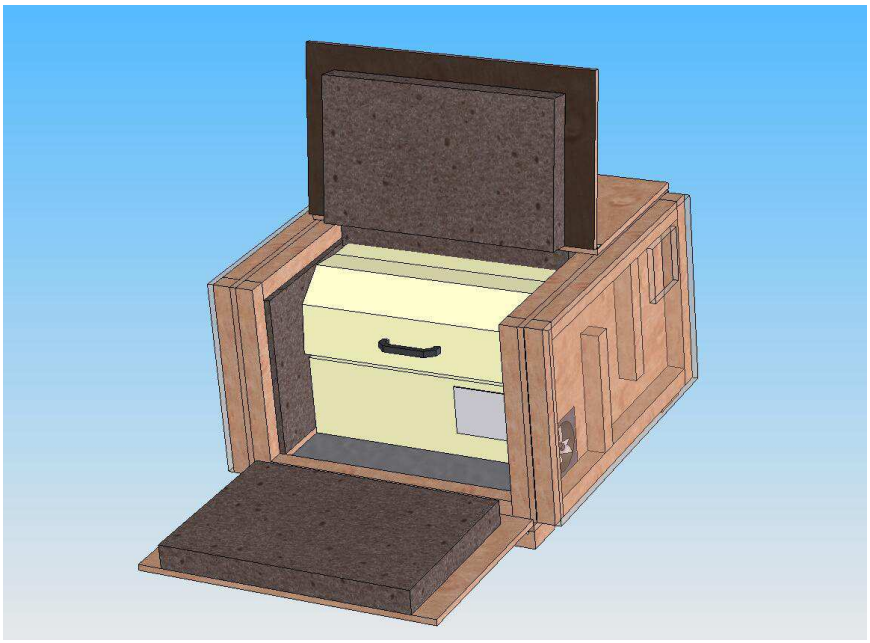

Figure C.1: Rendered drawing of acoustic box with ventilation system exposed

The actual constructed box can be seen in Figure C.2. The acoustic attenuation is so good that the ball milling cannot be heard when it is running.

Figure C.2: Acoustic box after completion

Figure C.3 shows the electronics installed on the side of the box to turn the ball mill on and off, as well, the microcontroller that controls the fans is here (under the top level printed circuit board (PCB)).

Figure C.3: Electronics control box on side of acoustic box

Appendix D

X-Ray Diffraction Sample Holder

Because the samples prepared and studied here were oxygen and moisture sensitive, a special sample holder was required to handle the powder during x-ray diffraction measurements. Commercial air-sensitive sample holders did not fit the XRD system (Bruker D8) used. Thus in-house holders were developed and used. We adopted a design proposed by Palchik et al.[50]. Their design was partially modified by making the assembly shorter thereby eliminating one of the o-rings. We also used Kapton film instead of Mylar film. Figure D.1 shows the XRD scan of an aluminum plate with and without a Kapton film. It can be seen that the Kapton is quite transparent to x-rays and little attenuation of the peaks occur. No additional background peaks are observed.

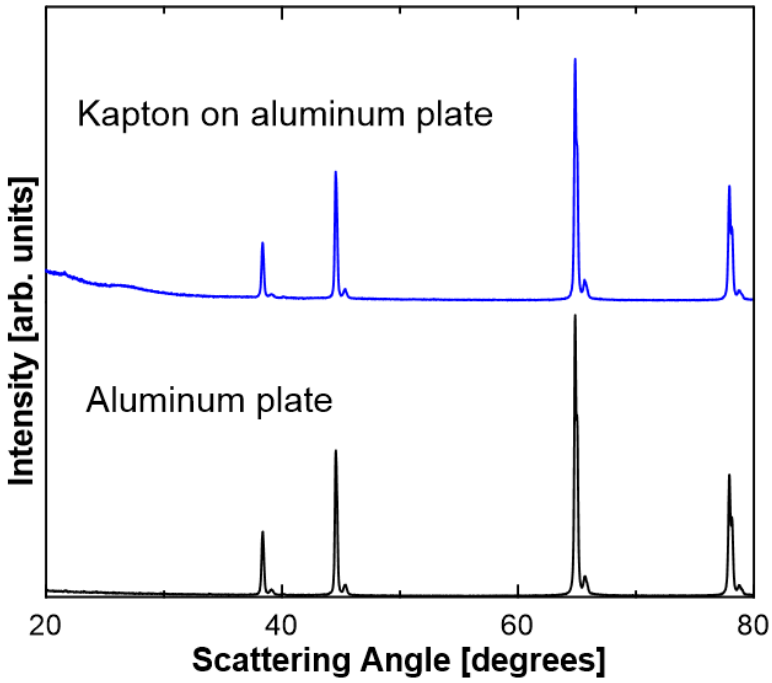

Figure D.1: XRD scan of aluminum with and with out Kapton (deg in 2θ).

Figure D.2 shows a photograph of the XRD samples holders made.There are three part: A - Base, B - Ring, C - Sample pan and D - Screw. The powder sample is placed into the Sample pan (C) and then placed onto the base. The lid is then secured over the base and the screw (D) tightened.

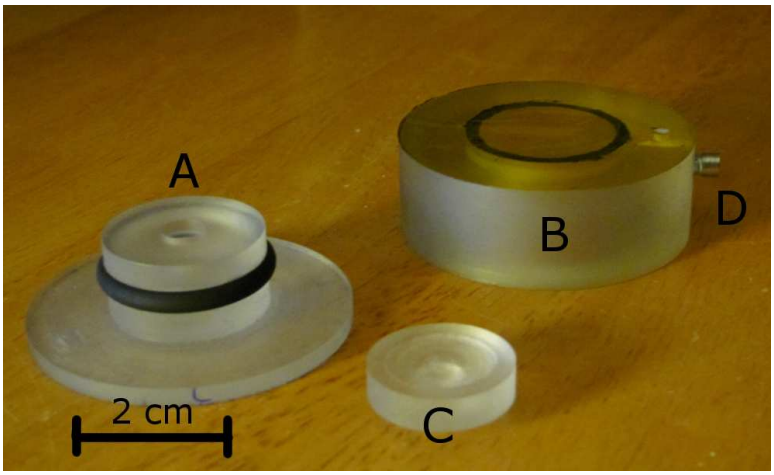

Figure D.2: Photograph of XRD airtight sample holder

A sample loading tray was also designed to work with the XRD sample holder and is shown in Figure D.3.

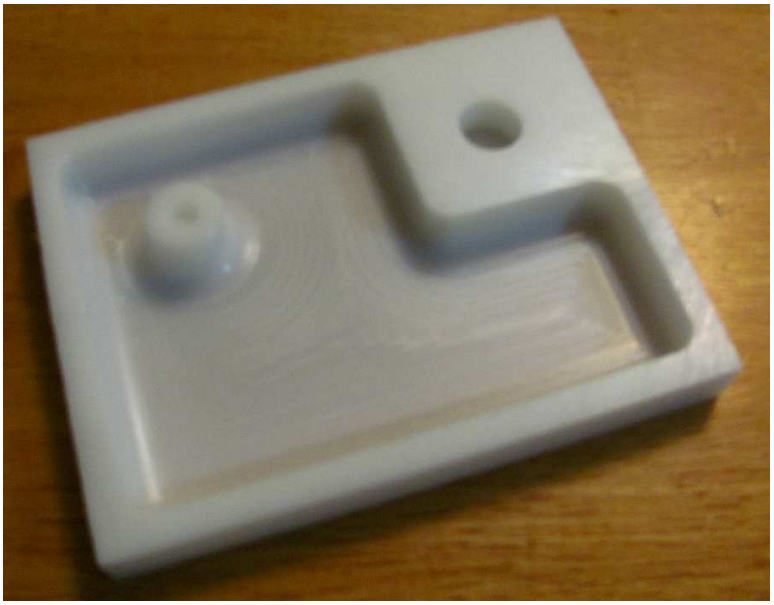

Figure D.3: Sample loading tray for airtight XRD sample holder

The following are the engineering drawings for the XRD sample holders as made for

this thesis.

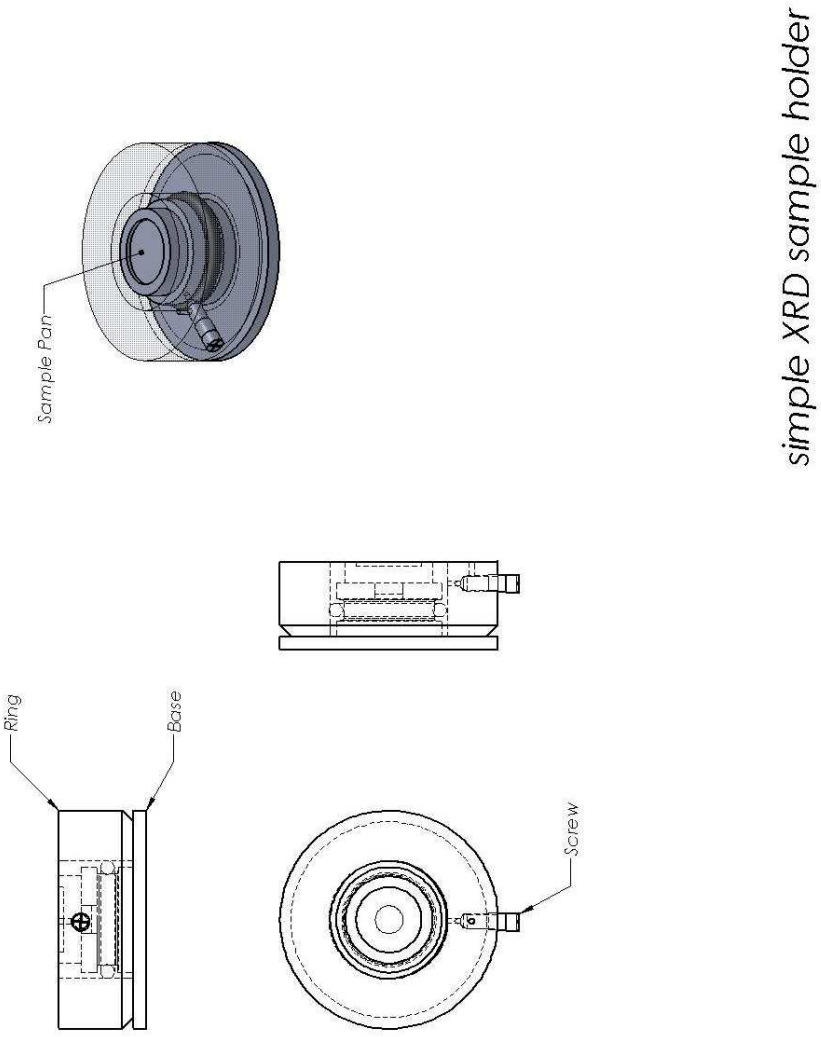

Figure D.4: Simple XRD sample holder

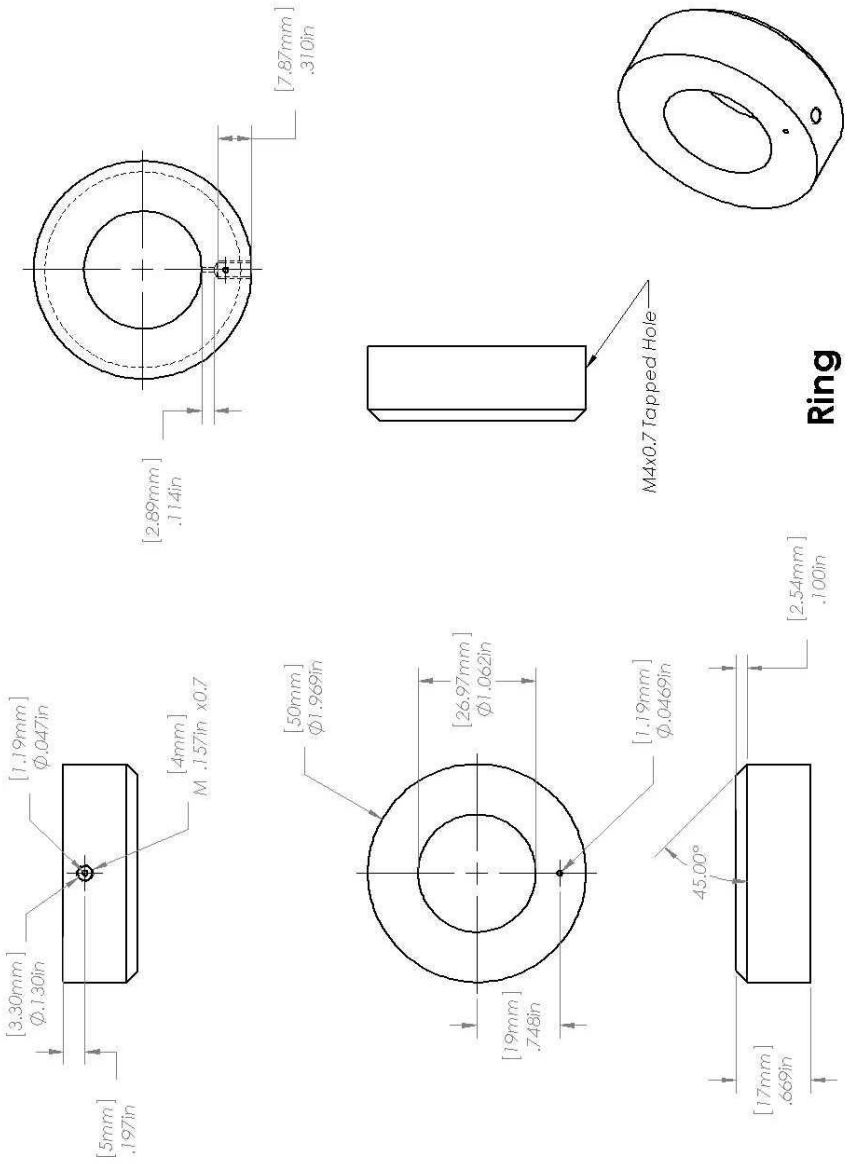

Figure D.5: Ring part for simple XRD sample holder

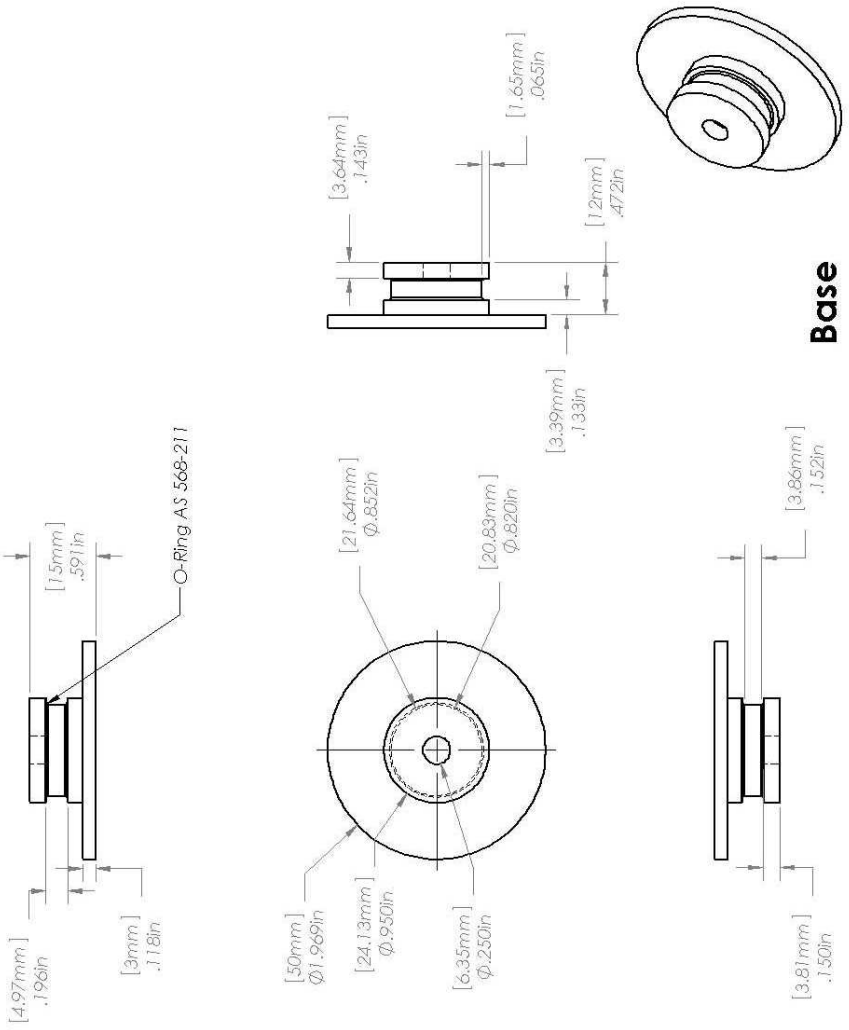

Figure D.6: Base part for simple XRD sample holder

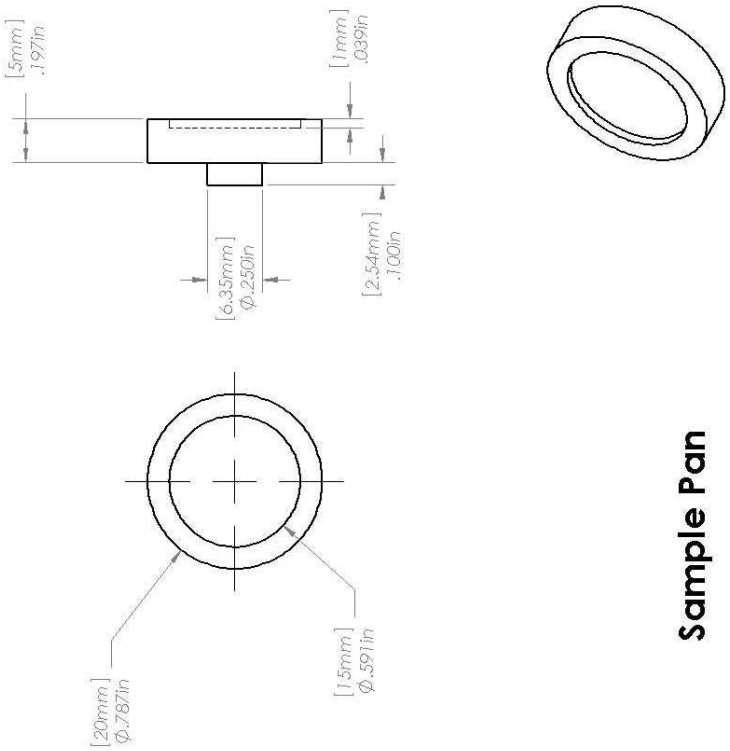

Figure D.7: Sample pan part for simple XRD sample holder

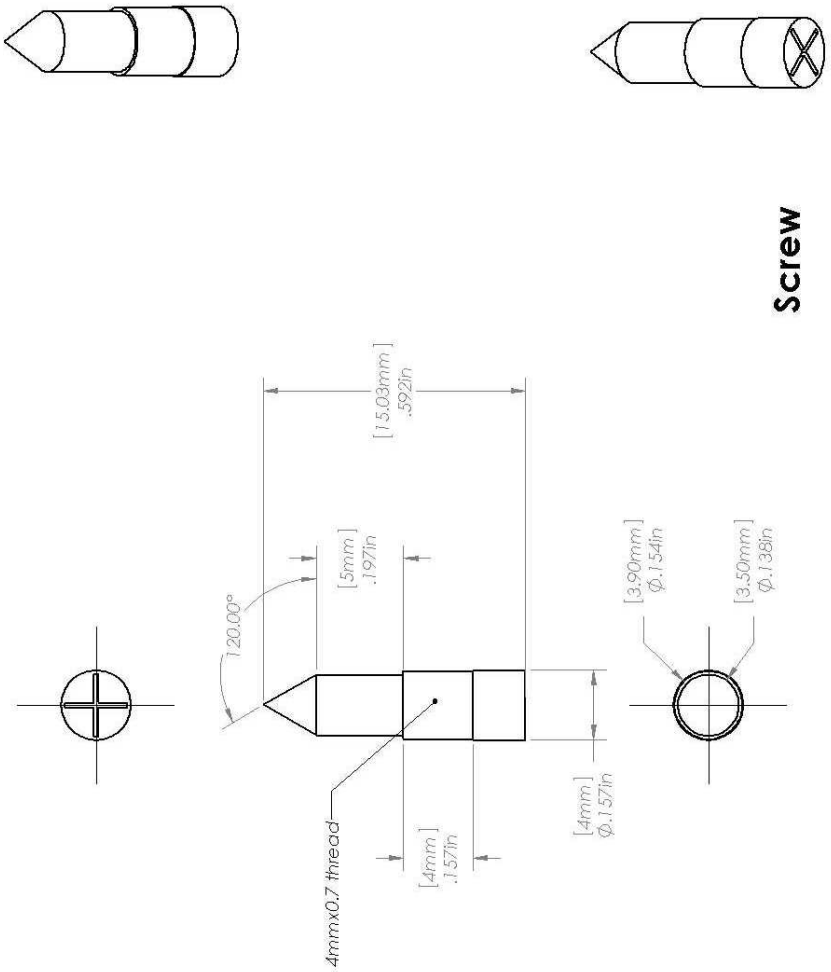

Figure D.8: Screw part for simple XRD sample holder

Appendix E

XRD Analysis Program

A program was written to analyze the data collected from the XRD machine. Grain size and peak matching were incorporated into the program. Figure E.1 shows the fitting page of the program. Choices such as which data to show and how much smoothing to apply to the raw file are given. At the bottom the choice to output the all the data to a file for later use is also given.

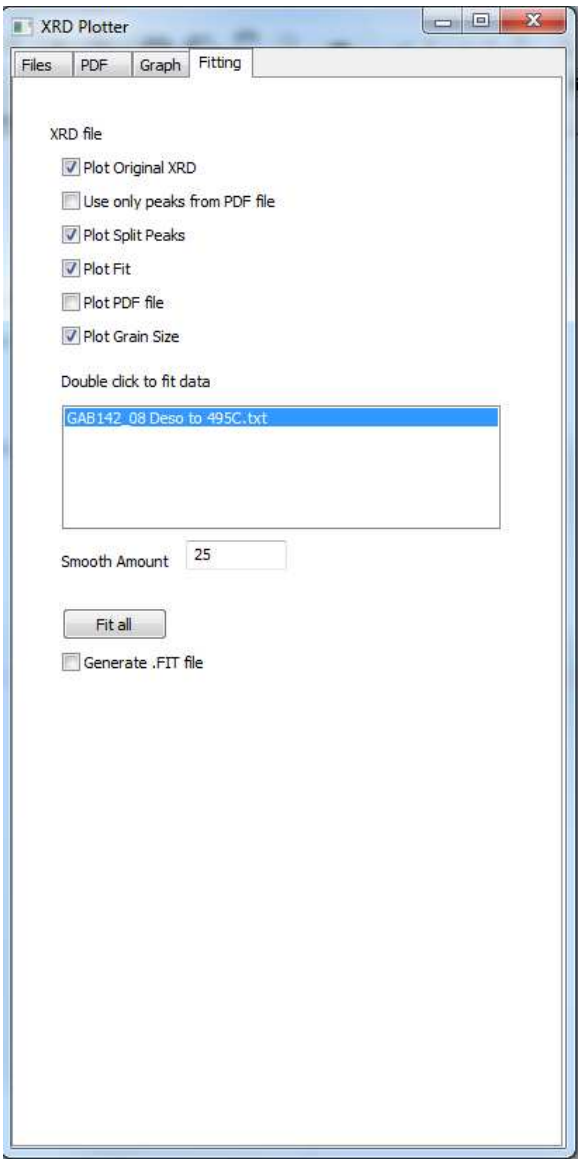

Figure E.1: Fit page for XRD program

The XRD fitting program can read an entire scan at once and split it into individual peaks that it then sequentially fits. The fit algorithm in the program uses a pseudo - Voight function which is a function of the form

$$\mathrm{I}(2\theta) = \mathrm{I}_{\mathrm{hkl}}[\eta \mathrm{L}(2\theta - 2\theta_0) + (1-\eta)\mathrm{G}(2\theta - 2\theta_0)] \tag{E.1}$$

where L and G are the Lorentz and Gaussian functions respectively, and η represents how much of each function is used. I_{hkl} is the intensity and is a scaling factor that multiplies through everything to match the peak height of the fitted data.

The peak search algorithm uses a Gaussian smoothing algorithm to smooth the data so that the first derivative can be used to find the start and end of each peak. It looks for a change in the sign of the derivative to determine the peak location and the beginning and end of the peak.

The grain size is calculated by using the Scherrer equation shown in Equation E.2.

$$\mathrm{d} = \frac{0.9\lambda}{\beta_{\mathrm{FWHM}} \cos\theta} \tag{E.2}$$

Where d is the grain size, l is the wavelength of radiation used, β_{FWHM} is the FWHM of the peak used to determine the grain size, and θ is the diffraction angle of the peak. The value 0.9 can vary up to 1 and depends on the shape of the crystallites.

By fitting the data and obtaining the FWHM which is the full width of the peak at half of the maximum height of the peak (full width half max) an estimate of the grain size can be obtained. However, other factors must be taken into account first, specifically instrumental resolution. Instrumental resolution can be mitigated by obtaining a reference scan from a mono-crystalline material such that the peaks will be as narrow as possible. This will define the instrumental resolution of the machine.

Program output is shown in Figure E.2. There is a lot of information on the graph. In solid blue is the original XRD scan as received from the XRD machine, and superimposed just beneath it is a multitude of coloured peaks which are the peaks that the search algorithm has identified. Each peak that is fit is shown as a different coloured series of small crosses

and the fit is shown as a solid line just behind it. To the right of the fitted peak is the calculated grain size. A PDF (powder diffraction file) can be used to do peak identification and can be seen here for $NaAlH_4$ by the long vertical blue lines with red diamonds on top of them.

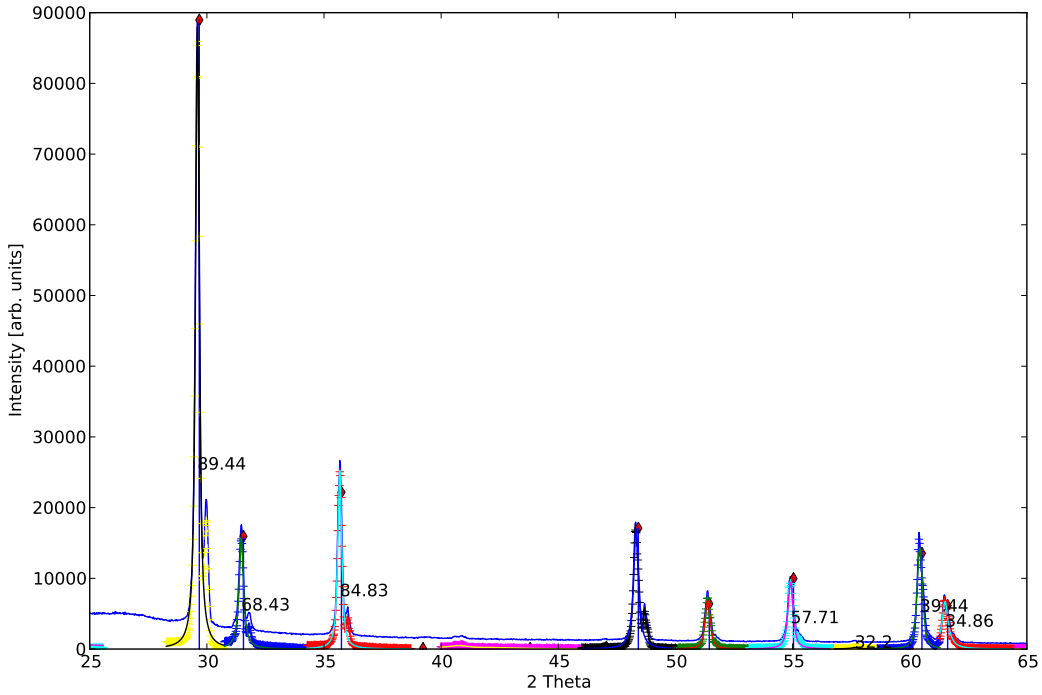

Figure E.2: Graphical output from XRD program showing the original XRD scan (solid blue) overlaid with the fitted peaks with baseline removal (multiple colours). The PDF file is also shown for peak matching along with the grain size is placed to the right side of each peak